UNIVERSITÉ DE SHERBROOKE
Faculté de génie
Département de génie mécanique

Analyse dynamique (CFD) et thermodynamique combinée dans un éjecteur supersonique en présence de gouttelettes

Combined CFD and thermodynamic analysis of a supersonic ejector with liquid droplets.

Thèse de doctorat
Specialité : génie mécanique

Sergio CROQUER

Jury: Prof. S. PONCET (directeur, Université de Sherbrooke)
Dr Z. AIDOUN (co-directeur, Ressources Naturelles Canada)
Prof. S. MOREAU (examinateur, Université de Sherbrooke)
Prof. P. PROULX (rapporteur, Université de Sherbrooke)
Prof. S. ELBEL (examinateur, University of Illinois at Urbana-Champaign)
Prof. Y. BARTOSIEWICZ (examinateur, Université Catholique de Louvain)

Sherbrooke (Québec) Canada Janvier 2018

Computers are useless.
They can only give you answers.
- Pablo Picasso

RÉSUMÉ

Ce projet de recherche a pour objectif principal d'étudier en détail les caractéristiques de l'écoulement interne dans des éjecteurs supersoniques monophasiques pour des applications en réfrigération, et les effets potentiels de l'injection de gouttelettes sur les performances de l'appareil. A cette fin, une approche numérique est proposée et a été séparée en deux parties.

Tout d'abord, une stratégie de modélisation RANS pour les éjecteurs supersoniques a été décrite en combinant la base de données pour les gaz réels NIST [NIST, 2010] et le modèle de turbulence $k - \omega$ SST dans sa formulation à bas nombre de Reynolds. L'approche proposée prédit avec un accord d'environ 5% (resp. 2%) le rapport d'entraînement (resp. rapport de compression) avec les données expérimentales de García del Valle *et al.* [2014]. Il capte également correctement les principales caractéristiques de l'écoulement interne et a un coût de calcul raisonnable. Ce modèle RANS a été appliqué à l'analyse d'un éjecteur supersonique au $R134a$ utilisé à des fins de réfrigération, montrant en particulier que le flux secondaire est entraîné par un transfert d'impulsion à travers la couche de cisaillement, que la position de départ des ondes de choc dans la section constante se situe dans une plage de 9 à 16 fois le diamètre de sortie de la buse primaire et que l'important caractère axial du flux limite le mélange des deux écoulements d'entrée au-delà du train d'ondes de choc. De plus, une analyse exergétique à travers le dispositif montre que le mélange et les ondes de choc obliques sont responsables de 50% et 70% des pertes générées, ces dernières pouvant être atténuées par injection de gouttelettes dans la section à zone constante. De plus, il a été démontré que le remplacement direct du fluide de travail par les HFO $R1234yf$ et $R1234ze(E)$ entraîne de légers changements dans la performance de l'éjecteur mais réduit en moyenne le COP du système HDRC (resp. la capacité de refroidissement) de 7.1% (resp. 23.3%). Enfin, une comparaison des prédictions du modèle avec le modèle thermodynamique de Galanis and Sorin [2016] pour un éjecteur à air montre que lorsque le fluide de travail se rapproche du comportement de gaz idéal, l'écoulement peut être normalisé en fonction de la température et de la pression à l'entrée secondaire, la gorge de la tuyère principale et les rapports d'entraînement et de compression.

Dans la seconde partie, l'influence des gouttelettes a été étudiée d'un point de vue local en étendant le modèle RANS à une phase discrète qui affecte le flux principal par des échanges de quantité de mouvement et d'énergie thermique, et d'un point de vue global en construisant un modèle thermodynamique qui prédit l'entraînement et le rapport de compression limitant étant donné une géométrie fixe et les conditions de fonctionnement. Les deux approches présentent un très bon accord en termes de profils internes de p, T et Ma. Les résultats pour un éjecteur supersonique au $R134a$ comme fluide de base, avec des gouttelettes injectées à mi-chemin dans la section de la zone constante, montrent que la structure d'écoulement dans cette région présente des changements perceptibles seulement à la fraction d'injection la plus élevée, 10%, en diminuant l'intensité du choc de 8% et la surchauffe à la sortie de l'éjecteur de 15 °C. Néanmoins, la performance de l'éjecteur est sévèrement affectée vu que le rapport de compression, l'efficacité d'Elbel et le performance exergétique sont réduites respectivement de 5%, 11% et 15%, principalement en raison de l'entropie supplémentaire générée par l'injection de gouttelettes et le mélange avec le flux principal.

Mots-clés : éjecteur supersonique, réfrigération, gouttelettes, CFD, model thermodynamique

ABSTRACT

This research project has as main objective to study in detail the internal flow features of single-phase supersonic ejectors for refrigeration applications, and the potential effects of injecting droplets on the performance of the device. To this end, a numerical approach is proposed which has been separated into two parts:

First, a RANS modelling strategy for supersonic ejectors has been outlined combining the NIST real gas equations database [NIST, 2010] and the $k-\omega$ SST turbulence model in its low-Reynolds number formulation. The proposed approach agrees within 5% (resp. 2%) to the experimental entrainment ratio (resp. compression ratio) data of García del Valle *et al.* [2014], properly captures the main internal flow features and has a reasonable computational cost. This RANS model has been applied in the analysis of a supersonic $R134a$ ejector for refrigeration purposes, showing in particular that the secondary flow is entrained by momentum transfer through the mixing shear layer, that the distance between the primary nozzle exit and the shock-waves in the constant area section varies between 9 and 16 times the primary nozzle exit diameter and that the important axial character of the flow limits mixing of both inlet flows until after the shock train. Furthermore, an exergy analysis through the device shows that the mixing and the oblique shock waves are responsible for between 50% and 70% of the generated losses, the latter might be attenuated through droplet injection in the constant area section. Moreover, it has been shown that drop-in replacement of the working fluid with HFOs $R1234yf$ and $R1234ze(E)$ leads to mild changes in the ejector performance but reduces the HDRC system COP (resp. cooling capacity) in average by 7.1% (resp. 23.3%). Lastly, a comparison of the model predictions with the thermodynamic model of Galanis and Sorin [2016] for an air ejector, shows that as the working fluid approaches the ideal gas behaviour, the flow can be adimensionalized in terms of the secondary inlet temperature and pressure, the motive nozzle throat and the entrainment and compression ratios.

In the second part, the influence of droplets has been studied from a local perspective by extending the RANS model to include a discrete phase, which affects the main flow through exchanges of momentum and thermal energy, and from a global perspective by building a thermodynamic model, which predicts the entrainment and limiting compression ratio given a fixed geometry and operating conditions. Both approaches present very good agreement in terms of p, T and Ma internal profiles. Results for a supersonic ejector with $R134a$ as baseline working fluid and droplets injected at the constant area section show that the flow structure has perceptible changes only at the highest injection fraction considered 10%, which induces boundary layer detachment, reduces the shock intensity by 8% and diminishes the superheat at the ejector outlet by 15 °C. Nonetheless, ejector performance metrics are severely affected as the limiting compression ratio, Elbel efficiency and exergy performance reduce respectively by 5%, 11% and 15%, due mainly to the additional entropy generated through droplet injection and mixing with the main flow.

Keywords: supersonic ejector, refrigeration, droplets, CFD, thermodynamic model

ACKNOWLEDGEMENTS

This thesis would not have been possible without the help of many people whom, at times unknowingly, gave me the exact push I needed towards this achievement. To all of you I am infinitely grateful, although I would like to specially acknowledge the contributions of the following people:

My supervisors, Dr. Zine Aidoun and Prof. Sébastien Poncet, for their patience, guidance and unconditional help. Your confidence in me was a constant source of motivation. And through your examples I have learned invaluable lessons, both for my academic and personal life.

To the examiners (in no particular order): Prof. Stéphane Moreau, Prof. Pierre Proulx, Prof. Stefan Elbel and Prof. Yann Bartosiewicz, for accepting their roles as examiners of this thesis. It is a honour to submit my work to the views of academics whom I consider references in their fields. Also to Prof. Nicolas Galanis, who showed great interest in this work since the beginning and did not hesitate to actively collaborate in its development.

On a personal level, I would like to show my appreciation to my friends and colleagues in the *LMFTEUS* group and in the Faculty. Specially to: Ghofrane, Maud, Alla-Eddine, Aurélien, David, Edwin, Ibai, Mauricio, Nizar and Yu. It has been a pleasure to work and share laughs, doubts, kicks and goals with all of you. I also thank the members of the *Groupe d'Aérocoustique*, in particular Marlène, for their help in setting up the cluster-based simulations, and *CERFACS* for providing the AVBP code used in the LES cases.

And last but not least, to my family, specially my wife Beatriz and my little sister Sara (*AOYS*). For all your unconditional love and confidence, despite my senselessness throughout the years.

TABLE OF CONTENTS

LIST OF FIGURES

LIST OF TABLES

LIST OF SYMBOLS

Symbol	**Definition**
a	Speed of sound [m/s]
A_{ratio}	Area ratio [-]
b	Generic flow quantity
c_p	Isobaric specific heat [kJ/kg/K]
c_v	Isochoric specific heat [kJ/kg/K]
C_D	Droplet drag coefficient [-]
d	Primary nozzle exit diameter [mm]
D	Constant section chamber diameter [mm]
$\mathcal{D}_\omega$	Specific dissipation rate destruction [kg/m^3/s^2]
e	Specific internal energy [kJ/kg]
e_d	Diffuser exit diameter [mm]
F_D	Drag forces acting on a particle [N]
h	Static enthalpy [kJ/kg]
h_p	Convection heat transfer coefficient for a particle [W/m^2]
k	Turbulence kinetic energy [m^2/s^2]
l	Constant section chamber length [mm]
L	Subsonic diffuser length [mm]
$\dot{m}$	Mass flow rate [kg/s]
Ma	Mach number [-]
M_{ch}	Momentum interphase exchange [N]
n_d	Primary nozzle throat diameter [mm]
Nu	Nusselt numer [-]
Oh	Ohnesorge number [-]
p	Pressure [kPa]
p_{lim}	Limiting Pressure [kPa]
P_{ratio}	Pressure ratio / Compression ratio [-]
PM	Molar mass [-]
Pr	Prandtl number [-]
$\mathcal{P}$	Turbulence kinetic energy production [m^2/s^3]
$\mathcal{P}_\omega$	Turbulent specific dissipation rate production [kg/m^3/s^2]
q	Specific heat transferred [kJ/kg]
Q_{ch}	Thermal energy interphase exchange [J]
R_u	Universal gas constant [$= 8.3145\,$kJ/kmol/K]
R	Gas Constant $= \frac{R_u}{PM}$ [kJ/kg/K]
Re	Reynolds number [-]
s	Specific entropy [kJ/kg/K]
$\dot{S}$	Entropy flow rate [kW/kg/K]
S_e	Surface transfer area [m^2]
S_{ij}	Strain rate tensor [m/s]
t_f	Final time [s]

Symbol	**Definition**
t_o	Initial time [s]
T_{red}	Reduced temperature [-]
u	Axial flow velocity [m/s]
u^+	Dimensionless tangent velocity [-]
y	Normal wall distance [m]
y^+	Dimensionless wall coordinate [-]
Y_m	Turbulence compressibility effects [kg/m/s^3]
w	Specific work [kJ/kg]
W_S	Shock wave velocity [m/s]
We	Weber number [-]
x	Axial coordinate [m]
$\mathcal{X}_\omega$	Turbulent specific dissipation rate cross-diffusion [kg/m^3/s^2]

Greek characters	
ϵ	Turbulence dissipation rate [m^2/s^3]
η_{Elbel}	Elbel's ejector efficiency [-]
η_{prim}	Primary nozzle isentropic efficiency [-]
η_{sec}	Secondary inlet isentropic efficiency [-]
η_{mix}	Mixing efficiency [-]
η_{diff}	Diffuser isentropic efficiency [-]
η_χ	Exergy efficiency [-]
λ	Thermal conductivity [W/m/K]
Λ	Wavelength of fastest growing waves in the WAVE model [m]
μ	Laminar viscosity [Pa s]
ν	Kinematic laminar viscosity [m^2/s]
ξ	Exergy destruction index [-]
ρ	Density [kg/m^3]
σ	Surface tension [N/m]
σ_i	Turbulent Prandtl number for quantity i [-]
τ_d	Breakup time [s]
τ_{ij}	Viscous stress tensor [N/m^2]
ϕ	Droplet diameter [µm]
Φ_1	Losses coefficient in the primary nozzle [-]
Φ_2	Losses coefficient at the mixing chamber [-]
Φ_3	Losses coefficient at the subsonic diffuser [-]
$\dot{\chi}$	Exergy flow rate [kW]
ω_r	Entrainment ratio [-]
ω	Turbulent specific dissipation rate [s^{-1}]
Ω	Accentric factor [-]
Ω_{max}	Maximum wave growth rate [s^{-1}]

Subscripts	
i, j, k	Coordinate directions
out	Outlet

Symbol	**Definition**
p	Particle
$prim$	Primary inlet
sec	Secondary inlet
t	Turbulent
$'$	Turbulent fluctuations (Reynolds averaging)
$''$	Turbulent fluctuations (Favre averaging)

Superscripts

is	Isentropic process
sat	Saturation conditions

LIST OF ACRONYMS

Acronym	**Definition**
CAS	Constant Area Section
CFD	Computational Fluid Dynamics
COP	Coefficient of performance
EERC	Ejector Expansion Refrigeration Cycle
EoS	Equation of State
FANS	Favre Averaged Navier-Stokes
HFC	Hydro-fluorocarbons
HFO	Hydrofluoroolefins
HDRC	Heat Driven Refrigeration Cycle
HVAC	Heating, Ventilation and Air Conditioning
LES	Large Eddy Simulation
NXP	Nozzle Exit Plane
NS	Navier-Stokes
OP	Operating Point
RANS	Reynolds Averaged Navier-Stokes
RKS	Redlich-Kwong-Soave Equation of State

PART I

INTRODUCTION

CHAPTER 1

SCOPE

1.1 Context and Problem Description

The current energy and environmental world scenario demands for a more efficient use of natural resources which, in combination with a political will to reduce greenhouse gas emissions, drives many initiatives to increase the efficiency of industrial processes. Particularly in the refrigeration industry, the objective is to replace refrigerants with a high environmental impact and develop systems with reduced energy consumption. In this regard, supersonic ejectors have gained a renewed interest in recent years for their use in novel refrigeration systems, where they can operate in single-phase mode as compressor substitutes, or in two-phase mode harvesting the energy usually wasted in the throttling valve. Both alternatives result in cycles potentially more efficient, simpler to operate, less energy demanding and less polluting than the standard compressor-based refrigeration cycle.

In an ejector, a secondary flow is entrained and compressed by interactions with a supersonic primary or motive flow. The device does not have any moving parts, is of simple design and in single-phase configurations can be driven by low-grade energy sources such as waste heat. These characteristics make it an interesting component for energy integration applications in a wide range of industries. To date, global features of supersonic ejectors have been extensively studied both experimentally and numerically. Thus, within the long term objective of enhancing the efficiency of ejector-based systems, the interest now shifts towards particular aspects that hinder its performance and competitiveness.

The first step in this direction is to better understand the internal flow features and exergy transfer mechanisms within a single-phase supersonic ejector. To this end, Computational Fluid Dynamics (CFD) techniques have proven to be an excellent tool, providing much more details than what can be attained by experimental methods, albeit their reliability is very much dependant on the quality of the assumptions required to achieve a computationally feasible model. This is particularly true for supersonic ejectors where the internal flow complexity has prevented a definite consensus on a reliable benchmark numerical approach for their study.

One of these issues is the effect that the presence of droplets might have on its internal flow features and, ultimately, on the system performance. Droplets at low concentrations ($< 10\%$ relative to the primary inlet mass flow rate), either generated from spontaneous condensation or injected through the ejector walls, could mitigate two phenomena responsible for 40% each of the losses generated in the device: the velocity mismatch in the mixing region [Al-Ansary and Jeter, 2004] and the intensity of shock waves before the diffuser [Jourdan *et al.*, 2010]. Although the interaction of droplets with gaseous supersonic flows has been studied in other fields with promissory changes to flow properties and shock wave intensity [Chauvin *et al.*, 2011; Yang *et al.*, 2010], their particular effects on ejectors have not been thoroughly analysed and the few existing publications provide inconclusive results [Al-Ansary and Jeter, 2004; Hemidi *et al.*, 2009a; Little and Garimella, 2016].

This outlook poses a couple of issues to be addressed by this thesis: firstly, the definition of a proper RANS model, offering the best compromise in terms of accuracy versus computational costs to predict the internal flow features of supersonic ejectors; secondly, to assess and discuss the influence of droplets on the internal flow features of supersonic ejectors and their potential benefits for ejector-based refrigeration systems.

1.2 Objectives and Originality

This research project proposes to study in detail the main internal flow features of single-phase supersonic ejectors for refrigeration applications, and the potential effects of injecting droplets on the performance of the device. To this end, the following points are introduced which, to date, have not been discussed in the literature concerning single-phase ejectors:

- A benchmark study combining different choices of turbulence and gas properties models for numerical modelling of supersonic ejectors working with real gas refrigerants, determining the best option in terms of accuracy versus computational costs. The $k-\omega$ SST turbulence model in its low-Reynolds number formulation is compared to the more commonly used high-Reynolds number formulations in terms of global accuracy and flow structure predictions.
- A numerical assessment of the changes occurring in ejector entrainment ratio and refrigeration cycle performance when a drop-in substitution of HFC refrigerants with HFO fluids is carried out.

- — A vis-a-vis discussion of the validity of common assumptions made by thermodynamic models of single-phase ejectors working with perfect or real gases against the RANS model results.
- — The extension of the supersonic ejector RANS model to represent the droplet-main gas interactions using a Lagrangian approach.
- — A study on the effects on internal flow properties resulting from injecting droplets in the constant area section of supersonic ejectors for refrigeration applications, and their influence on ejector pressure ratio and efficiency.

1.3 Thesis Outline

This text is structured as follows: Part I comprehends an introduction to the problem and main assumptions, with a review of the most relevant literature on operation, performance characteristics and local features of supersonic ejector flows (Chapter 2); Part II describes the methodology followed by the development of both the RANS model (Chapter 3) and the thermodynamic model for studying the effects of droplets (Chapter 4); Results are presented in Part III, starting with an analysis of the main flow features in single-phase ejectors in Chapter 5, followed by the study on the influence of droplet injection on the performance of ejectors for refrigeration purposes in Chapter 6. Finally, future perspectives and conclusions are presented in Chapter 7, including a first look at 3D Large Eddy Simulation results of a supersonic air ejector.

CHAPTER 2

STATE OF THE ART

This chapter comprises a general outlook of single-phase supersonic ejectors. Their working principle and most common applications in the refrigeration industry are presented first, followed by a description of important performance parameters and their relation with typical operating conditions. Afterwards, the current state of the art on experimental and numerical approaches to study the inner flow features of single-phase supersonic ejectors is presented. Finally, the assumptions concerning the injection of droplets on single-phase ejectors and their potential effects on performance are introduced.

2.1 General Context of Supersonic Ejectors

A supersonic ejector is a simple device which uses the energy of a primary flow (*i.e.*: motive flow) to compress a secondary flow without requiring any moving parts. It consists essentially in a convergent-divergent nozzle followed by a mixing chamber and a diffuser, disposed as shown in Figure 2.1. Photographs of the components and assembly of a single-phase supersonic ejector are shown in Figure 2.2.

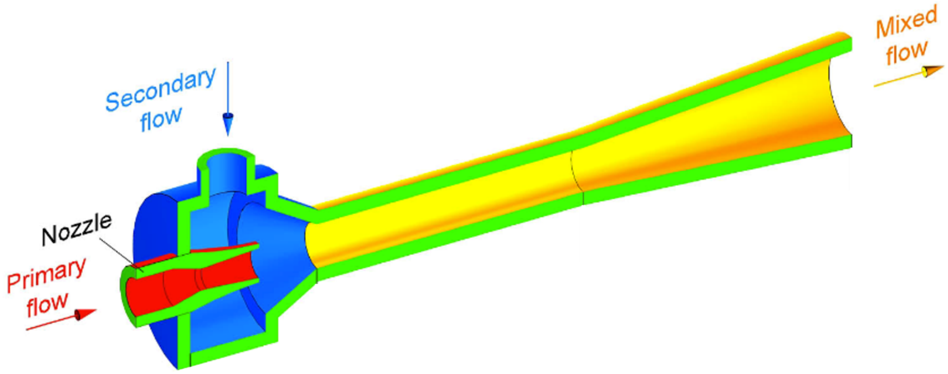

Figure 2.1 Schematics of a typical supersonic ejector geometry. After ERTC [2016].

The motive flow, coming from a reservoir at relatively high pressure and temperature, is accelerated into the mixing chamber, where it entrains the secondary flow along the constant area section (CAS). Afterwards, a series of supersonic shock waves take place before the mixture is further compressed in the diffuser to outlet conditions. The process

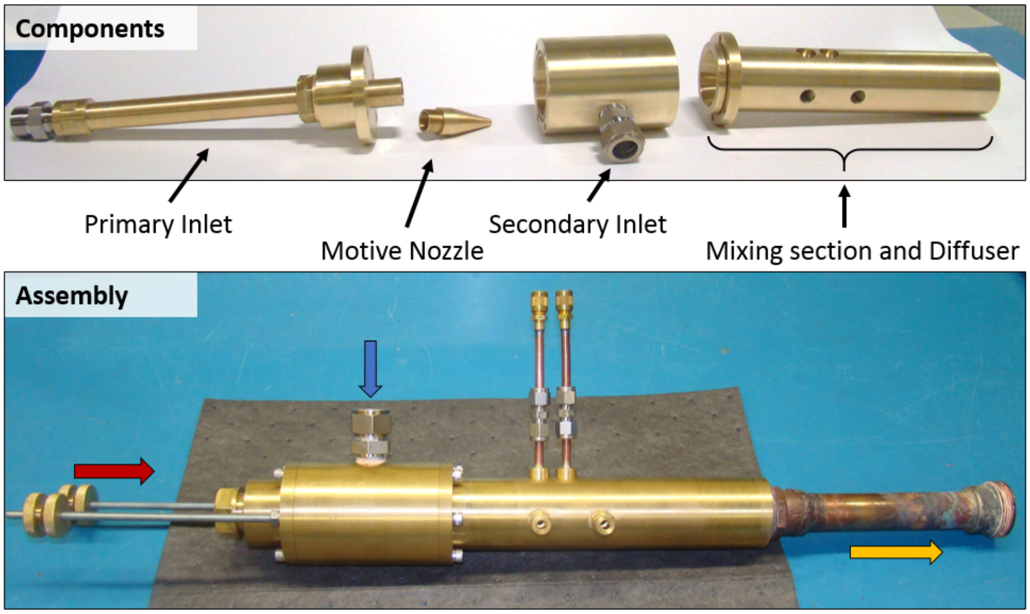

Figure 2.2 Components and assembly of a single-phase $R134a$ supersonic ejector for refrigeration applications. Courtesy of the CanmetEnergy research centre in Varennes (QC).

can be illustrated through the representative Mach number Ma and static pressure p profiles depicted in Figure 2.3, along with the definition of its main geometrical parameters.

2.2 Applications

Ejectors are of simple design and maintenance, do not have any moving parts, can be powered by low-grade energy sources (e.g.: solar thermal energy or rejected heat from an industrial process) and are highly reliable in handling phase-changing and two-phase mixtures. Thus, they have been considered as an alternative for energy integration schemes in a wide range of industries, *e.g.*: novel CO_2 capture [Reddick *et al.*, 2014] and desalination processes [Samaké *et al.*, 2014], revamping of galvanic plants to blast furnace gas plants [Besagni *et al.*, 2015], emergency systems in nuclear plants [Abe and Shibayama, 2014], exploitation of low pressure gas reservoirs [Chong *et al.*, 2009] and gas mixing inside SCUBA diving breathing apparatus [Cornman and Bliss, 2012]. An in-depth review of ejector application technologies up to 2015 can be found in Besagni *et al.* [2016].

Based on the amount of related publications during the last two decades, the most popular application for ejectors is in alternate refrigeration systems which, in general, are best performing and less pollutant than standard vapour compression cycles [Bilir Sag *et al.*, 2015]. Depending on the ejector role within the cycle, the two most common alternative

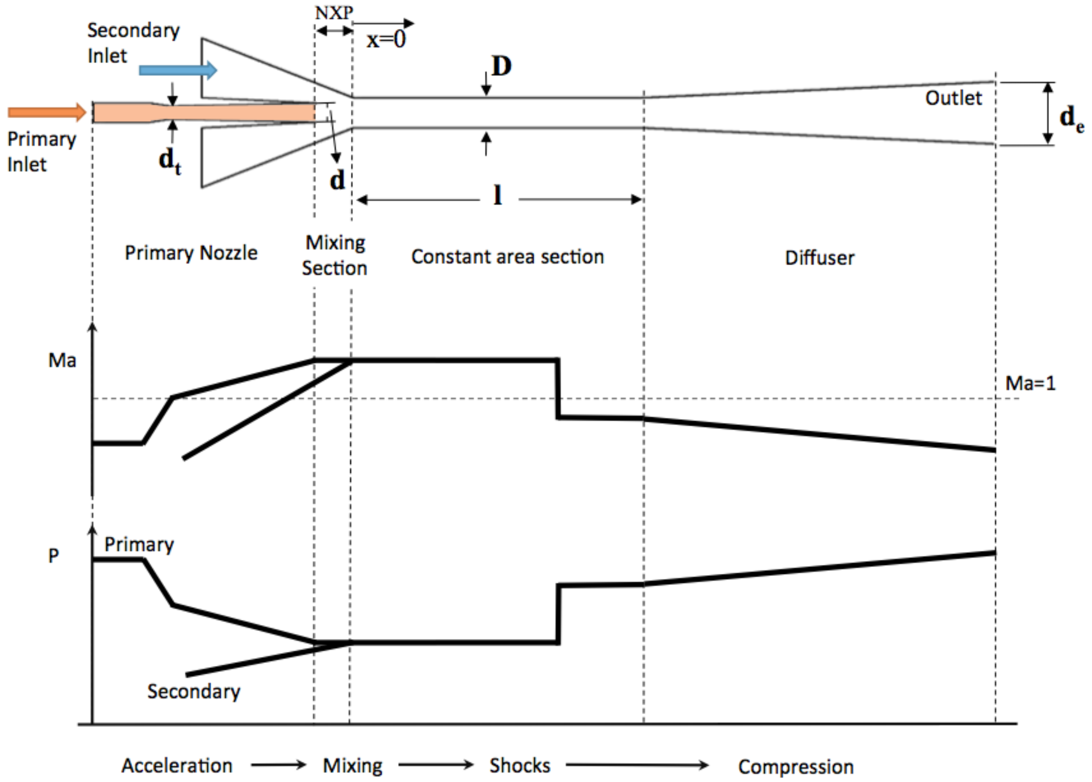

Figure 2.3 Mach number and pressure profiles through a supersonic single-phase ejector process. After Chunnanond and Aphornratana [2004]

refrigeration cycles are: the Heat Driven Refrigeration Cycle (HDRC), where a single-phase ejector substitutes the compressor, and the Ejector Expansion Refrigeration Cycle (EERC), where a two-phase ejector is used to harvest the energy lost at the trottling valve [Sumeru *et al.*, 2012].

2.2.1 The Heat Driven Refrigeration Cycle

The flow in a HDRC follows the configuration shown in Figure 2.4. It can be regarded as a standard refrigeration cycle (streams $1-2-3-5-6$) with the compressor substituted by a top loop conformed by the condenser, pump, generator and ejector (streams $1-2-3-4$). Being driven by low grade thermal energy (the pump represents barely 5% of the cycle energy consumption [Fang *et al.*, 2017]), the HDRC is a very environmentally friendly cycle although with a modest performance. Chunnanond and Aphornratana [2004] report a system Coefficient of Performance (COP) between ~ 0.28 and ~ 0.5 in a steam HDRC with 3 kW of cooling capacity and evaporator and generator temperatures in the ranges 5 °C to 15 °C and 110 °C to 150 °C respectively. Under similar conditions, Thongtip *et al.* [2014] report a maximum COP of 0.45 , at generator and evaporator temperatures of 110 °C and

17 °C respectively. The authors also observed a linear relationship between the evaporator temperature and the system cooling capacity, independently of the generator temperature and the ejector primary nozzle size.

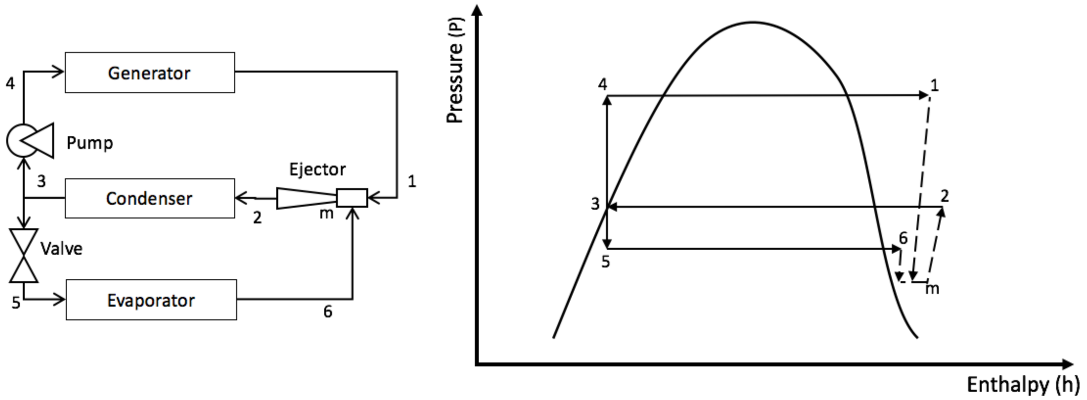

Figure 2.4 Schematics and Pressure-Enthalpy diagram of the Heat Driven Refrigeration Cycle. The dashed lines denote the streams through the ejector.

Common working fluids for these cycles are HFC refrigerants such as $R134a$ and $R245fa$, which are highly stable, non-toxic and non-flammable. In terms of performance, slight differences can be observed: Selvaraju and Mani [2006] report a COP between 0.1 and 0.5 for a $R134a$ HDRC with a nominal cooling capacity of 0.5 kW, evaporator temperatures between 5 °C and 12 °C and generator temperatures between 65 °C and 90 °C; whereas with $R245fa$ a COP as high as 0.6 has been reached for generator and evaporator temperatures of 90 °C and 10 °C respectively [Mazzelli and Milazzo, 2015]. HFC refrigerants will be progressively banned in the coming years in favour of HFO fluids such as $R1234yf$ and $R1234ze(E)$, which have a much lower global warming potential [Parliament and Council, 2014]. Experimental studies on drop-in replacement of these refrigerants exhibited mitigated results regarding their impact on the COP of standard cycles [Ansari *et al.*, 2013; Jarall, 2012; Ozgur *et al.*, 2012]. A theoretical assessment of the effects of using HFO refrigerants $R1234yf$ and $R1234ze(E)$ instead of $R134a$ on a HDRC system, along with CFD results of the changes in internal ejector flow configuration, is presented in Chapter 5.

2.2.2 The Ejector Expansion Refrigeration Cycle

In an EERC, the expansion valve is substituted by an ejector and a phase separator, resulting in the configuration shown in Figure 2.5. This modification brings some advantages in comparison to the standard cycle: first, the flow coming from the condenser is expanded in an isentropic rather than isenthalpic process; second, the energy released during this expansion is not entirely wasted, but used to compress the flow serving the bottoming refrigeration sub-cycle (streams $2 - 5 - 6 - 7$); finally, the quality at the evaporator inlet is much lower, rendering a higher specific enthalpy available for heat extraction. The addition of all these effects is a refrigeration process systematically more efficient than the standard cycle under the same operating conditions [Lawrence and Elbel, 2013].

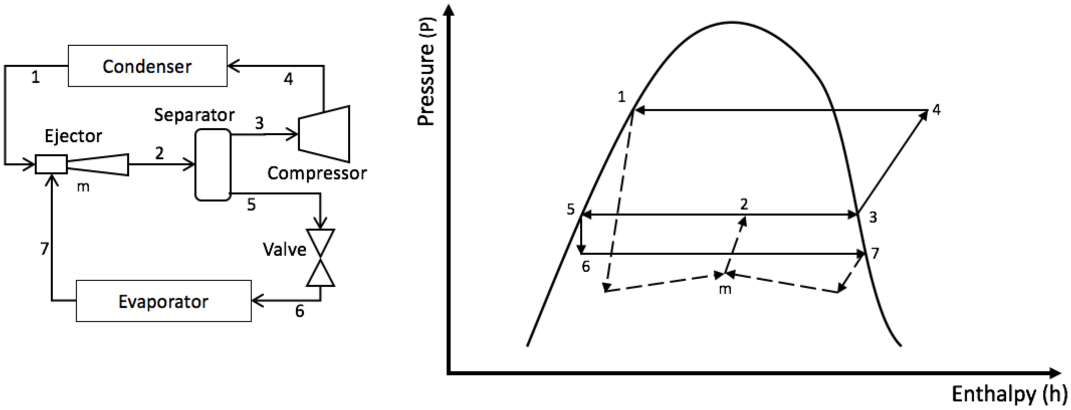

Figure 2.5 Schematics and Pressure-Enthalpy diagram of the Ejector Expansion Refrigeration Cycle. The dashed lines denote the streams through the ejector.

The first experimental comparisons of EERCs versus standard cycles were carried out by Menegay and Kornhauser [1996] in the context of a typical HVAC system with $R12$. Initial tests showed the EERC had worst performance, which the authors related to the use of an ejector designed for single-phase conditions. Over a range of evaporator (resp. condenser) temperatures of 8 °C to 16 °C(resp. 27 °C to 37 °C), $R134a$ EERC systems with a correctly designed ejector are able to provide performances 10% to 11% higher than the standard cycle [Disawas and Wongwises, 2004; Reddick *et al.*, 2012], particularly at lower condenser temperatures. A direct comparison of EERC systems with different working fluids shows that higher COPs are achieved with $R1234fa$ and $R134a$, respectively 12% and 8% over the same cycle with CO_2. Yet, the latter is more popular given its higher work recovery rate [Lawrence and Elbel, 2014].

The COP for these systems relates the cooling benefit to the invested energy, namely the heat extracted in the evaporator ($\dot{q}_{evaporator}$) to the compressor work ($\dot{w}_{compressor}$) in the case of EERCs or to the generator heat input ($\dot{q}_{generator}$) pump work ($\dot{w}_{pump}$) in the case of HDRCs. It can be easily shown that the system COP depends directly on the ejector entrainment ratio (ω_r, the ratio of secondary to primary mass flows, Section 2.3). For the HDRC (Figure 2.4):

$$COP_{HDRC} = \omega_r \frac{q_{evaporator}}{q_{generator} + w_{pump}}, \tag{2.1}$$

and for the EERC (Figure 2.5):

$$COP_{EERC} = \omega_r \frac{q_{evaporator}}{w_{compressor}}. \tag{2.2}$$

It is clear that better understanding the influence of operating conditions and design parameters on ejector performance is crucial to enhance the competitiveness of alternative refrigeration cycles.

2.3 Ejector Performance

2.3.1 Entrainment and Compression Ratios

From a secondary flow perspective, the ejector is a compressing device with its performance measured in terms of the entrainment ratio [ω_r, Eq. (2.3)] and the compression ratio [P_{ratio}, Eq. (2.4)]. These reflect, respectively, the entraining and compressing capabilities of the device:

$$\omega_r = \frac{\dot{m}_{sec}}{\dot{m}_{prim}}, \tag{2.3}$$

$$P_{ratio} = \frac{p_{out}}{p_{sec}}. \tag{2.4}$$

p and $\dot{m}$ are respectively the pressure and mass flow rate measured at the primary inlet ($prim$), the secondary inlet (sec) or the outlet of the ejector (out).

Figure 2.6 shows a typical ejector operating curve with ω_r as a function of the outlet pressure (p_{out}) for fixed inlet conditions. Three zones are identified: double-choke or on-design, single-choke or off-design and malfunction. During on-design operation, both motive and secondary flows are choked, making the entrainment ratio dependent only on inlet conditions. This regime persists until the outlet pressure equals the limit p_{lim}, where the secondary flow is no longer choked and its mass flow rate decreases with p_{out}. At the point where the outlet pressure is so high that the primary flow deviates towards the secondary inlet, the ejector enters the malfunction zone [Eames *et al.*, 1995].

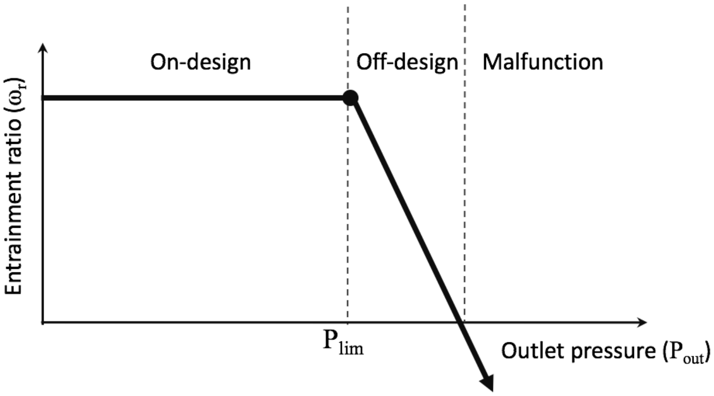

Figure 2.6 Typical ejector operating curve for increasing outlet pressure. After Chunnanond and Aphornratana [2004]

In the context of refrigeration systems, primary and secondary inlet pressures are typically defined by the generator and evaporator temperatures, affecting both the entrainment and compression ratios. As it is shown in Figure 2.7 [Chunnanond and Aphornratana, 2004], while a higher secondary pressure increases both ω_r and p_{lim}, augmenting the primary pressure increases p_{lim} but reduces ω_r. These effects are related to the primary jet expansion in the mixing section as discussed in Section 2.4.2.

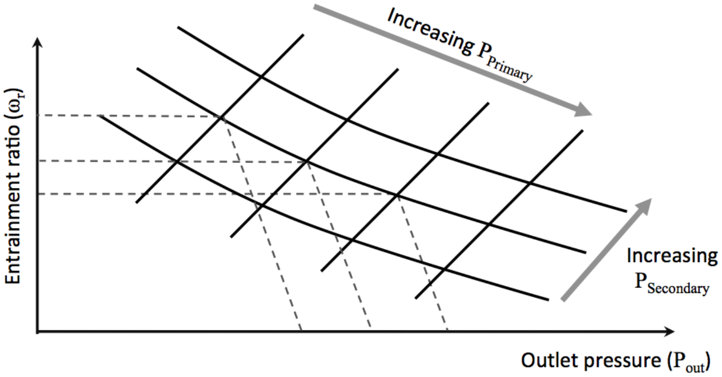

Figure 2.7 Typical ejector operating map: ω_r as a function of inlet and outlet pressures.

In terms of geometrical parameters, the ejector performance is usually linked to the area ratio (A_r, the ratio of the CAS to nozzle throat cross sections), the nozzle exit position (NXP) and the constant area section length (l) as defined in Figure 2.3. Depending on the NXP and main section design, two mixing process alternatives can be considered [Keenan, 1950]: constant pressure mixing and constant area mixing (see Figure 2.8). The former is often preferred given its higher ω_r under the same operating conditions [Chunnanond and Aphornratana, 2004]. In particular for single phase $R134a$ ejectors, the use of a constant pressure design increases in average the entrainment ratio by 20% but reduces the limiting pressure by 8% [García del Valle *et al.*, 2014]. Nonetheless, the constant area design is more sensitive to variations in the nozzle exit position, which makes it a suitable option for ejector control. On this regard, a maximum entrainment ratio has been observed when the NXP locates slightly before the start of the CAS on air [Chong *et al.*, 2014] and $R134a$ ejectors [García del Valle *et al.*, 2014]. Moving further away the nozzle reduces both ω_r and p_{lim}, although the latter has an opposite tendency in two-phase devices [Sriveerakul *et al.*, 2007]. The effect is barely noticeable in constant pressure mixing designs.

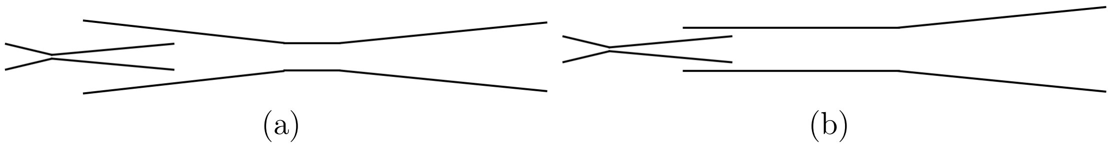
(a) (b)

Figure 2.8 Mixing section design alternatives: (a) Constant pressure, (b) Constant area.

2.3.2 Ejector Efficiency

The use of the entrainment and compression ratios for quantifying the effectiveness or convenience of a particular design over other alternatives is limited. Hence, various efficiency definitions have been proposed, differing particularly on their interpretation of the energy accounting and the required states for their computation. A few notable efficiency parameters will be defined in the following. A thorough comparison of several performance definitions can be found in the review of Lawrence and Elbel [2015].

For single-phase ejectors, a commonly used efficiency definition is that given by the American Society of Heating, Refrigerating and Air-Conditioning Engineers [ASHRAE, 1983], which divides the power gained in the compression of the total mass flow, from secondary inlet to outlet conditions, by the power made available via the isentropic expansion of the motive flow from primary inlet to outlet conditions [η_{ASHRAE}, Eq. (2.5)]:

$$\eta_{ASHRAE} = (1+\omega_r)\,\frac{h_{out}-h_{sec}}{h_{prim}-h_{out}^{is,prim}}, \tag{2.5}$$

where h is the static enthalpy at the subscript marked boundaries and the superscript $is, prim$ denotes the static enthalpy resulting from an isentropic process starting at the primary inlet conditions. Although Eq. (2.5) works well for single-phase ejectors, the large enthalpy differences between saturated liquid and vapour hinder its application in two-phase ejectors [Lawrence and Elbel, 2015]. For these cases, Elbel and Hrnjak [2008] proposed a more appropriate definition (η_{Elbel}) based on the ratio of the isentropic compression work of the entrained flow to the work available through the isentropic expansion of the primary flow:

$$\eta_{Elbel} = \omega_r \frac{h_{out}^{is,sec} - h_{sec}}{h_{prim} - h_{out}^{is,prim}}. \tag{2.6}$$

Note that the denominator in Eq. (2.6) is the work difference existing between the isentropic and isenthalpic expansions of the motive flow.

2.3.3 Second Law Analysis

The ejector performance is often assessed via entropy and exergy accounting, which allows to make comparisons with other processes and locate irreversibility sources. For instance, Banasiak *et al.* [2014] introduced the parameter ζ_{Ej} which quantifies the entropy increase avoided with the use of an ejector relative to a reference process:

$$\zeta_{Ej} = 1 - \frac{\Delta S_{ej}}{\Delta S_{ref}}, \tag{2.7}$$

where ΔS_{ej} and ΔS_{ref} are the generated entropies across the ejector and reference process respectively. In the case of an EERC, ΔS_{ref} represents the throttling stage of a standard refrigeration cycle under the same operating conditions. For an experimental EERC with CO_2, Banasiak *et al.* [2014] observed ζ_{Ej} in the range -0.062 to 0.223. Negative ζ_{Ej} values mean that more irreversibilities were generated across the ejector than the reference. Such negative effect translated into a poor Elbel efficiency ($\eta_{Elbel} = 2.1\%$ to 23.4%).

Another useful Second Law performance parameter is the exergy efficiency η_χ, the ratio of outlet to input exergy flow rates:

$$\eta_\chi = \frac{\dot{\chi}_{out}}{\dot{\chi}_{prim} + \dot{\chi}_{sec}}, \tag{2.8}$$

with $\dot{\chi}_i$ being the exergy flow rate, *i.e.*: the maximum work rate theoretically available between the thermodynamic conditions at surface i and a reference *dead state* 0:

$$\dot{\chi}_i = \dot{m}_i[(h_i - h_0) - T_0(s_i - s_0)]. \tag{2.9}$$

Typical dead state choices for isolated ejector studies are the secondary inlet state or the working fluid at normal conditions (1 atm and 15 °C). For refrigeration cycles, it is usual to choose the condenser inlet conditions.

The value of η_χ represents the amount of potential work recovered using an ejector. Bilir Sag *et al.* [2015] measured $\eta_\chi \sim 98\%$ and $\eta_{Elbel} \sim 40\%$ for an EERC with $R134a$. The exergy efficiency of the whole EERC was in average 17.5%, always two points over that of the standard refrigeration system tested under the same operating conditions.

A local assessment of the ejector, pinpointing sources of losses through the device, can be made via the exergy destruction index, ξ_j, which relates the exergy wasted between the inlet and outlet of a given ejector section $\dot{D}_j$ to the total total lost across the device $\dot{D}_{ej}$:

$$\xi = \frac{\dot{D}_j}{\dot{D}_{ej}} = \frac{\dot{S}_{j,start} - \dot{S}_{j,end}}{\dot{S}_{out} - \dot{S}_{prim} - \dot{S}_{sec}}, \tag{2.10}$$

where $\dot{S}_k = \dot{m} s_k$ is the total entropy flow rate at boundary k.

2.4 Internal Flow Features

Efforts to better understand the relationships between the ejector internal flow features and its performance have been made with different approaches, each with its strengths and weaknesses. On one hand, experimental studies are often limited to a global analysis (*e.g.*: ω_r vs. operating conditions) given the constraints of experimental test benches, though with a few exceptions. On the other hand, thermodynamic and CFD approaches provide better understanding of the ejector internal features but their proper validation can be difficult.

2.4.1 Experimental Visualizations

Fabri and Siestrunck [1958] performed a pioneer study of an air ejector obtaining Schlieren images of the mixing section. Changes in the primary jet structure were observed for different regimes. In particular, as shown in Figure 2.9, increased instabilities of the jet core and a contraction in the first shock cell were captured at the transition from double- to single-choke operation.

The primary jet structure is indirectly governed by the primary inlet to outlet pressure ratio through p_{NXP} and p_b, respectively the pressures at the NXP and mixing chamber

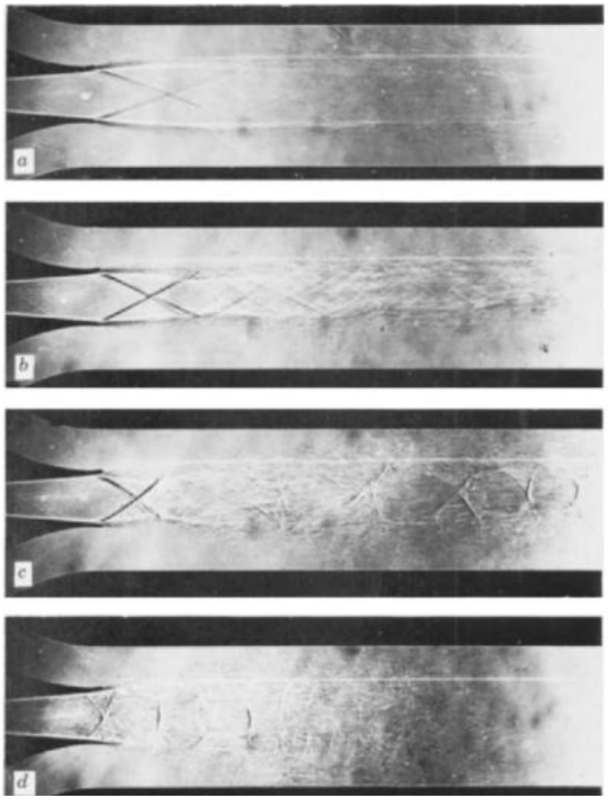

Figure 2.9 Schlieren images of the flow structure leaving the primary nozzle at different regimes: (a) On-design, (b) Critical operation, (c,d) Off-design. Extracted from Fabri and Siestrunck [1958].

inlet. It has been observed that, depending on the motive pressure, the primary jet potential zone extends 8 to 13 times the nozzle exit diameter [Marinovski *et al.*, 2009] and that the first shock cell length increases linearly with p_{prim} [Zhu and Jiang, 2014a]. These and other mixing section features have been captured by Bouhanguel *et al.* [2011] using laser tomography techniques based on a combination of illumination sources and scatter tracers injected in the secondary inlet of a supersonic air ejector. This approach allows to distinguish both permanent and instantaneous phenomena such as non-mixing length variations with primary inlet pressure [Figure 2.10(a)] and motive jet fluctuations [Figure 2.10(b)].

Apart from the flow passage available between the primary jet and the ejector walls, the entrainment ratio has also been linked to the turbulent intensity and spreading rate of the shear mixing layer by Rao and Jagadeesh [2014], through comparisons of the entrainment and compression ratios of air ejectors with different primary nozzle exit designs: conical, lobbed and ring at the nozzle tip. A gain of up to 30% in entrainment ratio was achieved with the lobbed and ring on the nozzle configurations which, as shown in Figure 2.11,

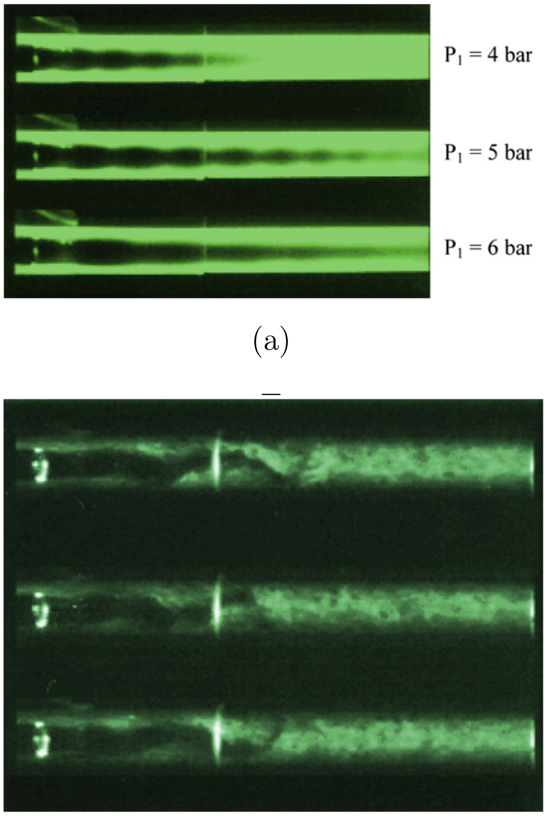

(a)

(b)

Figure 2.10 Phenomena in the mixing section of a supersonic ejector captured by Bouhanguel *et al.* [2011]: (a) Variations in the non-mixing region length with primary inlet pressure, produced with a combination of fluorescent tracers in the secondary flow and a camera equipped with band-pass light filters, (b) Primary jet plume fluctuations, produced with a combination of depolarizing tracers in the secondary flow and pulsed illumination ($\Delta t = 0.1$s).

trigger a greater turbulent activity. Nonetheless, these designs also resulted in 15% to 50% reduction in compression ratio, due to important losses in stagnation pressure.

Although various techniques permit to distinguish important internal flow features in the mixing and diffuser section of ejector, their quantification has been more difficult. Attempts have been made to extract the center line pressure profiles with capillary tubes but it greatly disturbs the flow structure [Bartosiewicz *et al.*, 2005]. Alternative methods using flush-mounted wall pressure transducers have been performed without incurring in noticeable flow disturbances [García del Valle *et al.*, 2015], producing wall pressure profiles such as those shown in Figure 2.12 for a single-phase $R134a$ supersonic ejector. These would allow to estimate for example the shock intensity and position based on the abrupt pressure changes in double-choke operation (*e.g.*: x between 40 mm and 50 mm

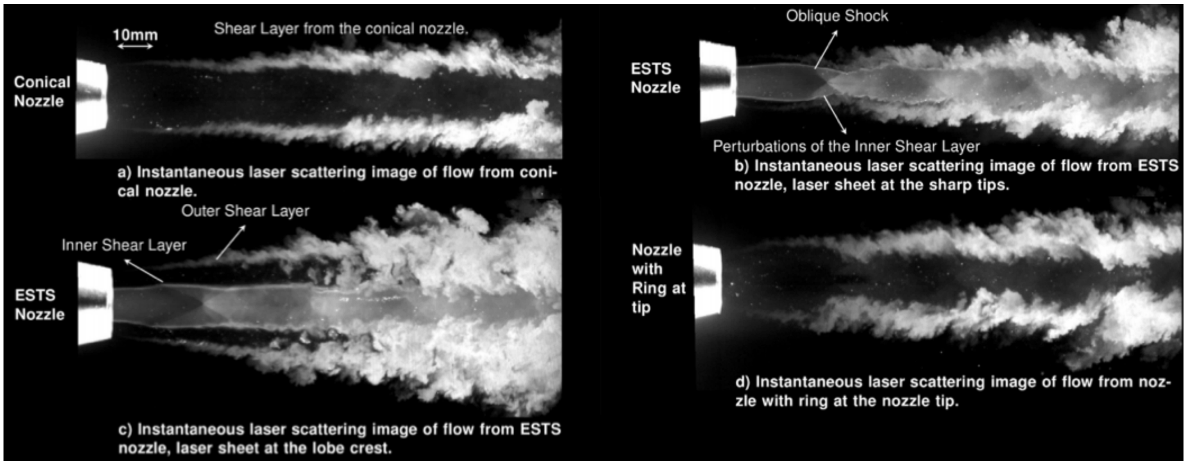

Figure 2.11 Turbulent shear layer developing at the nozzle tip for three different nozzle exit designs: (a) conical nozzle, (b,c) lobbed nozzle, (d) ring at the nozzle tip. After Rao and Jagadeesh [2014].

in Figure 2.12) although with some uncertainty. Ideally, these results in combination with accurate numerical models offer the best approach to study with great detail ejector internal flow features.

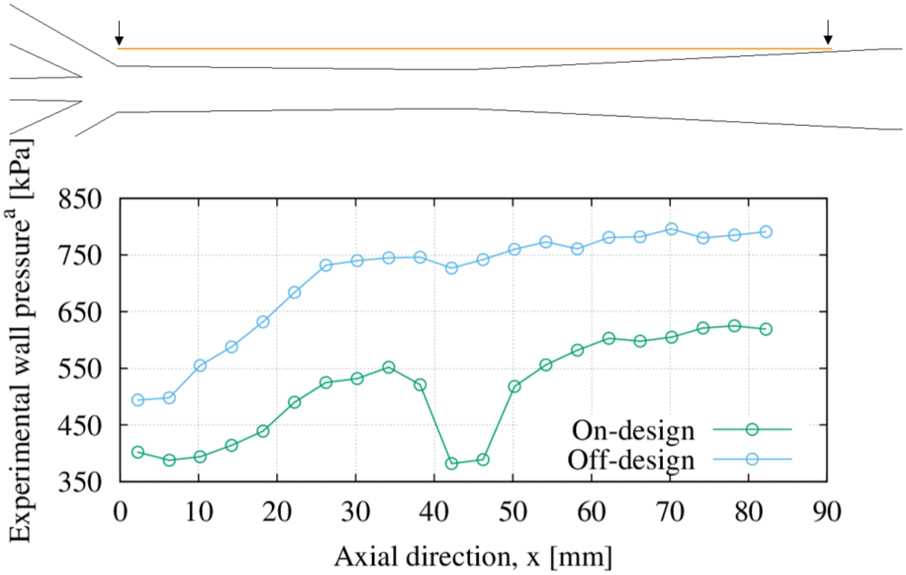

Figure 2.12 Wall pressure profiles in the mixing and diffuser sections of a $R134a$ constant pressure mixing ejector at on-design and off-design operations. ^{a}Experimental data after García del Valle *et al.* [2015]

2.4.2 Thermodynamic models

Early ejector thermodynamic models (*i.e.*: $0D$ and $1D$ models) use simple mathematical approaches to estimate the influence of geometry and operating conditions on the system performance. These are often based on integral formulations of the mass, momentum and energy conservation equations applied to characteristic sections of the device, namely: primary nozzle, secondary nozzle, mixing chamber, diffuser. A key point in the development of these models has been the *Effective Area* hypothesis proposed by Munday and Bagster [1977], which states that along on-design conditions the secondary flow chokes at an effective area A_{eff} between the motive jet and the mixing chamber walls (Figure 2.13). Such that the double-choke entrainment ratio is determined by the throat areas for primary and secondary flows, respectively the motive nozzle throat and A_{eff}.

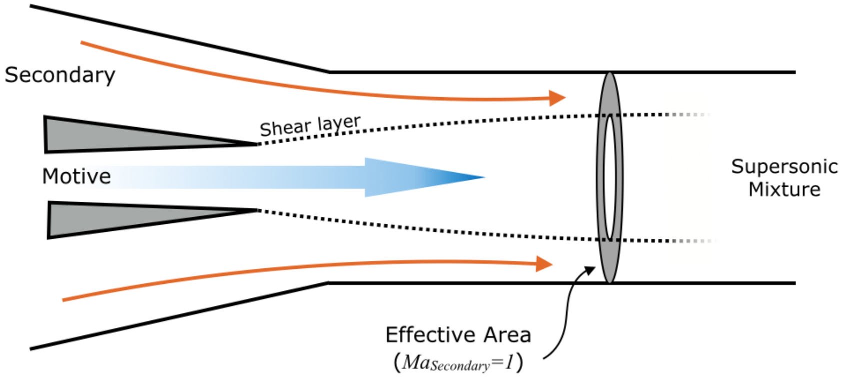

Figure 2.13 Schematics of the concept of the Effective Area as defined by Munday and Bagster [1977].

Among the first thermodynamic models is the work of Keenan [1950], which analytically solved the isentropic perfect gas relations for both constant pressure and constant area mixing. The perfect gas hypothesis was removed by Stoecker [1958], who employed tabulated real fluid properties and took losses into account by introducing isentropic efficiencies. These works assumed $p_{NXP} = p_b$, an assumption removed by Munday and Bagster [1977] who postulated that pressure equality occurs further down at the location of A_{eff}. After mixing, shocks in the CAS are usually considered as a single, normal shock occurring at the start of the diffuser [Sun, 1996]. Despite their simplicity, these models have a typical experimental deviation of 10% to 20%. In particular, the model of Huang *et al.* [1999] has been widely cited given its strong agreement with experimental ω_r data on single-phase ejectors with $R141b$. A thorough description of the evolution of ejector thermodynamic models up to 2009 can be found in the review of He *et al.* [2009].

In the last decade, efforts have switched towards extending the applicability of existing models and solve specific problems. Namely, the determination of single-choke performance has been attempted by Chen *et al.* [2013] and Galanis *et al.* [2014]. The latter authors apply the entropy generation principle to compute p_{lim} and introduce polytropic efficiencies which better adjust to pressure changes through the on-design to off-design transition. García del Valle *et al.* [2012] present a potential flow formulation and the use of real gas properties relationships for determining the entrainment ratio. Although of increased complexity, this model presents a difference of about 7% with the results of Huang *et al.* [1999]. For transcritical two-phase CO_2 ejectors, Banasiak and Hafner [2011] developed a differential $1D$ formulation of the Delayed Equilibrium Model, achieving a deviation of 1.84% (resp. 2.66%) in terms of critical primary flow rate (resp. P_{ratio}). In these type of flows, determining the choked conditions is particularly difficult since a correct speed of sound computation is still under debate. The problem is circumvented by maximizing the mass flow rate per unit area G which, for an isentropic expansion, can be expressed in terms of the inlet enthalpy (h_0), inlet entropy (s_0) and local pressure (p) as follows [Maytal, 2006]:

$$G\left(p, h_0, s_0\right) = \frac{\dot{m}}{A_t} = V\rho = \sqrt{2\left(h_0 - h\right)}\rho, \tag{2.11}$$

with the local enthalpy h and density ρ depending only on p and s_0. Equation (2.11) exhibits a maximum G^* at choking conditions. Thus, for fixed inlet conditions, the choked mass flow rate can be calculated by multiplying $G^* = max\left[G\left(p\right)\right]$ times the nozzle throat area. Since there is no need to determine the local speed of sound, the approach can be easily applied in two-phase flows, where critical conditions lie mostly over the saturation line [Maytal and Elias, 2009]. The model of Ameur *et al.* [2016] employs this approach to compute the thermodynamic properties of CO_2 ejectors for EERCs. A deviation of up to 7.14% (resp. 6.14%) is observed in the primary jet critical mass flow rate (resp. P_{ratio}). Note that in these cycles, ω_r is predetermined by the system through the quality at the condenser.

2.4.3 CFD Models

Computational Fluid Dynamics (CFD) is an area of fluid mechanics which relies on numerical methods to describe the full features of gas or liquid flows based on the *Navier-Stokes* (NS) equations. These techniques allow to study with outstanding detail a wide range of configurations and designs at a moderate cost compared to an equivalent experimental bench. This is particularly useful in configurations such as ejectors where, in addition, experimental characterization is limited by typically small prototypes, insulation jackets, hazardous materials and extreme operating conditions.

The computational cost of directly resolving the full spectra of time and space scales represented in the instantaneous NS equations for the compressible highly turbulent (and often two-phase) flow through an ejector is, at the moment, prohibitively high. The most preferred alternative approach consists in solving a statistically-averaged version of these equations known as the *Favre-Averaged Navier-Stokes* (FANS) or compressible *Reynolds-Averaged Navier Stokes* (RANS) equations. In the resulting system, the mean flow features are fully described but extra terms representing turbulent effects appear, requiring the need for turbulence models to close the system of equations and whose choice is very case dependent. In this regard, Bartosiewicz *et al.* [2005] assessed the accuracy of six two-equation turbulence models against experimental centerline pressure profiles on an air ejector. Experimental data were obtained using a capillary probe inserted through the primary nozzle (the technique greatly distorted the primary jet shock structure, showing the limitations of experimental methods for supersonic ejectors). Although none of the models provided entirely satisfactory agreement with the experimental data, the $k - \epsilon$ RNG and $k - \omega$ SST models showed the lower deviation in terms of shock phase, shock intensity and mean pressure recovery profiles, with the $k - \omega$ SST model standing out by its better mixing length predictions. Nonetheless, the correct prediction of internal flow features might not entirely correlate with accurately predicting global variables such as ω_r or P_{ratio}. Comparisons performed by Hemidi *et al.* [2009a] on an air ejector showed that the standard $k - \epsilon$ and $k - \omega$-SST models converge practically to the same on-design entrainment ratio value but with entirely different centerline pressure profiles. When including both on-design and off-design points, the standard $k - \epsilon$ deviation is less than 10% while for the $k - \omega$ SST model ranges from 10% to 20%. Differences in the prediction of internal flow features have been quantified by García del Valle *et al.* [2015], comparing the performance of four turbulence models in terms of ω_r and pressure measurements along the constant area section wall of a $R134a$ ejector. The $k - \epsilon$ model provided the best agreement with ω_r (deviation of $\sim 4.68\%$), but the $k - \omega$ SST model presented a better agreement with wall pressure measurements (deviation of $\sim 15.2\%$). A detailed description of the turbulence models often used in ejector modeling is provided in Chapter 3, Section 3.1.1.

The closure of the FANS system of equations also requires an equation of state relating pressure, temperature and density. To this end, the perfect or ideal gas model has been widely adopted given its simplicity and stability. In terms of accuracy, deviations in the range 1% to 10% versus experimental ω_r have been obtained for ejectors working with simple molecule gases such as N_2 [Zhu and Jiang, 2014b] and non-condensing water vapor [Ruangtrakoon *et al.*, 2013]. However, closer to the saturation line, the ideal gas assumption is no longer valid and a more complex model is needed. For condensing vapor ejectors, the wet steam model (which assumes homogeneous condensation and includes transport equations for droplet quantity and liquid fraction) shows better agreement with pressure data on convergent-divergent nozzles [Cai and He, 2013], predicting ω_r within 1% [Sharifi *et al.*, 2013]. In the case of slightly superheated refrigerants (without actual condensation), it is preferred to use the REFPROP equation database [NIST, 2010], which adopts fluid-specific formulations of the Helmholtz free energy equation of state adjusted with experimental data. Though this approach offers a deviation of the order of 0.1% for thermodynamic and transport properties of most common refrigerants, its application range might be limited for some gases. In these cases, a cubic equation of state such as the Peng-Robinson model can be used, which presents negligible differences when compared with ejector centerline profiles obtained with the REFPROP database, and has a deviation of less than 4% in terms of the inlet mass flows [Mazzelli and Milazzo, 2015].

For two-phase ejectors, such as in CO_2 EERCs, the simplest approach is the pseudo-fluid model (*i.e.*: Homogeneous Equilibrium Model) which treats the mixture as a single fluid with fraction-weighted average properties. This approach adds a transport equation for the phase distribution marker (*e.g.*: the volume fraction), which is used to determine the interfacial area and transfer terms [Attou and Seynhaeve, 1999]. Despite its simplicity, this model has been observed to agree better with experimental condensation data than the more complex Delayed Equilibrium Model [Banasiak and Hafner, 2013]. For transcritical CO_2 ejectors, Smolka *et al.* [2013] report differences of up to 14% and 20% for primary and secondary mass flow rates, respectively, using the pseudo-fluid and standard $k-\epsilon$ turbulence models. A similar study by Lucas *et al.* [2014] but with the $k-\omega$ SST model achieved an experimental deviation of up to 10% for the primary mass flow rate and pressure ratio for a CO_2 ejector without suction flow. For the tests with secondary flow, the pressure ratio deviation increased to 20%, although a good agreement is obtained with the experimental wall pressure values.

Table 2.1 lists some previous CFD studies of supersonic ejectors for different conditions. It can be seen that there is no real consensus yet over a CFD approach able to confidently represent the flow defining physics through the ejector. Though most studies focus on comparisons between different modelling choices rather than on the characterization of internal flow features, some interesting conclusions can be drawn from the literature. For example: Pianthong *et al.* [2007] and Sriveerakul *et al.* [2007] respectively captured the effective area reduction and the shortening of motive jet shock cells with increasing primary inlet pressure on steam ejectors. Little and Garimella [2016] studied the mixing section of a $R134a$ ejector, determining that the first shock angle relative to the horizontal direction is constant during on-design operation and that metastable effects at the exit of the motive nozzle can be ignored, which relaxes some constraints on condensation models for two-phase ejectors. Furthermore, other research groups have carried out in-depth analyses on the generation of losses across the ejector by incorporating a Second Law analysis: García del Valle *et al.* [2015] formulated an integral entropy transport equation on a supersonic $R134a$ ejector, identifying various entropy generating mechanisms and their contribution to total losses generation, while Lamberts *et al.* [2017b] adapted the definition of classical stream tubes to produce exergy tubes across an air ejector, showing that a greater exergy transfer occurs when operating close to p_{lim}, where irreversibilities due to viscous dissipation are lower in comparison with other operating points.

With the continuous progress in the capability of high performance computers, attempts are now being made at numerically modelling supersonic ejectors using more accurate and complex techniques such as the Large Eddy Simulation (LES) approach, where a filtered version of the Navier-Stokes equations is resolved, providing great detail of the large scale (geometry dependent) flow structures, while the smaller turbulent scales (of assumed universal behaviour) are modelled. Recently, Bouhanguel *et al.* [2015] performed a preliminary LES of a supersonic air ejector, although the high computational costs and difficulties for proper validation limited the study to a few visualizations without any validation or detailed analysis. It poses an exciting scenario for the future of numerical modelling of supersonic ejectors.

Table 2.1 Comparison of previous numerical studies. When not mentioned, the RANS models are used in their high-Reynolds number formulation using wall functions.

Authors	**Working fluid**	**Turb. Model**	**Exp. deviation**
Desevaux and Lanzetta [2004]	Air	Std. $k-\epsilon$	20% (P_{ratio})
Bartosiewicz *et al.* [2005]	Air	$k-\omega$ SST	$1\% - 23\%$ (p_{sec})
Pianthong *et al.* [2007]	Steam	Realizable $k-\epsilon$	5% (ω_r)
Sriveerakul *et al.* [2007]	Steam	Realizable $k-\epsilon$	$1\% - 12\%$ (ω_r)
Scott *et al.* [2008]	R245fa	Std. $k-\epsilon$	$5\% - 11\%$ (ω_r)
Hemidi *et al.* [2009a]	Air	Std. $k-\epsilon$	$1\% - 20\%$ (ω_r)
de Castro *et al.* [2010]	Air	$k-\omega$ SST	22% (ω_r)
Yazdani *et al.* [2012]	CO_2	$k-\omega$ SST	$1\% - 10\%$ (ω_r)
Ruangtrakoon *et al.* [2013]	Steam	$k-\omega$ SST	$5\% - 22\%$ (ω_r)
Cai and He [2013]	Steam	$k-\omega$ SST	15% (ω_r)
Banasiak *et al.* [2014]	$R744$	$k-\epsilon$ RNG	$1\% - 14\%$ (ω_r)
Zhu and Jiang [2014b]	N_2	$k-\epsilon$ RNG	$1\% - 10\%$ (ω_r)
Wang *et al.* [2014]	Steam	Realizable $k-\epsilon$	6% (ω_r)
Mazzelli and Milazzo [2015]	$R245fa$	$k-\omega$ SST	5% (ω_r)
García del Valle *et al.* [2015]	$R134a$	Std. $k-\epsilon$	14% (ω_r)
Little and Garimella [2016]	$R134a$	$k-\epsilon$ RNG	N/A
Lamberts *et al.* [2017b]	Air	$k-\omega$ SST (Low Reynolds)	1% (ω_r)

2.5 Droplet Injection in Ejectors

The previous sections show that general and internal flow features of ejectors have been extensively studied with both experimental and numerical approaches. Within the long-term goal of enhancing the performance of ejector systems, efforts focus now on specific issues. A point of discussion in this regard is the influence of droplets on the ejector performance parameters. Whether injected into the device or resulting from spontaneous condensation, droplets would affect the flow by altering its thermodynamic properties and extracting energy for breakup, acting in particular over two sources of losses: the velocity miss match at the mixing section [Al-Ansary and Jeter, 2004] and the intensity of shocks in the constant area section [Bilir Sag *et al.*, 2015]. Nonetheless, very few and inconclusive studies have been published on this matter.

2.5.1 Droplets in the Motive Nozzle

As steam flow is accelerated in *De Laval* nozzles, spontaneous condensation releases latent heat which is absorbed by the main flow [Yang *et al.*, 2010]. The local increase in gas temperature generates the small pressure bump, known as condensation shock, shown in Figure 2.14. Experimental studies show that spontaneous condensation reduces the overall Ma number along the nozzle diverging section but increases the entropy generation linked to droplet nucleation, an effect which can be reduced by injecting droplets mixed with the inlet flow [Teymourtash *et al.*, 2009].

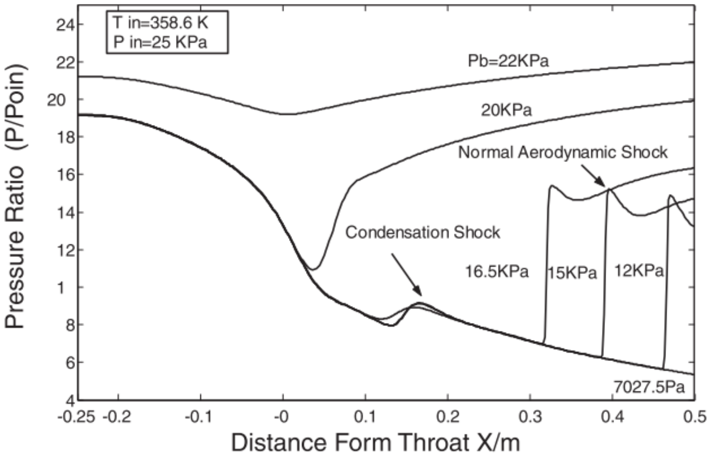

Figure 2.14 Pressure profiles in a converging-diverging nozzle with the existence of a condensation shock due to droplet formation, after Yang *et al.* [2010].

The premise of injecting droplets at the ejector primary inlet is to reduce the velocity mismatch at the mixing section by decelerating the motive flow while maintaining its momentum, reducing entropy generation and enhance mixing. However, experimental studies on air ejectors show that primary inlet air humidity only has noticeable effects at off-design conditions, where gains of 13% to 98% in secondary mass flow rate have been registered for varying primary inlet water mass fraction (4.3% and 11.2%) and primary pressure (107 kPa to 446 kPa) [Al-Ansary and Jeter, 2004]. Further studies using combined numerical and experimental approaches have observed a similar behaviour with injected liquid mass fractions as low as 1% [Hemidi *et al.*, 2009a], along with an increase of about 5% in limiting pressure and of 115% in the secondary mass flow rate close to malfunction operation. Nonetheless, these results should be taken with caution since in both cases the used fluid pair is uncommon for refrigeration purposes and the ejector was studied as a sole unit. In fact, a study by Little and Garimella [2016] on a $R134a$ HDRC system shows a linear decrease of entrainment ratio as the primary inlet superheat ($T_{prim} - T_{prim}^{Sat}$) goes to zero. Shadowgraph images of the mixing section show that the area occupied by the motive jet increases as condensation augments. Despite the integration within a complete refrigeration cycle, no data was reported concerning system performance or p_{lim}.

2.5.2 Shock-droplet Interactions in the Constant Area Section

Mist of droplets have been successfully applied to control the propagation and intensity of explosions [Igra *et al.*, 2013]. The same phenomenon could reduce the shock intensity in the CAS of ejectors, a region which accounts for about 40% of the exergy destroyed through the device [Bilir Sag *et al.*, 2015; Khennich *et al.*, 2014].

At the encounter with a shock wave front, droplets absorb energy for deformation and breakup, reducing the main gas velocity and pressure jump. The breakup mode varies from simple division to explosive disintegration depending on droplet stability. The process can be characterized using the droplet-gas mixture *Weber* (We) and *Reynolds* (Re) numbers based on the droplet diameter:

$$We = \frac{\rho_g^* W_S^2 \phi_d}{\sigma_d} \tag{2.12}$$

$$Re = \frac{\rho_g^* W_S \phi_d}{\mu_g} \tag{2.13}$$

These dimensionless numbers depend on the gas density (ρ_g^*) and velocity at the shock front (W_S), droplet diameter (ϕ_d), gas viscosity (μ_g) and surface tension (σ_d). For droplets, Jourdan *et al.* [2010] propose the breakup regime classification shown in Table 2.2 with

We and Re as principal parameters, such that increasing droplet diameter and relative velocity lead to more violent breakups.

Table 2.2 Droplet breakup regimes depending on We and Re numbers, after Jourdan *et al.* [2010].

Regime	We	$We/\sqrt{Re}$	**Break-up characteristics**
I	10-40	0.2 - 1	Division into two smaller droplets
II	40-1000	1 - 20	Striping of surface layer, apparition of smaller droplets
III	1000-100000	20 - 100	Explosive break-up into much smaller droplets

Note that at lower We values, no break-up should be expected. On this regard, Pilch and Erdman [1987] proposed the following correlation to determine this critical Weber threshold (We_c) based on experimental observations:

$$We_c = 12\left(1 + 1.077 Oh^{1.6}\right) \tag{2.14}$$

where Oh is the *Ohnesorge* number, which relates viscous to surface tension forces in a fluid particle [Chauvin *et al.*, 2011]:

$$Oh = \frac{\sqrt{We}}{Re}, \tag{2.15}$$

for droplets, it is generally assumed that $Oh \sim 0.1$.

By performing experiments on an air-water shock-tube at various droplet diameters and shock speeds in the range such that $14 < We < 2470$ and $690 < Re < 19800$, Jourdan *et al.* [2010] found a relationship between shock attenuation and the factor $fac_{Jourdan} = \frac{We}{\sqrt{Re}}\frac{S_e}{a^2}$, where S_e and a are the specific droplet surface and tube cross sectional area respectively. For $Ma \sim 1.8$ and an initial droplet diameter of 500 µm, an attenuation of 90% (resp. 20%) in pressure jump (resp. shock speed) was observed.

A similar setup was used by Chauvin *et al.* [2011] for droplet breakup visualization in the range $40 < We < 1000$, fixing initial droplet diameter and volume fraction to 500 µm and 1.2%. It was observed that, prior to breakup, droplets deformed increasing the surface exchange area and enhancing its attenuation effects in comparison with solid particles. The physical time for deformation and breakup was determined to be of the order of 200 µs. Furthermore, pressure profiles along the droplet mist region were captured in greater detail as shown in Figure 2.15 for $fac_{Jourdan} < 50$, revealing a pressure increase of about 20% at the shock front due to wave reflections and initial deceleration.

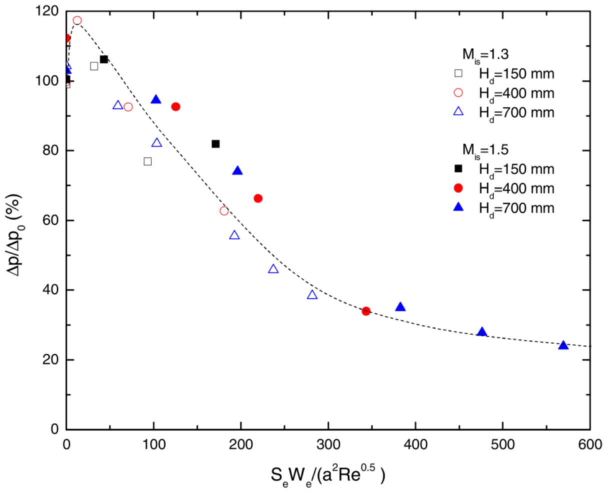

Figure 2.15 Attenuation of pressure jump (ΔP) of a normal shock wave as it passes through a cloud of droplets. After Chauvin *et al.* [2011].

Breakup Energy

The energy absorbed from the gas for droplet breakup can be determined using the droplet breakup energy, ΔE_{br}, which is related to the changes in surface energy E_s. For one spherical droplet of diameter ϕ_d and surface tension σ, E_s is defined as [Adiga *et al.*, 2009]:

$$E_s = S_d \sigma = \pi \sigma \phi_d^2 \tag{2.16}$$

During breakup, E_s varies along the transition shown in Figure 2.16 such that the energy absorbed from the gas by a mother droplet of diameter ϕ_1 breaking into n_3 daughters of diameter ϕ_3 is:

$$\Delta E_{br} = \pi \sigma \left(n_3 \phi_3^2 - \phi_1^2 \right) = \pi \sigma \phi_1^2 \left(\frac{\phi_1}{\phi_3} - 1 \right) \tag{2.17}$$

where mass conservation has been applied to eliminate n_3. Note that $\Delta E_{br} > 0$ is ensured by the fact that $\phi_3 < \phi_1$, showing the endothermic nature of the process. The daughter droplet diameter can be determined using the critical Weber number (Equation 2.14), thus:

$$\phi_3 = \frac{\sigma We_c}{\rho_g W_s^2} \tag{2.18}$$

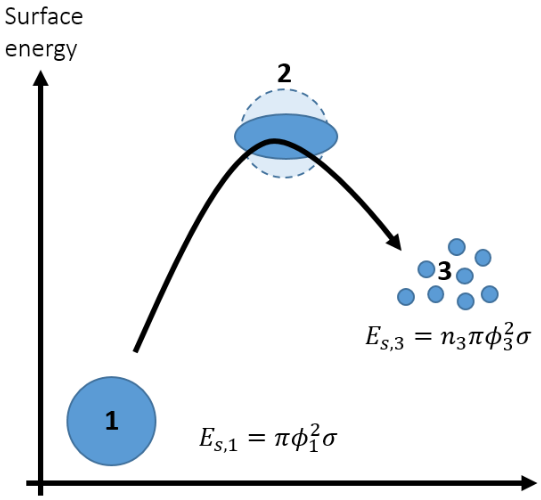

Figure 2.16 Droplet surface energy variation during breakup.

2.6 Conclusions

Supersonic ejectors are simple devices offering a reliable way to compress a flow with reduced costs and environmental impact, which have gained interest in recent years for their application in better performing alternative refrigeration cycles. During the last decades, their general behaviour for various configurations and operating conditions has been thoroughly studied, although with some reserves: experimental studies are mostly limited to global operation parameters and there is yet no consensus on a proper RANS approach to confidently characterize its internal flow features.

Furthermore, at a point where the global ejector features are widely known and with the long term objective of enhancing the competitiveness of ejector based refrigeration systems, the attention switches now to specific manners to improve its efficiency. In particular, the presence of droplets for enhancing ejector performance, by improving energy transfer through the mixing layer and reducing shock-wave intensity, has been scarcely discussed in the literature and with somewhat inconclusive results.

PART II

METHODS

CHAPTER 3

Numerical Modelling of Supersonic Ejectors

This chapter describes the principles and methods adopted in the construction of the numerical CFD models of single-phase supersonic ejectors used in this investigation. The chapter starts with the presentation of the basic flow governing equations together with the most important simplifications and necessary closure relationships. Afterwards, the strategies and the numerical set up adopted in the solution of this system is described. Finally, a benchmark study comprising five two-equation turbulence models and three gas properties models was carried out, highlighting the choice offering the best compromise in terms of accuracy versus computational cost.

3.1 Governing Equations

The compressible turbulent flow through a supersonic ejector is described by the *Navier-Stokes* (*NS*) equations, which reflect mass, momentum and energy conservation across a fluid volume. At the moment, the direct solution of these equations for most problems of practical interest is too computationally expensive. An alternative is to solve the *Favre-Averaged Navier-Stokes* (*FANS*) or compressible *Reynolds-Averaged Navier-Stokes* (*RANS*) equations which describe the mean flow features. In absence of body forces, these can be written in the following form [Lamberts *et al.*, 2017b; Wilcox *et al.*, 1998]:

$$\frac{\partial \bar{\rho}}{\partial t} + \frac{\partial}{\partial x_i}\left(\bar{\rho}\tilde{u}_i\right) = 0 \tag{3.1a}$$

$$\frac{\partial}{\partial t}\left(\bar{\rho}\tilde{u}_i\right) + \frac{\partial}{\partial x_j}\left(\bar{\rho}\tilde{u}_j\tilde{u}_i\right) = -\frac{\partial p}{\partial x_i} + \frac{\partial}{\partial x_j}\left(\bar{\tau}_{ij} - \overline{\rho u_i'' u_j''}\right) \tag{3.1b}$$

$$\frac{\partial}{\partial t}\left(\bar{\rho}\tilde{e}^t\right) + \frac{\partial}{\partial x_j}\left(\bar{\rho}\tilde{u}_j\tilde{h}^t\right) = \frac{\partial}{\partial x_j}\left[-q_j - \overline{\rho u_j'' h''} + \tilde{u}_i\left(\bar{\tau}_{ij} - \overline{\rho u_i'' u_j''}\right) + \overline{\tau_{ji} u_i''} - \overline{\rho u_j'' \tfrac{1}{2} u_i'' u_i''}\right] \tag{3.1c}$$

Two averaging processes are introduced in System (3.1), a conventional time average (*i.e.*: Reynolds average):

$$\bar{b} = \frac{1}{t_f} \int_{t_o - \frac{t_f}{2}}^{t_o + \frac{t_f}{2}} b dt, \tag{3.2}$$

and a density-weighted time average (*i.e.*: Favre average):

$$\tilde{b} = \frac{1}{\bar{\rho}} \frac{1}{t_f} \int_{t_o - \frac{t_f}{2}}^{t_o + \frac{t_f}{2}} \rho b dt. \tag{3.3}$$

In this manner, any given quantity b can be expressed as the sum of mean plus fluctuating components: $b = \bar{b} + b'$ in the case of *Reynolds* averaging and $b = \tilde{b} + b''$ in the case of *Favre* averaging. The quantities $\tilde{e}^t$ and $\tilde{h}^t$ in Equation (3.1c) are, respectively, the total internal energy and total enthalpy, including the mean and turbulence kinetic energies:

$$\tilde{e}^t = \tilde{e} + \frac{\tilde{u}_i \tilde{u}_i}{2} + \frac{u_i'' u_i''}{2}, \tag{3.4}$$

$$\tilde{h}^t = \tilde{h} + \frac{\tilde{u}_i \tilde{u}_i}{2} + \frac{u_i'' u_i''}{2}, \tag{3.5}$$

$\bar{\tau}_{ij}$ is the viscous shear stress tensor which for a Newtonian fluid is written as:

$$\bar{\tau}_{ij} = \mu \left[\left(\frac{\partial \tilde{u}_j}{\partial x_i} + \frac{\partial \tilde{u}_i}{\partial x_j} \right) - \frac{2}{3} \frac{\partial \tilde{u}_k}{\partial x_k} \delta_{ij} \right] \tag{3.6}$$

A result of the averaging process is the appearance of additional terms involving the fluctuating components ($e.g.$:u_i''), which require further modelling. Firstly, the last term in the right-hand side of the momentum conservation equation (Eq.3.1b), known as the Favre-Averaged Reynolds-Stress tensor, is related to the mean velocity gradients using the Boussinesq hypothesis:

$$-\overline{\rho u_i'' u_j''} = \tau_{ij,t} = \mu_t \left[\left(\frac{\partial \tilde{u}_j}{\partial x_i} + \frac{\partial \tilde{u}_i}{\partial x_j} \right) - \frac{2}{3} \frac{\partial \tilde{u}_k}{\partial x_k} \delta_{ij} \right] - \frac{2}{3} \bar{\rho} k \delta_{ij}, \tag{3.7}$$

where k and μ_t are respectively the turbulence kinetic energy and the turbulent or eddy viscosity, which are determined using the turbulence models described in Section 3.1.1. The last term in the R.H.S. of Eq 3.7 is often neglected.

The first two terms in the right-hand side of the energy conservation equation (Eq.3.1c), respectively the molecular diffusion heat flux and the turbulent heat flux, are approximated in terms of the mean temperature gradient as [Wilcox *et al.*, 1998]:

$$q_j + \overline{\rho u_j'' h''} = q_j + q_{j,t} = \lambda \frac{\partial \tilde{T}}{\partial x_j} + \frac{c_p}{Pr_t} \mu_t \frac{\partial \tilde{T}}{\partial x_j} = \lambda_{eff} \frac{\partial \tilde{T}}{\partial x_j} \tag{3.8}$$

where λ is the thermal conductivity, c_p is the constant pressure specific heat and Pr_t is the turbulent Prandtl number, which is often assumed to be 0.85. The last two terms on the right-hand side of Eq.(3.1c) are neglected.

System (3.1) has eight unknowns: ρ, $\vec{U} = [u, v, w]$, p, $\tilde{T}$, k and μ_t but only five equations. The turbulence model introduces two additional relations, often in the form of transport equations for turbulent quantities (*e.g.*: the turbulence kinetic energy k, the dissipation rate of the turbulence kinetic energy ϵ or the specific dissipation rate ω). The remaining expression is an equation of state of the form $\rho = \rho(p, \tilde{T})$ stemming from the assumed gas model. Although the perfect gas assumption is usually adopted, other more accurate choices also exist.

3.1.1 Turbulence Models

All the assessed turbulence models considered here belong to the family of two-equation models, in which the turbulent viscosity μ_t is computed by combining the turbulence kinetic energy k with either the turbulent dissipation rate ϵ or the eddy frequency ω. These models are reasonably accurate for free and fully developed turbulent flows, but are known for being too dissipative, hindering its performance in wall-bounded flows and configurations with important rotational character, separation or anisotropy.

Within the context of supersonic ejectors, the $k-\epsilon$ models are widely used given its stability and better entrainment ratio accuracy [Hemidi *et al.*, 2009a; Li and Li, 2011], although some studies suggest that the $k-\omega$ SST model is more accurate, in particular concerning internal flow structure [Bartosiewicz *et al.*, 2005; Ruangtrakoon *et al.*, 2013].

Standard $k-\epsilon$ model

In the standard $k-\epsilon$ model, the turbulent viscosity is a function of k and ϵ:

$$\mu_t = \rho C_\mu \frac{k^2}{\epsilon} \tag{3.9}$$

where $C_\mu \sim 0.09$ is an empirical constant. Two transport equations for k and ϵ are required, respectively [Wilcox *et al.*, 1998]:

$$\frac{\partial}{\partial t}(\bar{\rho}k) + \frac{\partial}{\partial x_i}(\bar{\rho}ku_i) = \frac{\partial}{\partial x_j}\left[\left(\mu + \frac{\mu_t}{\sigma_k}\right)\frac{\partial k}{\partial x_j}\right] + \mathcal{P} - \bar{\rho}\epsilon - Y_M \tag{3.10a}$$

$$\frac{\partial}{\partial t}(\bar{\rho}\epsilon) + \frac{\partial}{\partial x_i}(\bar{\rho}\epsilon u_i) = \frac{\partial}{\partial x_j}\left[\left(\mu + \frac{\mu_t}{\sigma_\epsilon}\right)\frac{\partial \epsilon}{\partial x_j}\right] + C_{1\epsilon}\frac{\epsilon}{k}\mathcal{P} - C_{2\epsilon}\bar{\rho}\frac{\epsilon^2}{k} \tag{3.10b}$$

where $C_{1\epsilon} = 1.44$ and $C_{2\epsilon} = 1.92$ are empirical constants and $\sigma_k = 1.0$ and $\sigma_\epsilon = 1.3$ are respectively the turbulent Prandtl numbers for k and ϵ. The turbulent production term $\mathcal{P}$ represents the generation rate of k from the mean flow fluctuations. It is modelled as a function of μ_t and the strain rate tensor (S_{ij}):

$$\mathcal{P} = -\bar{\rho}\overline{u_i'u_j'}\frac{\partial u_j}{\partial x_i} = \mu_t 2\left(S_{ij}S_{ij}\right). \tag{3.11}$$

Y_m accounts for the dilation-dissipation effects of compressibility, it is modelled as a function of the turbulent Mach number $Ma_t = \sqrt{\frac{k}{a^2}}$:

$$Y_m = 2\bar{\rho}\epsilon Ma_t^2 \tag{3.12}$$

The standard $k-\epsilon$ model has been the industry favourite for decades, given its robustness and economy.

$k-\epsilon$ RNG model

While the transport equation for ϵ in the standard model stems from a purely empirical analysis, in the $k-\epsilon$ RNG model a statistical technique called Renormalization Group Method is used to derive a transport equation for ϵ from the Navier-Stokes equations. This also results in a differential equation for μ_t, which tends to Eq. (3.9) in the limit of high Re numbers. This improved model corrects failing aspects of the standard version: prediction of round jet spreading rates and near-wall flows [Yakhot and Orszag, 1986].

$k-\epsilon$ Realizable model

In this case, the ϵ equation is derived from the exact transport equation of mean-square vorticity fluctuations and the turbulent viscosity is calculated using Eq. (3.9), but with C_μ being now a function of the mean strain-rate and rotation tensors. This model is considered more physically consistent than the standard and RNG models, and outperforms them particularly in separated flows and where important secondary flows are present [Shih *et al.*, 1995].

Standard $k-\omega$ SST model

In the $k-\omega$ SST model, a transport equation for the specific dissipation rate ($\omega = \epsilon/k$) substitutes Eq. (3.10)b):

$$\frac{\partial}{\partial t}\left(\bar{\rho}\omega\right) + \frac{\partial}{\partial x_i}\left(\bar{\rho}\omega u_i\right) = \frac{\partial}{\partial x_j}\left[\left(\mu + \frac{\mu_t}{\sigma_\omega}\right)\frac{\partial \omega}{\partial x_j}\right] + \mathcal{P}_\omega - \mathcal{D}_\omega + \mathcal{X}_w \tag{3.13}$$

where σ_ω is the turbulent Prandtl for ω, and $\mathcal{P}_\omega$, $\mathcal{D}_\omega$ and $\mathcal{X}_\omega$ are respectively the production, dissipation and cross-diffusion terms. In its pure form, the $k-\omega$ model is superior in the computation of the near-wall viscous region, but has severe problems in free stream configurations [Pope, 2009]. Menter [1994] proposed an improved alternative, the $k-\omega$ Shear Stress Transport model ($k-\omega$ SST), where the turbulent viscosity (and most parameters like $\mathcal{P}_\omega$, $\mathcal{D}_\omega$ and $\mathcal{X}_\omega$) are calculated using blending functions depending on the normal distance to the wall, such that the $k-\omega$ model is applied in the boundary layer region and the standard $k-\epsilon$ model is applied away from walls. This approach offers better accuracy when dealing with complex features such as adverse pressure gradients and transonic shock-waves.

The near-wall accuracy of the $k-\omega$ SST model can be enhanced with a low-Reynolds number correction, which adds damping terms to the k and ω transport equations, thus modifying the laminar-turbulent transition and reproducing the k profiles observed very close to walls. Both the *high-* and *low-Reynolds* number formulations were assessed in this investigation.

Near wall treatment

Under the high-Reynolds number approach, the boundary layer region is not fully resolved but approximated using semi-empirical wall functions for the inner momentum and thermal boundary layers. The use of standard wall functions allows to relax the mesh refinement constraint, such that the wall coordinate y^+ lies between 25 and 30 for computations using the high-Reynolds number approach. For the low-Reynolds number formulation, the boundary layer is resolved up to the viscous sublayer, requiring near wall refining up to $y^+ = 1$ through the whole computational domain. Of course, such an approach is more computationally expensive.

3.1.2 Gas Properties

Three approaches were considered for the evaluation of gas properties: the perfect gas model, the Redlich-Kwong-Soave Equation of State (RKS-EoS) and the *NIST-REFPROP* 7.0 equation database.

Perfect Gas Model

The perfect gas model is the simplest approach. It assumes that gas molecules are punctual particles without any significant interactions or individual volume. It is based on the ideal gas law:

$$\frac{p}{\rho} = RT, \tag{3.14}$$

where R is the gas constant, resulting from dividing the universal gas constant ($R_u = 8.3145\,\mathrm{J/mol/K}$) by the gas molar mass (M). In the perfect gas model all transport properties are constant and the specific enthalpy (h) and specific internal energy (e) are functions of the temperature only:

$$e = c_v T \qquad h = c_p T \tag{3.15}$$

where c_v and c_p are respectively the isochoric and isobaric specific heats. This approach is widely used in thermodynamic models of single-phase ejectors given its simplicity and stability [Galanis and Sorin, 2016; Huang *et al.*, 1999]. It also shows good agreement in compressible RANS simulations of ejectors working with simple gases [Zhu and Jiang, 2014b] and non-condensing steam [Ruangtrakoon *et al.*, 2013].

Redlich-Kwong-Soave Equation of State

This model uses a pressure explicit cubic equation of state, similar to the ideal gas law with added terms to account for molecular interactions:

$$P = \frac{R\,T}{v-b} - \frac{a(T)}{v(v+b)} \tag{3.16a}$$

$$a(T) = 0.42748\frac{R^2\,T_c^2}{P_c}\alpha(T) \tag{3.16b}$$

$$b = 0.08664\frac{R\,T_c}{P_c} \tag{3.16c}$$

$$\alpha(T) = \left[1 + (0.480 + 1.574f - 0.176f^2)\left(1 - \left(\frac{T}{T_c}\right)^{1/2}\right)\right]^2 \tag{3.16d}$$

where P_c and T_c are respectively the pressure and temperature at the critical point, f is the acentric factor. Transport properties are assumed constant. This model is well known for its simplicity and improved accuracy over the perfect gas model in the region close to the saturation dome and above the critical point [Camporese *et al.*, 1985]. Nonetheless, to the best of the author's knowledge there are no references on its application in gas ejectors.

NIST-REFPROP 7.0 equation database

The REFPROP 7.0 model for $R134a$ is based on the formulation of Tillner-Roth and Baehr [1994], where a Helmholtz free energy equation of state is used to determine all fluid properties, including transport quantities. This 21 parameters equation has been adjusted to an extensive quantity of experimental measurements for $R134a$. It accurately represents real gas behaviour in the temperature range −103 °C to 182 °C for pressures up to 70 MPa, at an added computational cost, given the need to solve the subroutines for each cell in the domain at each time step. The REFPROP libraries are commonly used for numerical studies of single-phase supersonic ejectors with refrigerants such as $R142b$ [Bartosiewicz *et al.*, 2006], CO_2 [Banasiak *et al.*, 2012] or $R245fa$ [Mazzelli and Milazzo, 2015].

3.2 Particle injection

Droplets injected into the ejector are modelled using a discrete phase Langrangian approach, based on following the trajectory and temperature of a given number of particles from the injection point to their end (breakup or leaving the domain). Within this work, droplets are assumed as spherical particles, able to exchange momentum and sensible heat with the main flow. While breakup effects are considered, coalescence and phase-change effects are neglected.

The discrete phase motion is computed by integrating a force balance around each particle:

$$\frac{du_{p,i}}{dt} = F_D \left(\tilde{u}_i - u_{p,i} \right), \tag{3.17}$$

where $u_{p,i}$ is the particle velocity vector and R.H.S. term represents the drag force per unit particle mass. For spherical particles of diameter d_p and density ρ_p:

$$F_D = \frac{18\mu}{\rho_p d_p^2} \frac{C_D Re_p}{24}, \tag{3.18}$$

with Re_p being the relative Reynolds number between the particle and the continuous phase:

$$Re_p = \frac{\bar{\rho} d_p \mid u_{p,i} - \tilde{u}_i \mid}{\mu}, \tag{3.19}$$

and the drag coefficient C_D takes the form shown in Eq. (3.20), as a function of the empirical constants $a1$, $a2$ and $a3$ which are dependent on Re_p[Morsi and Alexander, 1972]:

$$C_D = a1 + \frac{a2}{Re_p} + \frac{a3}{Re_p^2}, \tag{3.20}$$

For $Ma > 0.4$, C_D is corrected following the guidelines of Clift *et al.* [2005].

In parallel to a particle's trajectory, its temperature is computed by applying a heat balance comprising convective heat transfer at its surface:

$$m_p cp_p \frac{dT_p}{dt} = h_p A_p \left(\bar{T}_\infty - T_p \right) \tag{3.21}$$

where m_p, cp_p A_p and T_p are respectively the particle's mass, isobaric specific heat, surface area and temperature. $\bar{T}_\infty$ is the local temperature of the continuous phase and h_p is the convection heat transfer coefficient, determined as a function of the local Nusselt number (Nu) using the correlation of Ranz *et al.* [1952]:

$$Nu = \frac{h_p d_p}{\lambda} = 2.0 + 0.6 Re_p^{1/2} Pr^{1/3}. \tag{3.22}$$

The WAVE model for droplet breakup

Breakup is modelled using the WAVE approach proposed by Reitz *et al.* [1987] for flow configurations with $We \geq 100$. The model assumes that breakup parameters such as the breakup time and daughter droplet size are related to the waves of fastest grow generated on the surface of the mother droplets. The equation for wave growth rate (Ω) is derived from the stability analysis of the waves generated on the surface of a cylindrical, viscous, liquid jet, solved by assuming wave solutions of the hydrodynamic equations. The newly formed droplets have an initial radius r_d:

$$r_d = B_o \Lambda \tag{3.23}$$

where $B_o = 0.61$ is an empirical constant and Λ is the wavelength of the fastest-growing waves. Moreover, the rate of change of the mother droplet radius, r_m, is:

$$\frac{dr_m}{dt} = -\frac{r_m - r_d}{\tau_d}, \tag{3.24}$$

with the breakup time, τ_d, defined as:

$$\tau_d = \frac{3.762 B_1 r_m}{\Lambda \Omega_{max}}, \tag{3.25}$$

where $B_1 = 1.73$ is an empirical constant and Ω_{max} is the maximum wave growth rate. Both Ω_{max} and the corresponding Λ are functions of the flow Weber, Taylor and Ohnesorge numbers, resulting from curve-fits of numerical solutions of the the wave growth equation [Reitz *et al.*, 1987].

For the implementation of the WAVE model, the rate given by Eq. (3.25) is used to estimate mass accumulation from the mother droplet. Once this shed mass is equal to 5%, a new daughter droplet is generated with the radius given by Eq. (3.23). This new droplet has the same properties (position, pressure, temperature, etc.) as the mother droplet.

Momentum and heat exchange with the continuous gas

Two-way coupling exists between the continuous and discrete phases, such that the carrier gas affects the particle's properties (temperature, velocity, pressure) and vice-versa. The momentum and heat exchanges are determined by computing the momentum and thermal energy changes of each particle as it enters and leaves a computational cell. These variations are then added as source terms to the continuous phase momentum and energy equations. The momentum change of a particle, M_{ch}, is calculated as:

$$M_{ch} = \frac{18\mu C_D Re_p}{\rho_p d_p^2 24}(u_{p,i} - \tilde{u}_i)\dot{m}_p \Delta t \tag{3.26}$$

where $\dot{m}_p$ is the mass flow rate of the particles through the cell, and Δt is the numerical time-step used for integrating the particle's equations of motion and temperature [Eqs. (3.17) and (3.21)]. Similarly, the particle's thermal energy change, Q_{ch}, is:

$$Q_{ch} = \frac{\dot{m}_{p,0}}{m_{p,0}}\left(-m_{p,out} Cp_p T_{p,out} + m_{p,in} Cp_p T_{p,in}\right), \tag{3.27}$$

where $\dot{m}_{p,0}$ and $m_{p,0}$ are the particle's initial injection mass flow rate and initial mass respectively, and the subscripts *in* and *out* refer to the states at the cell entry and exit.

3.3 Flow Solver

The flow governing equations (Eqs. (3.1)) were solved using the commercial software ANSYS Fluent v.15 based on the finite volume method. In this method, the compressible RANS equations, along with the gas properties and turbulence model, are applied to small subdivisions or volumes conforming the computational domain, requiring numerical approximations to evaluate the terms involving derivatives and boundary fluxes. After discretization, the resulting system of algebraic equations may be solved using either a density or pressure based algorithm. Although from a historical perspective, density-based solvers are usually preferred for supersonic flows involving abrupt gradients (*e.g.*: shock waves), pressure-based solvers based on the *SIMPLE* algorithm have been successfully used in both single- [Yazdani *et al.*, 2012; Zhu and Jiang, 2014b] and two-phase [Li and Li, 2011] supersonic ejector computations. Both approaches were used in this investigation. In the following, the specific set up of the cases covered in this thesis will be described. In-depth information on the finite volume method can be found in the books of Versteeg and Malalasekera [2007] and Ferziger and Peric [2002].

For all calculations involving $R134a$, advective fluxes were discretized using a second-order upwind scheme, except for the pressure equation where the PRESTO! scheme (specifically designed for flows involving steep pressure gradients) has been preferred, diffusive terms were discretized using second-order central differences schemes and gradients were evaluated using the least-squared method. The *Coupled* pressure-based algorithm, with full pressure-velocity coupling, was chosen. The full implicit coupling is achieved through an implicit discretization of pressure gradient terms in the momentum equations and face mass fluxes, including the Rhie-Chow pressure dissipation terms [ANSYS, 2013]. The energy equation is solved in a second step and density is computed through the gas property model. For this particular application, convergence with the *Coupled* algorithm appeared to be much more stable than with any of the density-based alternatives, and results from both cases were indistinguishable. A high-order relaxation technique was applied throughout the entire computation to ensure convergence smoothness.

For the air supersonic ejector computations, advective and diffusive terms were discretized using respectively second-order upwind and central differences schemes while gradients were evaluated using the least-square method. The resulting system was solved using an implicit density-based solver, where a coupled set of equations for density, velocity and temperature is solved simultaneously at each time step, while pressure is obtained through the equation of state.

The equations describing the trajectory and temperature of the discrete phase form a system of ordinary differential equations in time, which was integrated using a semi-implicit trapezoidal method. A point injection approach was used to fix the initial conditions for the injected droplets: velocity, temperature and average diameter. The discrete phase trajectories and temperatures were updated every 10 main-flow iterations.

3.4 Numerical Setup

In general, the ejector flow domain was assumed to be steady state and axi-symmetric. Previous studies show that the flow through the device is predominantly two-dimensional [Pianthong *et al.*, 2007]. It must be noted however that Mazzelli and Milazzo [2015] report a better accuracy of the off-design conditions predictions in squared-section ejectors when using a 3D computational domain.

Ejector walls were modelled as adiabatic and hydro-dynamically smooth walls. Although some studies report that imposing a low wall roughness might improve accuracy [Mazzelli and Milazzo, 2015], a preliminary analysis showed that, for the particular cases considered in this thesis, including even a very low wall roughness value resulted in important deviations from experimental entrainment ratio data (which does not provide any information on this regard). Total pressure and total temperature were prescribed as inlet boundary conditions, whereas static pressure was fixed at the outlet. For the cases where the operating conditions are based on experimental data, it is assumed that the inlet and outlet velocities are negligible relative to the mean values through the geometry, therefore the reported experimental data was taken as corresponding total pressure and total temperature values. Inlet turbulence boundary conditions were set by prescribing a 5% turbulence intensity and the boundary hydraulic diameter. A preliminary sensitivity analysis showed no verifiable influence of these parameters on the final results.

Given the different near-wall refinement requirements of the low- and high-Reynolds number approaches, two different mesh strategies were used. For the high-Reynolds number computations, unstructured meshes with five prismatic layers of near-wall refinement were employed. Grid size was determined following a mesh-independence study based on the variations in entrainment ratio and pressure and Mach number profiles along the ejector centreline. For the low-Reynolds number cases, structured meshes conformed by tetrahedral elements were used, with 21 wall adjacent prismatic layers and size refining in the shear layer region to better capture the increased activity in this region. Given the smaller average element size in this case, no grid independence study was deemed necessary. An average dimensionless wall coordinate value of 1 was sought to ensure the computation of the linear and logarithmic regions. In these cases, mesh refinement. Examples of the grid configurations for low- and high-Reynolds number computations are shown in Figure 3.1.

The flow field was initialized using a hybrid-initialization method, where a Laplace equation for pressure and velocity is resolved at first to obtain a physically coherent initial condition. Nonetheless, it was observed that attempts at directly using the second-order schemes rapidly diverged. Therefore, a progressive approach was adopted: for the high-Reynolds number cases, a first-order solution using the Standard $k-\epsilon$ and Perfect Gas models was obtained from the hybrid-initialization method. The first-order solution was then used as initial condition for the computation with any of other high-Reynolds number turbulence models, which was then used as starting point for the second-order cases. In the case of the low-Reynolds number approach, a first-order solution with the high-Reynolds number $k-\omega$ - SST model was interpolated onto the finer mesh. For all cases, the RKS and $REFPROP$ solutions were started from a corresponding first-order solution using the perfect gas model. Convergence was achieved when the following criteria were met:

— residuals for all conservation equations were under 10^{-4},

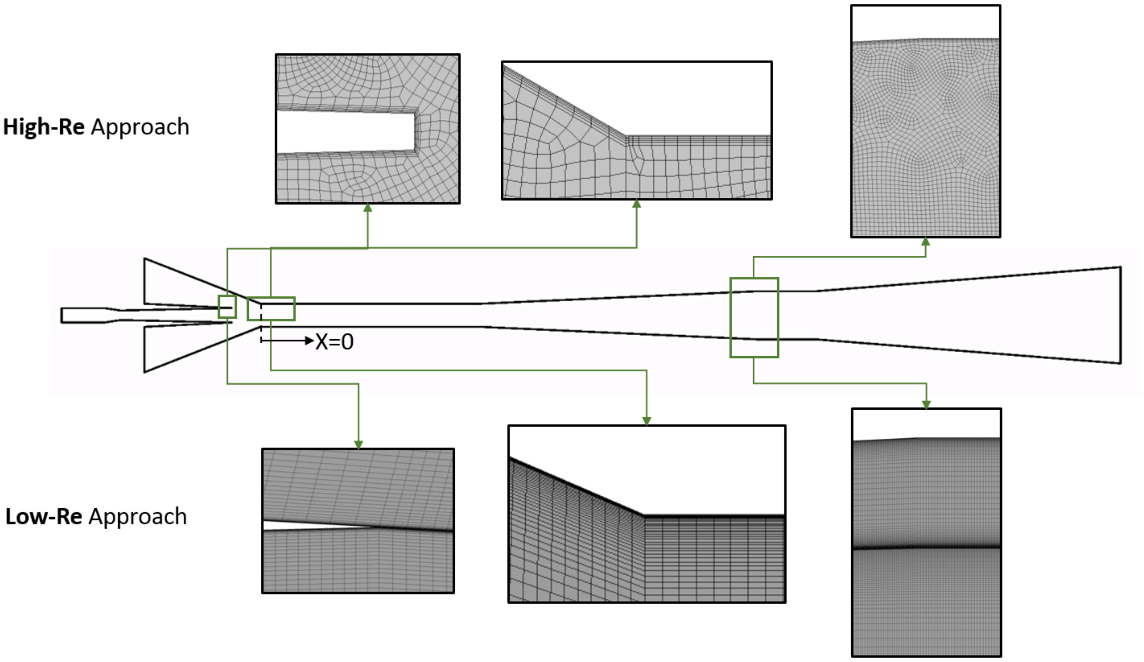

Figure 3.1 Examples of the mesh grids used for the high- and low-Reynolds number turbulence models.

— mass imbalances under 1% of the primary inlet mass flow rate,
— stable area-weighted average outlet temperatures.

All computations were performed on a workstation with 16GB of RAM and a four core $i7-7440$ CPU (3.40GHz), taking between 1 and 6 hours to complete, depending on the chosen turbulence and gas properties models.

3.5 Validation and Benchmark Study

A numerical benchmark covering the turbulence and gas properties models described in Sections 3.1.1 and 3.1.2 was carried out, based on the experimental information of García del Valle *et al.* [2014] which assesses the performance of different $R134a$ single-phase supersonic ejector prototypes for application in a HDRC, with varying mixing section profiles and primary nozzle exit positions. This study was chosen given the fact that it offers a particularly high level of detail regarding the ejector geometry and covers a realistic range of operating conditions for refrigeration purposes.

3.5.1 Baseline Geometry and Working Conditions

Ejector prototype 'A' from the study of García del Valle *et al.* [2014] was used in this benchmark. It is a constant area section model with a much more stable operation over a wider range of inlet and outlet temperatures. A schematic of the ejector geometry is shown in Figure 3.2, with the dimensions summarized in Table 3.1. This ejector has an Area Ratio $A_r = (D/n_d)^2 = 5.76$, slightly lower than the range suggested by Huang *et al.* [1999] for an optimal entrainment ratio ω_r ($A_r = [7 - 16]$). Similarly, the diffuser is in fact formed by two consecutive diverging sections, with a total L/D ratio of 25, well over the value of $L/D = 8$ recommended by Henzler [1983] for minimizing subsonic compression losses.

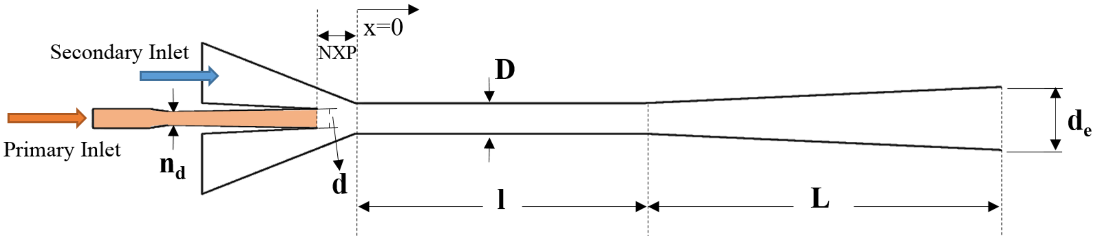

Figure 3.2 Schematics of the baseline ejector geometry used in the numerical benchmark. Dimensions values are provided in Table 3.1.

Table 3.1 Main dimensions of the baseline ejector geometry for the CFD benchmark. After García del Valle *et al.* [2014].

Parameter	**Value** [mm]
Primary nozzle throat diameter, n_d	2.00
Primary nozzle exit diameter, d	3.00
Nozzle exit position, NXP	-5.38
Mixing chamber diameter, D	4.80
Mixing chamber length, l	41.39
Diffuser length, L_d	120.15
Diffuser exit diameter, d_e	20.00

Numerical boundary conditions are based on the characteristic operating points (OP) shown in Table 3.2 along with the corresponding experimental ejector performance. It must be pointed out that both primary and secondary inlet temperatures comprise a 10 °C superheat to prevent spontaneous condensation through the ejector. Furthermore, the reported outlet pressure corresponds to the double-choke limit (p_{lim}) and was determined based on the condenser temperature T^{sat}_{out}.

Calculations were performed using the approach described in Sections 3.1 through 3.4, with the *Coupled* pressured-based algorithm. For the cases involving the high-Reynolds number turbulence approach, a mesh conformed by 51000 irregular elements with five

Table 3.2 Operating conditions used in the benchmark study, and corresponding to the experiments of García del Valle *et al.* [2014].

	OP1	**OP2**	**OP3**
Primary Inlet			
p_{prim} [kPa]	2598.04	2888.83	3188.14
T_{prim} [°C]	89.37	94.39	99.15
Secondary Inlet			
p_{sec} [kPa]	414.61	414.61	414.61
T_{sec} [°C]	20.00	20.00	20.00
Outlet			
p_{out} [kPa]	757.22	826.57	897.12
T_{out}^{sat} [°C]	29.41	32.48	35.41
Performance			
ω_r [-]	0.494	0.398	0.339
P_{ratio} [-]	1.826	1.994	2.164

wall-adjacent prismatic layers was used. For the low-Reynolds number cases, the mesh contained 645000 structured elements, with 21 wall-adjacent prismatic layers at a growing rate of 1.15.

3.5.2 Influence of the Gas Properties Model

Figure 3.3 compares the ejector entrainment ratio at operating points OP1, OP2 and OP3 for the three assessed gas models with the experimental data of García del Valle *et al.* [2014]. The perfect gas model fails to predict the entrainment ratio within an acceptable accuracy whatever the operating conditions, with a maximum deviation of 19% at OP2 and OP3. The two real gas models provide essentially the same results. In particular at OP1 (the lowest p_{prim}/p_{sec} ratio) the deviation relative to the experimental value is less than 1%. At OP 2 (resp. OP 3), deviations are 4.4% (resp. 5.8%) and 6% (resp. 3.4%) for the REFPROP 7.0 and RKS models respectively.

The slight entrainment ratio over prediction increases with the outlet pressure but the two real gas models show negligible differences among each other. Nonetheless, a look at Table 3.3 shows that the actual mass flow rates between these two models somehow differ but the differences cancel out. Values obtained using the thermodynamic model described in Chapter 4 are included as a reference. It is seen that the RKS method underestimates $\dot{m}_{prim}$ but agrees well in the $\dot{m}_{sec}$, whereas the REFPROP 7.0 database has the opposite behaviour. The perfect gas model under estimates $\dot{m}_{prim}$ and over estimates $\dot{m}_{sec}$, which explains its consistent over prediction of the entrainment ratio.

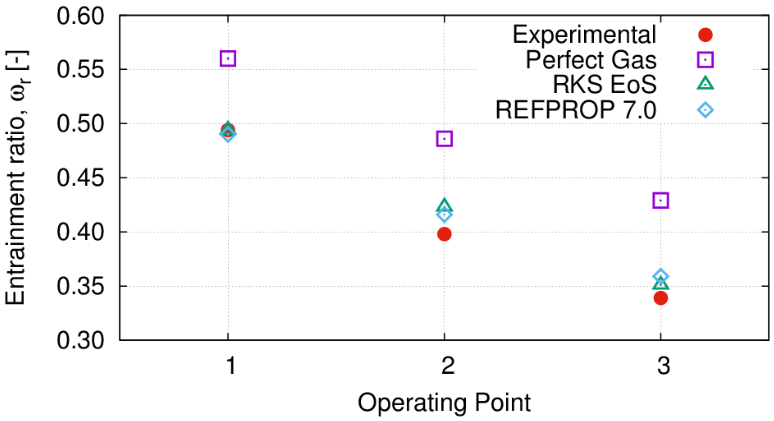

Figure 3.3 Entrainment ratio ω for the three operating points. Comparisons between three gas models using the standard $k-\epsilon$ model and the experimental data of García del Valle *et al.* [2014].

Table 3.3 Primary and secondary ejector mass flow rates obtained with the three different gas models and the thermodynamic model described in Chapter 4. Results for the ejector at conditions OP1 using the standard $k-\epsilon$ turbulence model.

Model	$\dot{m}_{prim}$ [kg/s]	$\dot{m}_{sec}$ [kg/s]	ω_r [-]
Perfect Gas	0.02906	0.01626	0.560
RKS EoS	0.03185	0.01572	0.494
REFPROP 7.0	0.03361	0.01649	0.490
Thermodynamic (Chapter 4)	0.03356	0.01576	0.470

Further details can be drawn from Figure 3.4, which depicts the distributions of static pressure, Mach number and temperature along the centreline of the ejector at OP1. Though the profiles for p and Ma are quite alike among the three models, important differences are observed concerning temperature. In general, these profiles express the most important flow features: the primary flow expansion for $-0.04\,\text{m} < x \leq 0.0\,\text{m}$, followed by a series of oscillations indicating the motive jet shock cells up to the end of the CAS where a normal shock is observed before the subsonic compression. Experimental observations show that rather than a normal shock, a system of shock waves appears in the mixing area (see Section 2.4.1). It will be shown in Section 3.5.3 that the numerically calculated shock structure in this region is sensible to the chosen turbulence model. It is expected for pressure profiles to be very similar, as these are somehow prescribed by the chosen boundary conditions. In terms of the Ma number, the perfect gas model predicts a slightly higher value in the CAS but all three models predict a normal shock wave of relatively weak intensity located at around $x = 0.04\,\text{m}$, the outlet of the mixing chamber. As it can be seen in the zoomed areas, the exact position and pressure jump of the shock wave slightly varies with the thermodynamic model. The greatest differences are observed in the temperature profiles, in particular at the NXP, the average values are 57.4 °C, 47.3 °C and 11.7 °C respectively for the perfect gas, RKS and REFPROP 7.0 models, which would explain the variations in $\dot{m}_{prim}$ observed in Table 3.3, as a lower NXP temperature implies lower exit velocity (assuming a constant c_p behaviour). The differences in temperatures persist through the rest of the flow process such that, at the outlet, the average values are 64.5 °C, 57.5 °C and 49.5 °C respectively for the perfect gas, RKS and REFPROP 7.0 models. These discrepancies are important as the outlet condition has an important role in the ejector efficiency calculation and, from a system perspective, the condenser cooling requirement would be very different for each case.

These observations are in relative agreement with the results of Bartosiewicz *et al.* [2005], who pointed out that despite observing differences in internal flow structure for different turbulence models, all computations provided practically the same entrainment ratio value. It is shown here that these observations might stem, in particular, from an cancellation of the errors incurred by the models in the calculation of the primary and secondary mass flow rates. It points out also the importance of using parameters other than ω_r and P_{ratio} for model validation, as these are to some extent heavily influenced by the imposed boundary conditions.

Table 3.4 summarizes the main thermophysical properties used or calculated by the three thermodynamic models. It shows in particular the importance of using real gas models as the heat capacity (and so the Prandtl number) may vary in a large range. Surprisingly, both real gas models predict very different results for the Prandtl number and the heat capacity, while predicting the same entrainment ratio and Mach and pressure distributions.

Table 3.4 Thermo-physical properties obtained by the three thermodynamic models for OP2 (total pressure $P \in [356.43-2950.56]$ kPa and total temperature $T \in [16.34 - 95.4]$ °C).

Properties / Model	**Perfect gas**	**RKS**	**REFPROP 7.0**
kinematic viscosity [$\times 10^{-5}$ Pa s]	1.44	1.44	1.05 – 1.62
Prandtl number [–]	1.54	1.55 – 1.83	0.78 – 1.12
thermal conductivity [W/m/K]	0.021	0.021	0.011 – 0.023
heat capacity [J/kg/K]	2240.1	2255.5 – 2667.7	871.8 – 1590
density [kg/m^3]	8.64 – 93.03	9.4 – 139.55	11.72 – 144.5

The particular differences between the RKS and REFPROP 7.0 models can be further explained using the compressibility factor (Z), *i.e.*: the ratio of the molar volume of a gas (evaluated through the corresponding equation of state) to the molar volume of an ideal gas at the same conditions. $Z \to 1$ as the gas behaviour approaches the ideal gas

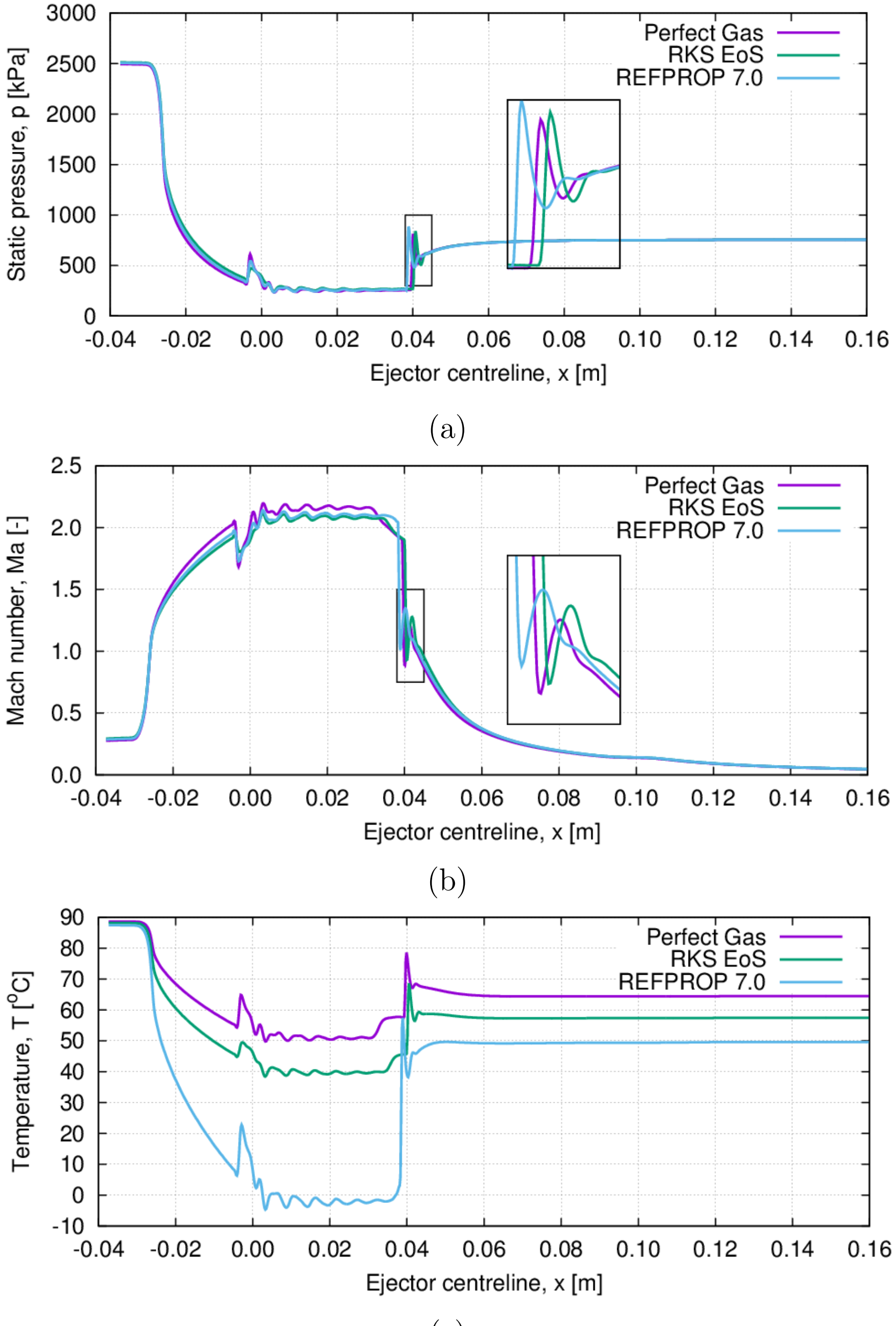

(a)

(b)

(c)

Figure 3.4 Comparisons of centreline profiles of (a) static pressure P [kPa], (b) Mach number Ma and (c) Temperature T (^oC) obtained with the different gas models for the ejector at OP1. Results obtained using the standard $k-\epsilon$ model.

law [Smith *et al.*, 1996]. Figure 3.5 compares the Z distribution between the RKS and REFPROP 7.0 models in the primary nozzle and mixing chamber for OP1. It is observed that the greatest deviations from the ideal gas behaviour occur through the motive jet expansion, yet the REFPROP model accounts more for these differences than the RKS EoS. Z is minimum at the inlet of the primary nozzle where the highest pressure levels are reached. In the secondary inlet, Z is equal to 0.91 for both models, close to the behaviour of a perfect gas. The over prediction already evoked above in terms of the entrainment ratio is then related to inaccurate predictions of the heat and fluid flow inside the primary nozzle.

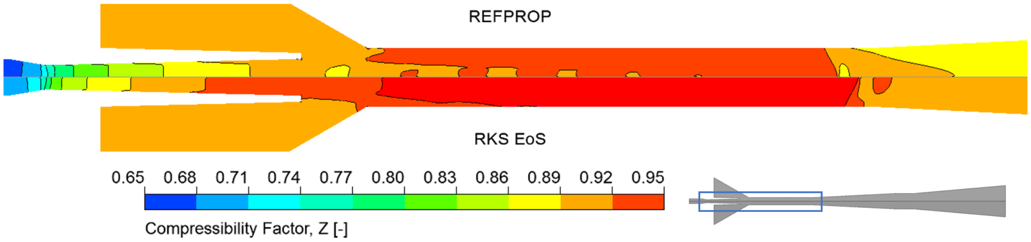

Figure 3.5 Maps of the compressibility ratio Z obtained by the standard $k-\epsilon$ model with the REFPROP 7.0 database and RKS equation of state for OP1.

As a conclusion, the use of the perfect gas model to investigate supersonic ejectors working with $R134a$, though being easier to use, is not advisable. The two real gas models perform quite well providing very similar results in terms of ejector performance and local flow features. It has been also checked that there is no noticeable differences between the two real gas models in terms of computational resources (CPU time and required memory size). Thus, they can be used confidently for single-phase supersonic ejector applications with $R134a$.

For other ejector designs and other operating conditions, the REFPROP model should nevertheless be used with a certain caution as the temperature range could be easily exceeded during the convergence process, causing the solution to fall in regions where the fluid properties are not defined. It may be particularly true during the first statistical iterations where the calculations are highly oscillating if initial conditions are not correctly chosen. Mazzelli and Milazzo [2015] obtained very low convergence rate and weak stability using the REFPROP database for a supersonic ejector working with $R245fa$, reporting better behaviour with the Peng-Robinson model.

3.5.3 Influence of the Turbulence Model

Four two-equation turbulence models described in Section 3.1.1 have been compared to the experimental data of García del Valle *et al.* [2014]. For all calculations, the real gas model based on the REFPROP 7.0 database has been used.

Table 3.5 shows the relative deviation ($\varepsilon = |\omega_{pred} - \omega_{exp}|/\omega_{exp}$) between the predicted ω_{pred} and the experimental $\omega_{exp} = 0.398$ values of the entrainment ratio for OP2. The standard $k-\epsilon$ model with standard wall functions offers the best accuracy, with a deviation of 4.27%. This model is known to predict well wall-bounded flows with relatively smooth mean pressure gradients, which is the case in the region confined between the primary nozzle exit and the appearance of the shock wave in the mixing chamber. For this particular conditions, the advanced versions of the $k - \epsilon$ model, the realizable $k - \epsilon$ and $k - \epsilon$ RNG, do not show any improvement in terms of the entrainment ratio prediction. In agreement with the observations of Hemidi *et al.* [2009a], the high-Reynolds number $k - \omega$ SST model presents a greater deviation than the standard $k - \epsilon$ model (6.78%), albeit a slight improvement is obtained by switching to the low-Reynolds number formulation.

Table 3.5 Relative deviations ε of the numerical values from the experimental data of García del Valle *et al.* [2014] in terms of the entrainment ratio for OP2 ($\omega_{exp} = 0.398$). Comparisons between the four two-equation models used in their high- (HRN) or low-Reynolds number (LRN) formulation.

Turbulence Model	**Relative deviation ε (%)**
standard $k - \epsilon$ (HRN)	4.27
realizable $k - \epsilon$ (HRN)	8.79
$k - \epsilon$ RNG (HRN)	6.03
$k - \omega$ SST (HRN)	6.78
$k - \omega$ SST (LRN)	5.70

Figure 3.6 compares the numerically predicted operation curves obtained by three turbulence models with the experimental data reported by García del Valle *et al.* [2014]. There is a good overall agreement between the standard $k - \epsilon$, the $k - \omega$ SST in its low-Reynolds number approach and the experimental results. The difference is around 4% along the on-design conditions ($T_{out}^{sat} < 33\,°\mathrm{C}$). According to these models, the critical operation point is $T_{out}^{sat} = 33\,°\mathrm{C}$, which marginally differs from the experimental value $T_{out}^{sat} = 32.5\,°\mathrm{C}$. Off-design conditions operate up to approximately $T_{out}^{sat} = 36\,°\mathrm{C}$, which corresponds to the breakdown pressure and the beginning of the ejector malfunction region. As a conclusion, the low-Reynolds number approach significantly improves the predictions of the entrainment ratio for a given $k - \omega$ SST model, reproducing well the ejector global performance. As a comparison, using the high-Reynolds $k - \omega$ SST model, entrainment ratio deviations

of 10% and 12.9% have been reported on air by Hemidi *et al.* [2009a] and on steam by Sriveerakul *et al.* [2007] ejectors.

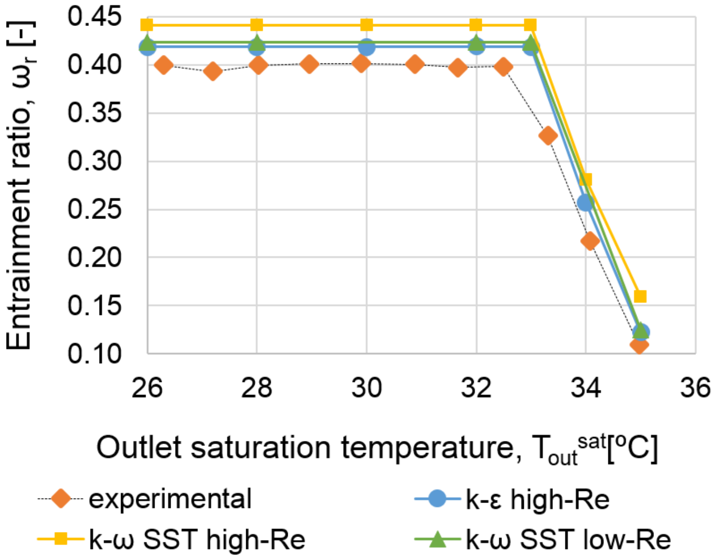

Figure 3.6 Comparison in terms of the ejector operating curve between the three turbulence models and the experimental data of García del Valle *et al.* [2014]. Results obtained for OP2 using the REFPROP 7.0 Database.

Both the standard $k-\epsilon$ and low-Reynolds number $k-\omega$ SST models accurately predict the entrainment ratio over the whole operation curve. Yet, the local flow features and especially the shock wave structure may differ significantly [Bartosiewicz *et al.*, 2005; Hemidi *et al.*, 2009b]. Figure 3.7 displays static pressure and Mach number profiles along the CAS and first diverging section centre line for OP1. It is clearly shown that the $k-\epsilon$ family predicts a normal shock wave in the mixing chamber ($0.030\,\mathrm{m} < x < 0.035\,\mathrm{m}$), whereas the $k-\omega$ SST predicts a series of oblique shock waves slightly earlier in this region (at around $x = 0.024\,\mathrm{m}$), very similar to the typical shock cells encountered in supersonic underexpanded jets. This oblique shock-wave structure in the CAS of supersonic ejectors has been reported both experimentally [Bouhanguel *et al.*, 2011; Zhu and Jiang, 2014b] and numerically [Bartosiewicz *et al.*, 2006; Scott *et al.*, 2011]. The low-Reynolds number $k-\omega$ SST model predicts a shock train with a relatively lower intensity as the amplitude of the pressure and Mach number oscillations are smaller than those predicted by the high-Reynolds number $k-\omega$ SST version.

Figure 3.8 shows the iso-contours of $Ma > 1$ in the mixing region at the critical conditions for the standard $k-\epsilon$ and both $k-\omega$ SST turbulence models. It confirms that where the standard $k-\epsilon$ model predicts a single normal shock wave in the mixing chamber, both $k-\omega$ SST models predict a series of shocks, with the high-Reynolds number formulation

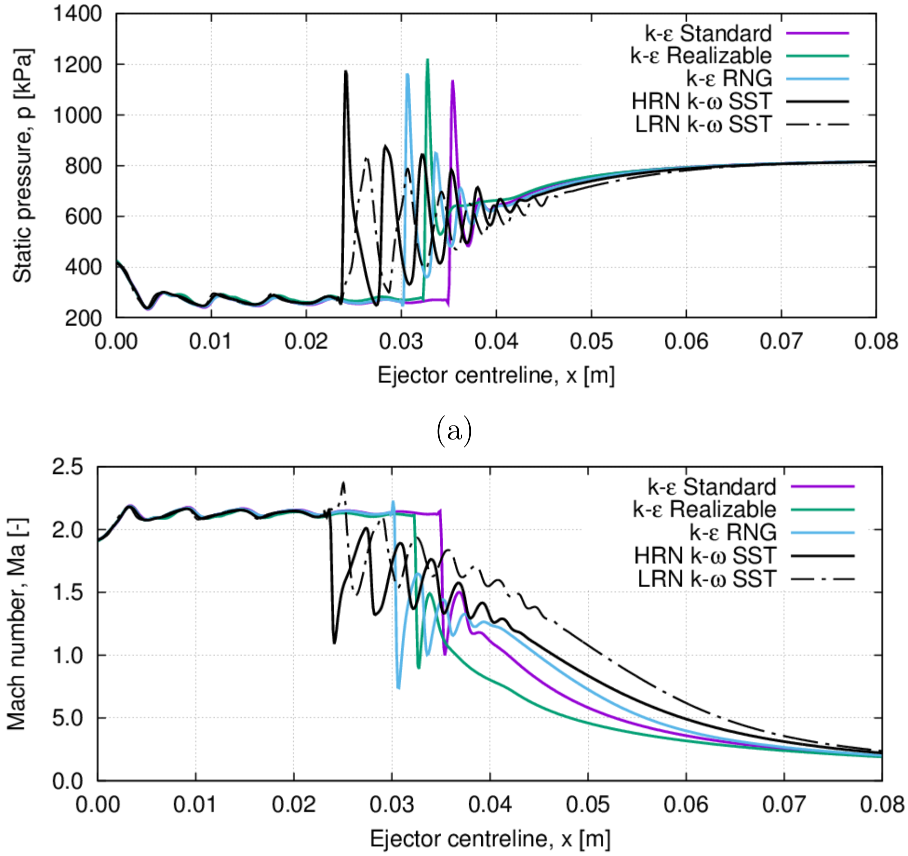

(a)

(b)

Figure 3.7 Comparison in terms of (a) static pressure and (b) Mach number profiles at the ejector center line for the different RANS turbulence models. Conditions corresponding to OP2. Experimental data after García del Valle *et al.* [2014].

anticipating the onset location. It is interesting to note that the good capture of the shock train structure is inherent to the turbulence model given the fact that both the standard $k-\epsilon$ and the high-Reynolds number $k-\omega$ SST model were applied on the same mesh, and that both $k-\omega$ SST formulations provide the same results despite using very different mesh grid arrangements. These observations suggest a strong link between the near wall profiles and the general flow structure through the ejector, since the both $k-\omega$ SST formulations are designed to be directly usable all the way down to the wall through the viscous sublayer.The $k-\omega$ SST low-Reynolds number combines then the good prediction of the shock-structure by the high-Reynolds number $k-\omega$ SST model and of the entrainment ratio by the high-Reynolds number $k-\epsilon$ model.

In order to provide further insight into the different behaviours between the standard $k-\epsilon$ and $k-\omega$ SST models, Figure 3.9 shows the contours of the turbulence kinetic

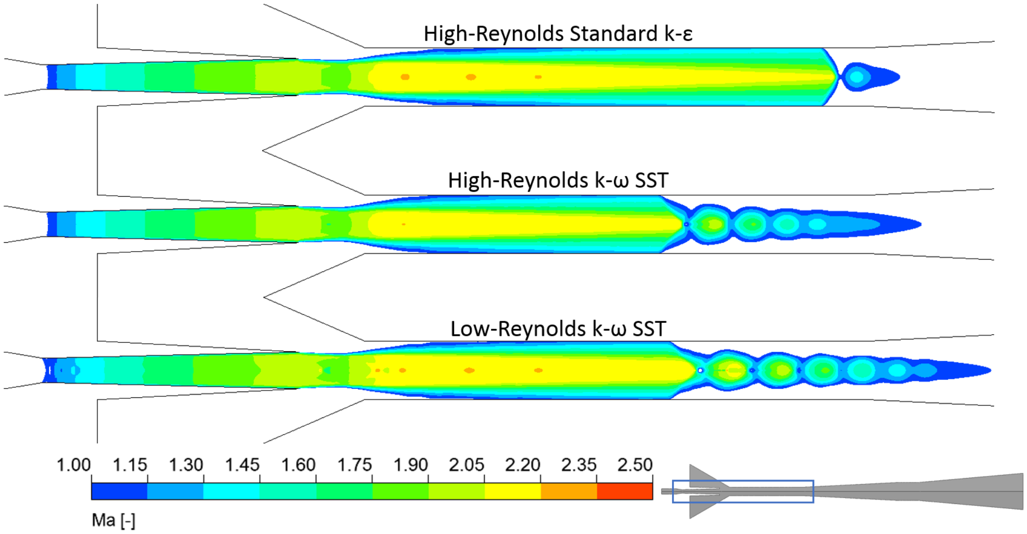

Figure 3.8 Comparison in terms of Ma number iso-contours in the mixing region of the ejector under OP1 conditions using the Standard $k-\epsilon$, high- and low-Reynolds number $k-\omega$ SST models.

energy k [$\mathrm{m}^2/\mathrm{s}^2$] for OP1. The maps obtained by other models in each family exhibit similar results and are then not shown here for sake of clarity. Turbulence kinetic energy reaches particularly high values in two regions within the ejector: the mixing shear layer developing at the trailing edge of the primary nozzle exit and at the exact location of the shock wave in the constant area section (indicated by the black iso-lines). Within the shear-layer, the maximum values of k are equal to $1475\,\mathrm{m}^2/\mathrm{s}^2$ and $1780\,\mathrm{m}^2/\mathrm{s}^2$ for the standard $k-\epsilon$ and $k-\omega$ SST models respectively ($1690\,\mathrm{m}^2/\mathrm{s}^2$ and $2440\,\mathrm{m}^2/\mathrm{s}^2$ respectively for the RNG and realizable models). Higher values of the turbulence kinetic energy in the shear-layer have been related to enhanced inlet fluid mixing and higher entrainment ratios [Rao and Jagadeesh, 2014]. At the shock wave location, the maximum turbulence kinetic energy is $3170\,\mathrm{m}^2/\mathrm{s}^2$ (resp. $\simeq 10^3\,\mathrm{m}^2/\mathrm{s}^2$) for the standard $k-\epsilon$ (resp. $k-\omega$ SST) model.

Figure 3.10 shows the iso-contours of turbulent viscosity obtained with the standard $k-\epsilon$ and high-Reynolds $k-\omega$ SST models for operating conditions OP1. The turbulence viscosity ratio is defined as the ratio of turbulent viscosity (ν_T) to kinematic viscosity ν, the latter being a variable when using the REFPROP 7.0 database. It has been checked that the same contours are obtained for ν whatever the two-equation model used. The turbulence viscosity ratio is then a direct measure of the turbulence viscosity ν_T and so of the locations where the turbulence model prominently acts and the energy it dissipates. The maximum turbulence viscosity ratio is observed in all cases downstream of the shock waves at the end of the mixing chamber or at the inlet of the diffuser, where flow detachment is

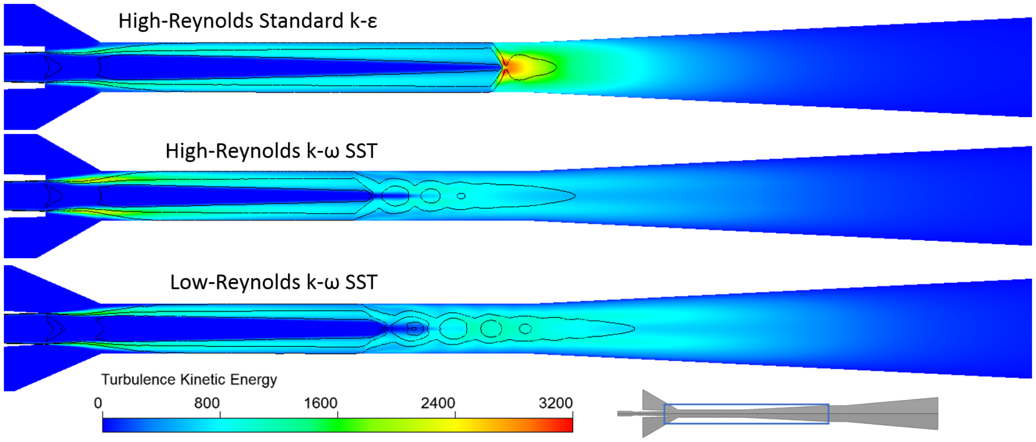

Figure 3.9 Comparison in terms of turbulence kinetic energy maps under OP1 conditions using the standard $k-\epsilon$ and the high- and low-Reynolds number $k-\omega$ SST models coupled to the REFPROP 7.0 database.

likely to occur. It is noteworthy that the standard $k-\epsilon$ model is much more dissipative, in particular at the shock wave location.

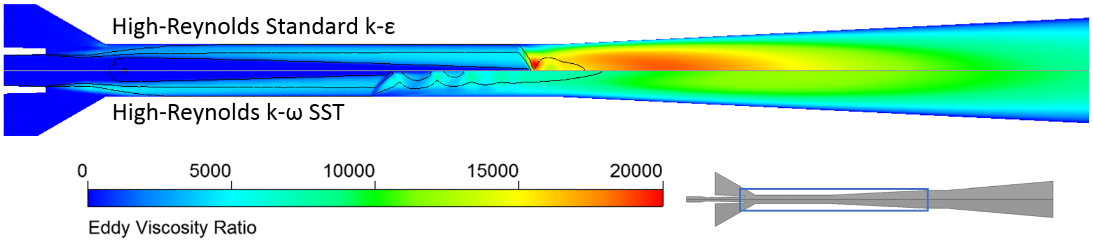

Figure 3.10 Comparison in terms of turbulent viscosity ratio maps under OP1 conditions between the standard $k-\epsilon$ and high-Reynolds number $k-\omega$ SST models coupled to the REFPROP 7.0 database.

In terms of the comparison between the low- and high-Reynolds $k-\omega$ SST formulations, it must be remarked that the maps of the turbulence kinetic energy and turbulence viscosity ratio are virtually the same but with slightly different maximum values. For the low-Reynolds number approach, $k_{max} = 1793\,\mathrm{m}^2/\mathrm{s}^2$ and $(\nu_T/\nu)_{max} = 16614$. The structure and the position of the shock wave seem to be better captured by the $k-\omega$ SST model either in its high- or low-Reynolds number formulation. The latter improves the flow field predictions within the boundary layers. The secondary fluid passage being confined close to the wall of the mixing chamber, the value of the predicted entrainment ratio is also improved. On the other hand, the advanced versions of the $k-\epsilon$ model do not improve the predictions of the standard model both in terms of global performance and local flow features within the ejector.

3.6 Conclusions

Numerical modelling of the flow through single-phase ejectors represents a very challenging task due to its supersonic nature, involving the presence of an intense shear-layer, a series of oblique shock waves, shock-boundary layer interactions, turbulent mixing, etc. The current computational resources limit the direct solution of the governing equations, creating the need for a series of simplifications which reduce the complexity of the problem, but require critical choices concerning turbulence and gas properties modelling. In this regard, a benchmark has been carried out between the most usual modelling choices to determine the best combination in terms of computational costs and accuracy.

Concerning gas properties, the perfect gas model is not suitable for single-phase ejectors with common refrigerants, as it deviates up to 19% relative to the experimental entrainment ratio values. Regarding more complex approaches, *i.e.* the RKS equation of state and the REFPROP 7.0 database, very similar ω_r values are predicted over the assessed operating conditions, yet the latter seems to provide a more accurate calculation of the transport properties.

In terms of turbulence modelling, although the $k-\epsilon$ family stands out for its stability and lower experimental deviation, it does not well reproduce the near-wall flow structures, which results in a poorly predicted shock structure in the mixing section. On the other hand, the $k-\omega$ SST model in its low-Reynolds number formulation offers a similar global accuracy to that of the standard $k-\epsilon$ model with the added value of predicting an inner flow structure much more in agreement with experimental visualizations. Thus, the REFPROP 7.0 database and the $k-\omega$ SST low-Reynolds number turbulence model present the best combination for compressible RANS simulations of single-phase supersonic ejectors with refrigerants.

CHAPTER 4

Thermodynamic Ejector Model With Droplet Injection

This chapter describes the thermodynamic model developed to estimate the performance and the effects of droplet injection on a supersonic ejector with prescribed geometry and operating conditions. Validation is carried out in single-phase mode using experimental data of ejectors working with air, $R141b$, $R134a$ and $R245fa$, and in two-phase operation using experimental data of condensing CO_2 choked nozzles and $R134a$ ejectors at different degrees of superheat. The main assumptions and governing equations are presented respectively in Sections 4.1 and 4.2, the complete calculation procedure is described in Section 4.3 and the model validation is performed in Section 4.4.

4.1 Main Assumptions

The thermodynamic model solves the integral mass, momentum and energy conservation equations through the characteristic sections of the ejector as depicted in Figure 4.1. The effects of droplets are estimated following the premise that these are injected in the CAS and would change the main flow properties via mixing and breakup, which occurs at the injection point and through the shock waves. The general assumptions can be listed as follows:

- Flow is 1D and steady-state and its properties are uniform at each cross section L_i.
- The effective area locates at position $L3$. The pressure at this location (p_{L3}) maximizes the secondary mass flow rate.
- A normal shock wave occurs before the diffuser inlet, between positions $L5$ and $L6$.
- Both inlet flows and injected droplets are fully mixed before the onset of the normal shock, position $L5$.
- Losses are represented using expansion and compression isentropic efficiencies.

Concerning the droplet injection:

- Droplets are of the same chemical species as the ejector working fluid.
- Droplets are in complete mechanical and thermal equilibrium with the gas phase ($V_{slip} = 0$).

- Droplets are spherical and form a monodisperse phase.
- Droplets are injected between positions $L4$ and $L5$, normal to the main flow.
- Droplet breakup occurs right after injection at position $L4$ and through the normal shock.
- Coalescence and droplet deformation phenomena are neglected.

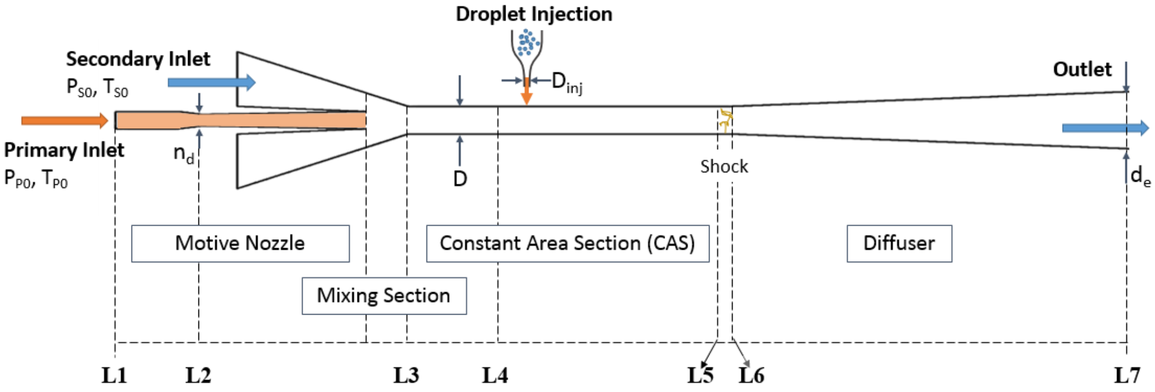

Figure 4.1 Main ejector sections for the thermodynamic model, including the assumed droplet injection location.

4.1.1 Input Data

- Thermodynamic state at both inlets: p_{prim}, T_{prim}, p_{sec} and T_{sec}.
- Diameters at the primary throat n_d, constant area section D and the diffuser exit d_e.
- Loss coefficients for the primary nozzle η_{prim}, secondary inlet η_{sec}, mixing section η_{mix} and diffuser η_{diff}.
- For droplet injection:
  - Injected fraction, $X_{inj} = \dot{m}_{injected\,droplets}/\dot{m}_{prim,\,without\,injection}$.
  - Droplet injection diameter, ϕ_{inj}.
  - Temperature of droplets at the injector, T_{inj}.
  - Injector diameter, D_{inj}.

4.1.2 Output Data

- Primary $\dot{m}_{prim}$ and secondary $\dot{m}_{sec}$ mass flow rates and entrainment ratio.
- Thermodynamic properties at every ejector section L_i indicated in Figure 4.1.
- Limiting pressure, p_{lim}.
- Ejector efficiency, η_{Elbel}.
- Exergy efficieny, η_{χ}.

4.2 Governing Equations

In the general case of a control volume with inlets ($in,1$ and $in,2$) and one outlet (out), the conserving equations take the following form:

Conservation of mass:

$$\rho_{in,1}V_{in,1}A_{in,1} + \rho_{in,2}V_{in,2}A_{in,2} = \rho_{out}V_{out}A_{out} \tag{4.1}$$

Conservation of momentum:

$$[p_{in,1}A_{in,1} + \dot{m}_{in,1}] + [p_{in,2}A_{in,2} + \dot{m}_{in,2}] = [p_{out}A_{out} + \dot{m}_{out}] \tag{4.2}$$

Conservation of energy:

$$\dot{m}_{in,1}\left[h_{in,1} + \frac{1}{2}V_{in,1}^2\right] + \dot{m}_{in,2}\left[h_{in,2} + \frac{1}{2}V_{in,2}^2\right] = \dot{m}_{out}\left[h_{out} + \frac{1}{2}V_{out}^2\right] \tag{4.3}$$

where ρ is the fluid density, V is the axial velocity through the cross sectional area A, P is the pressure, $\dot{m}$ is the mass flow rate and h is the specific enthalpy. Thermodynamic properties were determined using the *CoolProp* equation library [Bell *et al.*, 2014], which provides equations of state for a wide range of fluids using the Helmholtz energy formulations.

Two-phase thermodynamic states were defined via the combination of pressure, specific enthalpy or the specific entropy s and mixture quality x_l:

$$x_l = \frac{\dot{m}_v}{\dot{m}_v + \dot{m}_l} = \frac{b_m - b_l^{sat}}{b_v^{sat} - b_l^{sat}} \tag{4.4}$$

where b is any thermodynamic property different from P, T or ρ, and the subscripts m, l and v refer to the mixture, saturated liquid and saturated vapor, respectively. Saturation properties, denoted by the superscript sat, were evaluated at the local section pressure.

Losses incurred through the acceleration (primary and secondary inlets), mixing and compression (diffuser) stages of the ejector were represented by the following coefficients:

$$\eta_{prim}\eta_{sec} = \frac{h_{in} - h_{out}}{h_{in} - h_{out}^{is}} \tag{4.5a}$$

$$\eta_{diff} = \frac{h_{out}^{is} - h_{in}}{h_{out} - h_{in}} \tag{4.5b}$$

$$\eta_{mix} = \frac{p_{in}A_{in} - p_{out}A_{out} - \dot{m}_{out}V_{out}}{\dot{m}_{in}V_{in}} \tag{4.5c}$$

where the superscript *is* indicated properties evaluated through an isentropic process between the same states.

4.3 Calculation Procedure

The thermodynamic model is implemented within a Matlab environment. Starting from the motive nozzle, the flow properties at each section L_i are determined by applying corresponding forms of the mass, momentum and energy balances (Eqs. (4.1) to (4.3)).

4.3.1 Motive Nozzle Flow Rate [$P0$-$L2$]

The motive nozzle flow rate is determined by maximizing the mass flow rate per unit area function [G_{prim}, Eq. (2.11)] for the primary inlet conditions, following an iterative procedure based on the motive nozzle throat pressure (p_{L2}):

1. Assume $p_{L2} < p_{P0}$.
2. Determine $h_{L2}^{is} = h_{L2}^{is}(p_{L2}, s_0)$
3. Using η_{prim}, correct h_{L2} [Eq. (4.5)] between the primary inlet and $L2$
4. Determine $\rho_{L2} = \rho_{L2}(p_{L2}, h_{L2})$ and $V_{L2} = \sqrt{0.5(h_{P0} - h_{L2})}$
5. Determine $G_{prim} = \rho_{L2}V_{L2}$
6. Repeat steps 2 through 5 reducing the guess p_{L2} value until $max(G_{prim})$ is found
7. $\dot{m}_{prim} = max(G_{prim})A_{L2}$

At the end of this procedure, the properties at the motive throat are determined using p_{L2} and h_{L2}. This approach is based on the model of Ameur *et al.* [2016] for CO_2 transcritical ejectors in EERC, who reported a deviation of up to 14.2% in terms of the choking pressure for CO_2 nozzles.

4.3.2 Secondary Inlet [$S0$-$L3$]

Using a procedure analogous to that described in Section 4.3.1, the secondary stream critical pressure (p_{L3}) and choked mass flow rate per unit area (G^{*}_{sec}) are determined. It is assumed that p_{L3} is uniform across section $L3$ such that the area occupied by the primary jet is:

$$A_{L3,prim} = \frac{\dot{m}_{prim}}{V_{L3,prim}\rho_{L3,prim}} = \frac{\dot{m}_{prim}}{\sqrt{\frac{1}{2}(h_{po} - h_{L3,prim})}\rho_{L3,prim}} \tag{4.6}$$

where $h_{L3,prim}$ is determined through the motive flow expansion from primary inlet conditions corrected with η_{prim} and $\rho_{L3,prim}$ is determined using p_{L3} and $h_{L3,prim}$. The effective area for the secondary flow is therefore:

$$A_{L3,sec} = A_{L3} - A_{L3,prim} \tag{4.7}$$

and the entrainment ratio is:

$$\omega_r = \frac{\dot{m}_{sec}}{\dot{m}_{prim}} = \frac{G^{*}_{sec}A_{L3,sec}}{G^{*}_{prim}A_{L2}} = \frac{max\left[G\left(p_{L3,sec}, h_{S0}, s_{S0}\right)\right]A_{L3,sec}}{max\left[G\left(p_{L2}, h_{P0}, s_{P0}\right)\right]A_{L2}} \tag{4.8}$$

4.3.3 Mixing [$L3$-$L4$]

Assuming that both inlet flows are completely mixed at section $L4$, the following iterative procedure is applied between $L3$ and $L4$ to determine the mixture velocity V_{L4}, pressure p_{L4} and enthalpy h_{L4}:

1. Guess V_{L4}
2. Calculate p_{L4} [Eq. (4.2)] and h_{L4} [Eq. (4.3)]
3. Determine $\rho_{L4} = \rho_{L4}(p_{L4}, h_{L4})$
4. Calculate V^{g}_{L4} using Eq. (4.1)
5. If $|V_{L4} - V^{g}_{L4}| > tolerance$, substitute $V^{g}_{L4} \rightarrow V_{L4}$ and go back to step 1. Else, the calculation is finished and flow properties at position $L4$ are known.

4.3.4 Droplet Injection [$L4$-$L5$]

Droplets are injected before the onset of the normal shock wave. It is assumed that, immediately after injection, breakage occurs and the daughter droplet velocity ($V_{droplets}$) is equal to the gas velocity. The mass, momentum and energy equations following droplet injection are as follows:

$$\rho_{L4} V_{L4} A_{L4} + \dot{m}_{droplets} = \rho_{L5} V_{L5} A_{L5} = \dot{m}_5 \tag{4.9}$$

$$[p_{L4} A_{L4}] + \dot{m}_{L4} V_{L4} + \dot{m}_{droplets} V_{droplets} = [p_{L5} A_{L5} + \dot{m}_{L5}] \tag{4.10}$$

$$\dot{m}_{L4} \left[h_{L4} + \frac{1}{2} V_{L4}^2 \right] + \dot{m}_{droplets} \left[h_{droplets} + \frac{1}{2} V_{droplets}^2 \right] = \dot{m}_{L5} \left[h_{L5} + \frac{1}{2} V_{L5}^2 \right] + \Delta E_{br,4-5} \tag{4.11}$$

The last term in the R.H.S. of Eq. (4.11), representing the energy absorbed from the main flow for breakage, is determined using Eq. (2.17) (Section 2.5.2). The simultaneous solution of Equations (4.9), (4.10) and (4.11) gives the mixture properties just before the normal shock.

4.3.5 Normal Shock [$L5$-$L6$]

The shock train towards the end of the CAS is modelled as a normal shock wave occurring between sections $L5$ and $L6$ (with $p_{L5} < p_{L6}$, $s_{L5} < s_{L6}$, $\rho_{L5} < \rho_{L6}$ and $V_{L5} > V_{L6}$) and a second breakup step, with the corresponding breakage energy term ($\Delta E_{br,5-6}$) calculated using Eq. (2.17) (Section 2.5.2). The cross sectional area is assumed to be constant between both locations, and equal to A_{L3}.

The velocity V_{L6} is eliminated from Eqs (4.2) and (4.3) using Eq.(4.1), resulting in the system:

$$p_{L6} = p_{L5} + \rho_{L5} V_{L5}^2 \left(1 - \frac{\rho_{L5}}{\rho_{L6}} \right) \tag{4.12}$$

$$h_{L6} = h_{L5} + \frac{1}{2} V_{L5}^2 \left[1 - \left(\frac{\rho_{L5}}{\rho_{L6}} \right)^2 \right] - \frac{\Delta E_{br,5-6}}{\dot{m}_5} \tag{4.13}$$

which is resolved using the following iterative procedure:

1. Guess $\rho_{L6} > \rho_{L5}$
2. Calculate p_{L6} and h_{L6} using Eqs. (4.12) and (4.13) respectively
3. Determine $\rho^*_{L6} = \rho^*_{L6}(p_{L6}, h_{L6})$
4. If $|\rho_{L6} - \rho^*_{L6}| > tolerance$, substitute $\rho^*_{L6} \rightarrow \rho_{L6}$ and go back to step 1. Else, the calculation is finished and flow properties at position $L6$ are known.

4.3.6 Diffuser [$L6$-$L7$]

The ejector outlet conditions are determined by considering first an isentropic compression between $L6$ and $L7$, and then account for losses using η_{diff}. Since only the ejector exit area is known a priori at the outlet ($A_{L7} = \frac{\pi}{4}d_e^2$), an iterative procedure is followed:

1. Guess V_{L7}
2. Calculate h^{is}_{L7} by applying Eq. (4.3) between sections $L6$ and $L7$
3. Determine $p_{L7} = p_{L7}(h^{is}_{L7}, s_{L6})$ and $\rho^g_{L7} = \rho^g_{L7}(p_{L7}, s_{L6})$
4. Calculate $\dot{m}^g_{L7} = \rho^g_{L7} V_{L7} A_{L7}$
5. If $|\dot{m}^g_{L7} - \dot{m}_{L6}| > tolerance$, do $V_{L7} = V_{L7} + \Delta V_{L7}$ and go back to step 1
6. Correct h_{L7} with p_{L7} and η_{diff}, and determine flow properties at $L7$

Once h_{L7} and p_{L7} are known, the rest of flow properties at $L7$ can be determined. This outlet pressure is considered to be the maximum compression ratio achievable by the ejector at the given operating conditions [Galanis and Sorin, 2016].

4.4 Model Validation

Experimental data on single- and two-phase ejector based refrigeration cycles were used for comparison and validation of the thermodynamic model. Key validation points include: choked mass flows and entrainment ratio, limiting pressure, thermodynamic properties at different ejector sections and the effect of inlet vapour quality on the entrainment ratio.

4.4.1 Single-phase Operation

Figure 4.2 compares the predicted entrainment ratio values against experimental data from different studies [Chong *et al.*, 2014; Ersoy and Bilir Sag, 2014; García del Valle *et al.*, 2014; Hakkaki-fard *et al.*, 2015; Hemidi *et al.*, 2009a; Huang *et al.*, 1999] with varying dimensions, working gases and operating conditions. As a first step, friction and mixing losses are neglected here such that: $\eta_{prim} = \eta_{sec} = \eta_{mix} = \eta_{diff} = 1$.

The majority of predicted values lie within 10% of the corresponding experimental points when ω_r is in the range $[0.35 - 0.6]$, which is a typical range for most ejector applications in refrigeration systems. Deviations beyond 20% are found at the lower range of ω_r values, often associated with high motive to outlet pressure ratios. No clear tendencies are found between the model deviation and the entrainment ratio or the working gas.

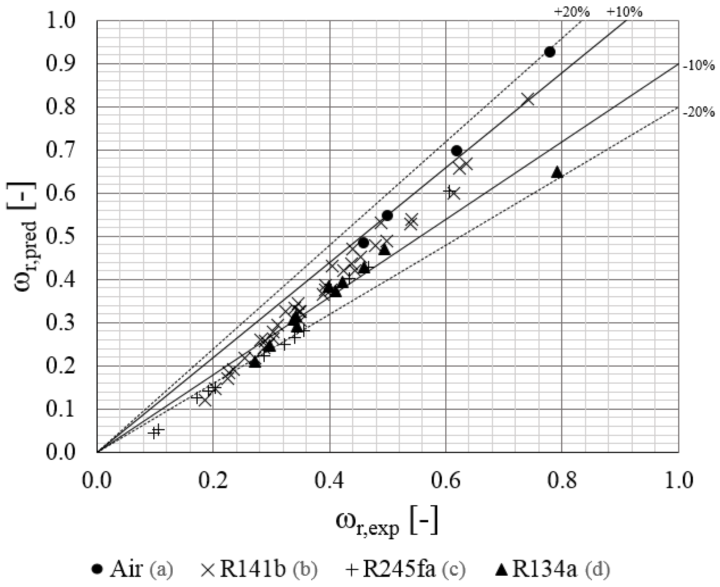

Figure 4.2 Comparison between the experimental and the predicted values of the entrainment ratio ω_r for different ejector configurations, under single-phase conditions, assuming 100% efficiencies. Data sources: (a) Hemidi *et al.* [2009a] and Chong *et al.* [2014], (b) Huang *et al.* [1999], (c) Dr. Aidoun (CanmetEnergy, personal communication), (d) García del Valle *et al.* [2014], Ersoy and Bilir Sag [2014] and Hakkaki-fard *et al.* [2015].

Influence of the loss coefficients

Figure 4.3 demonstrates the effect of the loss coefficients on the entrainment ratio ω_r and limiting pressure p_{lim} for a constant area ejector with gaseous $R134a$ as working fluid. Temperatures remain in the range 79 °C to 89 °C and 5 °C to 10 °C for the primary and secondary inlets respectively and a 10 °C superheat is applied to ensure vapor conditions [García del Valle *et al.*, 2014]. The loss coefficients are shown in Table 4.1, these being determined in a RANS study of the same ejector under the same operating conditions by performing energy balances through the motive nozzle, secondary inlet, mixing section and diffuser [Croquer *et al.*, 2016b]. Including losses in the thermodynamic model has a negligible effect on the predicted entrainment ratio, since it is only affected by the primary and secondary expansion coefficients, which are close to 1 in the present case. In terms of the limiting pressure, a better agreement is observed when using the adjusted loss coefficients η_{mix} and η_{diff}, showing the greater influence of the mixing and diffusion processes on the ejector compressing capacity. Overall, the model determines p_{lim} with an accuracy of 10%.

Table 4.1 Values of the loss coefficients deduced from the RANS analysis for different operating conditions. Determined after Croquer *et al.* [2016b].

Operation Point	p_{prim}[kPa]	T_{prim}[°C]	η_{prim}, η_{sec}	η_{mix}	η_{diff}
OP1	2598.04	89.37	0.98	0.623	0.892
OP2	2888.80	94.39	0.98	0.610	0.914
OP3	3188.14	99.15	0.98	0.566	0.925

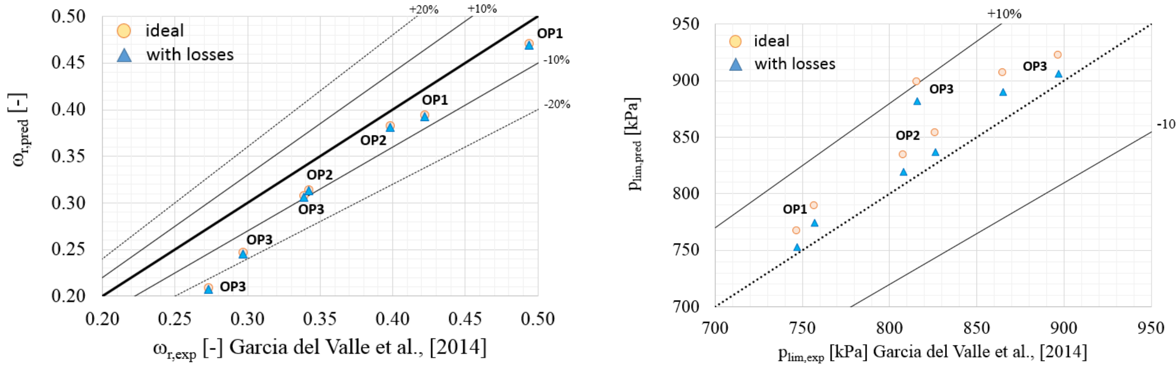

(a) (b)

Figure 4.3 Comparison between the experimental and predicted values of (a) the entrainment ratio ω_r and (b) limiting pressure p_{lim} for a single-phase R134a ejector. The operating conditions and loss coefficient values are shown in Table 4.1. Experimental data after García del Valle *et al.* [2014].

Comparisons at different sections of a supersonic ejector working with R134a

Table 4.2 shows a comparison between the thermodynamic model and RANS averaged values of pressure, temperature, Mach number Ma, specific enthalpy and specific entropy at four locations along the ejector: $L2$, $L4$, $L6$ and $L7$. Operating conditions correspond to OP2 of Table 4.1, with $T_{sec} = 20\,°C$, $p_{sec} = 414.6\,kPa$ and a fixed outlet pressure of 826.57 kPa. The RANS model is described in detail in Chapter 3. An average deviation of 3% is achieved at the primary throat ($L2$) and after mixing ($L4$). The greatest differences are observed at the start of the diffuser ($L6$): 15%, 18.53% and 19.48% for P, T and Ma respectively. These discrepancies may be partly explained by the 2D nature of the flow at this position highlighted by the RANS model [Croquer *et al.*, 2016a]. In terms of global quantities, the primary and secondary mass flow rates according to the thermodynamic model (resp. RANS model) are $\dot{m}_{prim} = 0.037\,53\,\mathrm{kg/s}$ and $\dot{m}_{sec} = 0.0143\,\mathrm{kg/s}$ (resp. $\dot{m}_{prim} = 0.037\,47\,\mathrm{kg/s}$ and $\dot{m}_{sec} = 0.0163\,\mathrm{kg/s}$), resulting in a difference of 0.15% and 14.3% respectively for the primary and secondary flow rates between both models.

Table 4.2 Comparison with the RANS results at different ejector sections for OP2. RANS results obtained using the REFPROP 7.0 and low-Reynolds number $k-\omega$ SST model.

Location	**Model**	p[kPa]	T[°C]	Ma[−]	h[J/kg]	s[J/kg/K]
L2	Therm.	1807.42	70.55	0.99	437616.82	1730.67
	RANS	1697.38	67.55	1.05	436267.09	1730.51
L4	Therm.	244.80	7.36	1.65	406385.75	1768.69
	RANS	264.10	7.60	1.58	406096.63	1761.80
L6	Therm.	686.65	46.11	0.62	433067.36	1781.21
	RANS	596.92	38.90	0.77	427724.66	1774.34
L7	Therm.	826.57	53.33	0.03	437734.85	1782.43
	RANS	826.57	52.25	0.03	436640.63	1779.08

4.4.2 Two-phase Operation

To assess the capability of the model in handling flows with a small liquid fraction, the primary mass flow rate of initially supercritical CO_2 through supersonic nozzles is compared with experimental values [Smolka *et al.*, 2013; Zhu *et al.*, 2017] at various inlet conditions indicated on the P-h diagram of Figure 4.4. Results are presented in Figure 4.5 for different values of the primary nozzle efficiency η_{prim}, showing that the adjustment of η_{prim} improves the model deviation from beyond 20% down to less than 10%. The best agreement is obtained with $\eta_{prim} = 0.75$ for the data in Figure 4.5(a) and with $\eta_{prim} = 0.85$ for the data in Figure 4.5(b).

The capacity of the present model to reproduce the effects of the primary superheat at the primary inlet ($\Delta_{OH} = T_{prim} - T_{prim,sat}$) on the entrainment ratio is shown in Figure 4.6 in comparison with the experimental values of Little and Garimella [2016] for $R134a$. An average deviation of 4% is achieved. The linear dependency of ω_r with the superheat Δ_{OH} is also well reproduced. For a 0 °C superheat, the calculated quality at the primary nozzle throat (resp. position $L3$) is 0.942 (resp. 0.933).

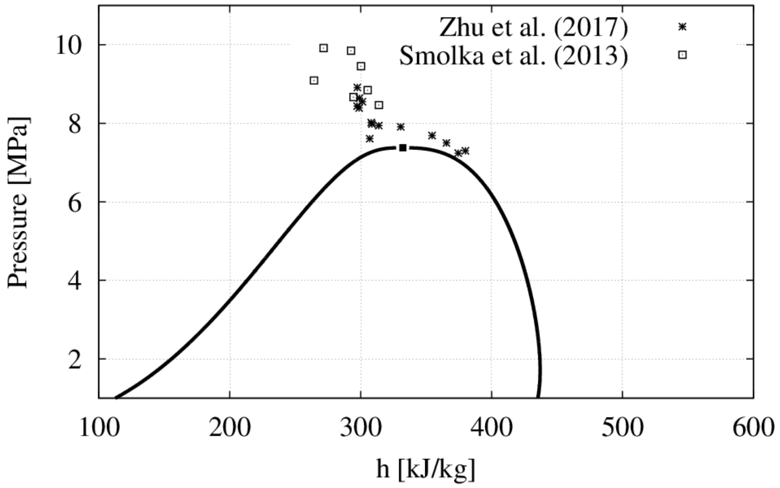

Figure 4.4 Location on a P-h diagram of the experimental inlet conditions used in the CO_2 choked mass flow rate model validation. Data sources: Smolka *et al.* [2013] and Zhu *et al.* [2017].

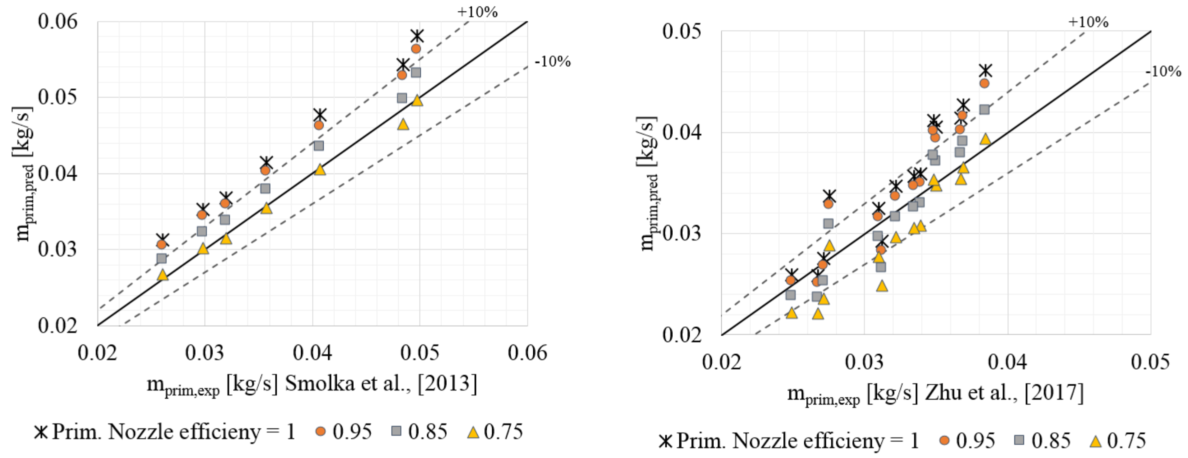

(a) (b)

Figure 4.5 Comparison between the experimental and predicted values of the primary mass flow rates for different ejector configurations under two-phase conditions. Data sources for CO_2 flows: (a) Smolka *et al.* [2013], (b) Zhu *et al.* [2017].

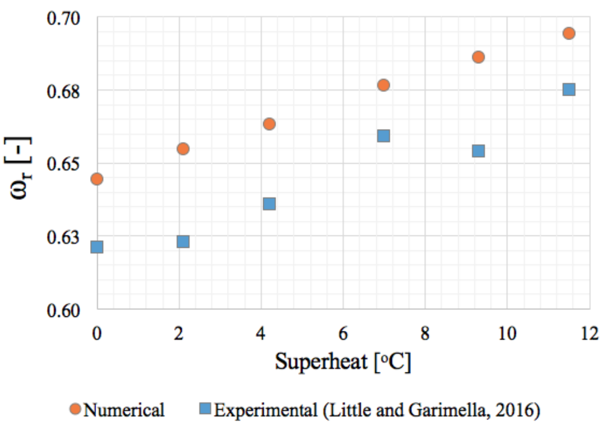

Figure 4.6 Comparison between the experimental and predicted values of the entrainment ratio ω_r for different superheat values. Experimental data after Little and Garimella [2016].

4.5 Conclusions

A thermodynamic model has been developed to predict performance of a supersonic gas ejector with droplet injection within the context of a HDRC. Input parameters comprise the inlet operating conditions and key geometrical parameters (primary throat, mixing section and diffuser exit diameters). Based on the successive application of mass, momentum and energy balances through the key sections of the ejector, the thermodynamic properties, entrainment ratio, pressure ratio and ejector efficiency are obtained as output results.

Validation against experimental data of single- and two-phase supersonic ejectors has been carried out. Under ideal single-phase operation, the entrainment ratio is determined with an average deviation of 18% for various working fluids (Air, $R141b$, $R134a$ and $R245fa$) and the double-choke limiting pressure with a mean deviation of 4.5% for $R134a$. The inclusion of loss coefficients has a negligible effect on the entrainment ratio results but reduces the p_{lim} deviation to 2.5%.

Under two-phase conditions, a deviation of about 10% in the prediction of the choked mass flow of CO_2 across convergent-divergent nozzles is obtained. A greater sensibility to the loss coefficients was observed in this case. The entrainment ratio dependence on the primary inlet superheat for a $R134a$ ejector was also captured, with good agreement versus experimental data.

PART III

RESULTS

CHAPTER 5

CFD Analysis of Single-Phase Gas Ejectors

This chapter presents an analysis of single-phase gas ejectors using the numerical CFD model described in Chapter 3. First, an in-depth analysis of the internal flow features of an $R134a$ ejector is carried out, with particular attention to the flow characteristics in the mixing section, the differences between double- and single-choke operation and the influence of operating conditions ejector performance and exergy destruction. Afterwards, a study of the influence on ejector and HDRC system performance when substituting the working fluid by novel refrigerants $R1234yf$ and $R1234ze(E)$ is presented. The chapter ends with a comparison of the predictions, resulting from thermodynamic and CFD models, of the global performance and flow scalability of supersonic air ejectors.

5.1 Flow Structure in $R134a$ ejector

A numerical analysis of the main flow features of a single-phase $R134a$ ejector was carried out. The flow domain, boundary conditions and numerical setup are based on the conclusions of the benchmark study described in Section 3.5. All results showed in this section were obtained using the REFPROP gas properties equations database and the low-Reynolds $k-\omega$ SST turbulence model. Operating conditions are summarized in Table 3.2. A general outlook of the ejector performance is given in Figure 5.1 for inlet conditions OP2. The calculated double-choke entrainment ratio and limiting conditions are respectively $\omega_r = 0.436$ and $T_{out}^{\text{sat,lim}} = 33\,°\text{C}$, which corresponds to a maximum compression ratio of 2.02. These results present a good agreement with the experimental data of the same ejector reported by García del Valle *et al.* [2014], respectively $\omega_r = 0.438$ and $T_{out}^{sat} = 32.48\,°\text{C}$.

5.1.1 General features in the CAS

The flow structure through the mixing section and the CAS is shown in Figure 5.2 for the three operating conditions OP1, OP2 and OP3. The ejector expansion ratio (p_{out}/p_{prim}) for these conditions is, respectively, 0.291, 0.286 and 0.281. The pressure range is limited to the interval $[0-600]$kPa to emphasize the high- and low-pressure zones. The black iso-lines denote $Ma = 1$. These start at the primary nozzle exit, following the shape of

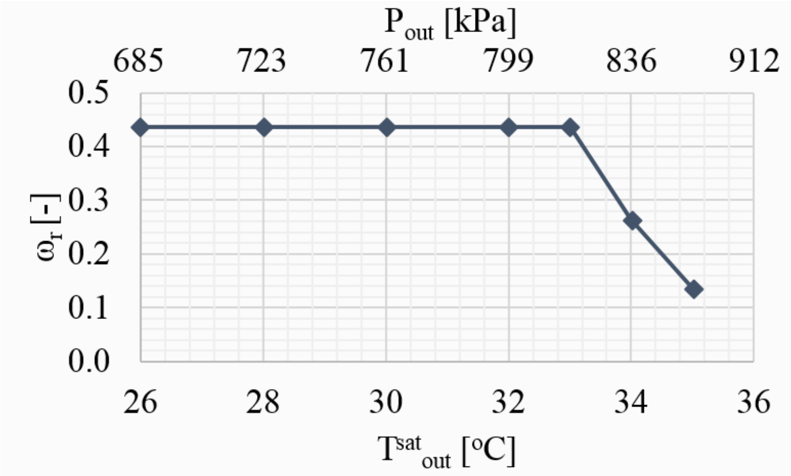

Figure 5.1 Ejector operation curve: entrainment ratio as a function of the outlet saturation temperature for fixed inlet conditions OP2. Results obtained with low-Reynolds $k-\omega$ SST turbulence model and REFPROP gas properties library.

the motive jet and moving then towards the CAS walls, indicating that the main flow is supersonic through the CAS and, thus, that the ejector is in double-choke regime. The supersonic region is characterized by a uniform pressure zone followed by oblique shocks. Given the small expansion ratio change through OP1-3, differences in the general flow structure are negligible except for two points: the primary jet core length (from the NXP to the start of the shock train) and the primary jet condition relative to the surrounding fluid in the mixing chamber. Greater detail on these differences is observed in Figure 5.3 which depicts pressure and Ma profiles at the ejector centreline for $-0.02\,\text{m} \leq x \leq 0.08\,\text{m}$. In particular, it is shown that as the expansion ratio decreases the shock start location, $x_{\text{shock onset}}$, moves towards the start of the CAS. By defining the shock train start position as the end of the motive jet potential zone, the latter has a dimensionless extension $[(x_{\text{shock onset}} - x_{NXP})/d]$ of 10.4, 9.5 and 9.2 respectively for OP1, OP2 and OP3, in line with experimental observations on air ejectors [Marinovski *et al.*, 2009].

Another interesting point observed in Figure 5.3 is the little variation in the p and Ma average values along the interval $0 \leq x \leq x_{\text{shock onset}}$, despite the differences in the primary inlet conditions, which differ by about $\sim 20\%$ from OP1 to OP3. The values in this region oscillate between 240 kPa and 310 kPa, with averages for OP1, OP2 and OP3 of respectively 270 kPa, 284 kPa and 304 kPa. It remains very close to the theoretical critical pressure for the secondary inlet conditions, 244 kPa. The pressure at the end of the motive nozzle varies with the inlet conditions, from 360 kPa at OP1 to 450 kPa at OP3, generating a drastic change in conditions at the NXP to adjust to the surrounding value in the mixing

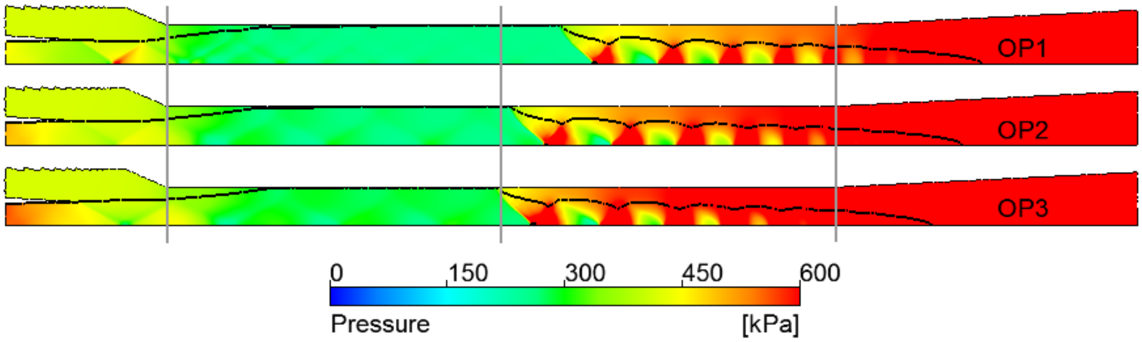

Figure 5.2 Static pressure distributions in the mixing chamber.

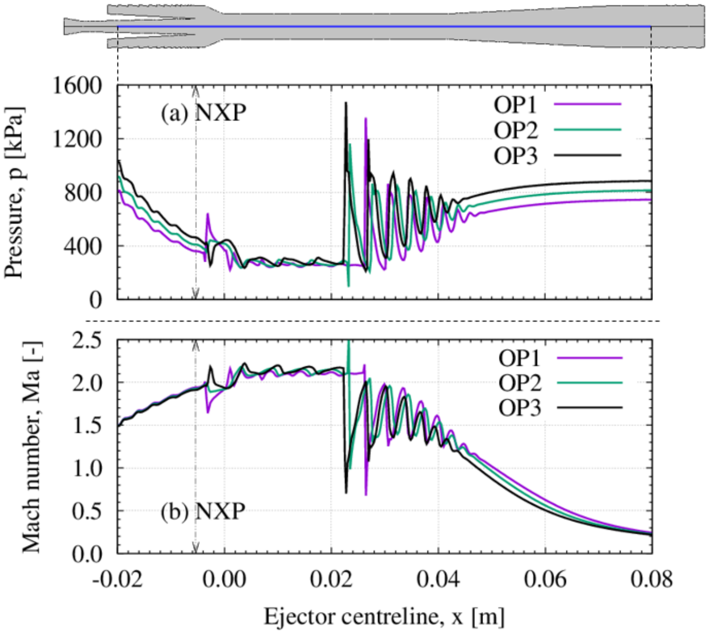

Figure 5.3 Centreline profiles of pressure and Ma number for OP1, OP2 and OP3.

chamber. This phenomenon is better appreciated in Figure 5.4 which compares pressure profiles from the primary nozzle exit towards the ejector axis for the primary flow and towards the start of the CAS for the secondary flow. It is noticeable that the secondary flow pressure profiles (dashed lines) are practically invariant with the primary or outlet conditions, at an average $p_{sec}^{NXP} \sim 411\,\text{kPa}$ (close to secondary inlet pressure value of 415 kPa). The decrease in pressure as one moves towards the wall of the CAS indicates flow acceleration, which results from entrainment into the shear layer, in agreement with the expansion of the sonic region seen in Figure 5.2.

Furthermore, a closer look at the profiles in Figure 5.4 for the same OP shows that the primary flow pressure at the NXP (p_{prim}^{NXP}) is not always lower than that of the entering secondary flow (p_{sec}^{NXP}), confirming that shear interactions play a role in the secondary flow entrainment. In addition, the primary jet can be either over-expanded (OP1, $p_{prim}^{NXP} < p_{sec}^{NXP}$), fully-expanded (OP2, $p_{prim}^{NXP} \sim p_{sec}^{NXP}$) or under-expanded (OP3, $p_{prim}^{NXP} > p_{sec}^{NXP}$), which greatly affects the cross-section area occupied by the motive jet at the start of the CAS. These effects are shown in Figure 5.5(a), with streamlines starting from the secondary inlet. At the mixing chamber, streamlines follow the $Ma = 1$ iso-line. In comparison with a horizontal line drawn from the nozzle exit ring, the over-expanded primary jet at OP1 contracts towards the centreline, whereas the exact opposite occurs at OP3 (at OP2 the motive jet is in balance with the surrounding pressure). Changes in the secondary flow area passage can be estimated by assuming that the primary jet at the start of the CAS is delimited by $Ma = 1$, leading to Figure 5.5(b) where the secondary mass flow rate has been plotted as a function of the secondary flow passage area at the start of the CAS. It was discussed in Section 2.4.2 that, under fixed inlet conditions, the sonic mass flow rate per unit area is the maximum of the function $G = G(p, h_o, s_o)$ Eq. (2.11), such that the secondary mass flow rate at double choke conditions is dependent only on the effective area size and throat pressure. The noticeable deviation from a linear trend in Figure 5.5(b) (reflected in the low value of $R^2 = 0.75$) suggests that, under fixed secondary inlet conditions, the choked secondary mass flow rate is influenced by factors other than effective area, such as the gain in momentum through the shear layer.

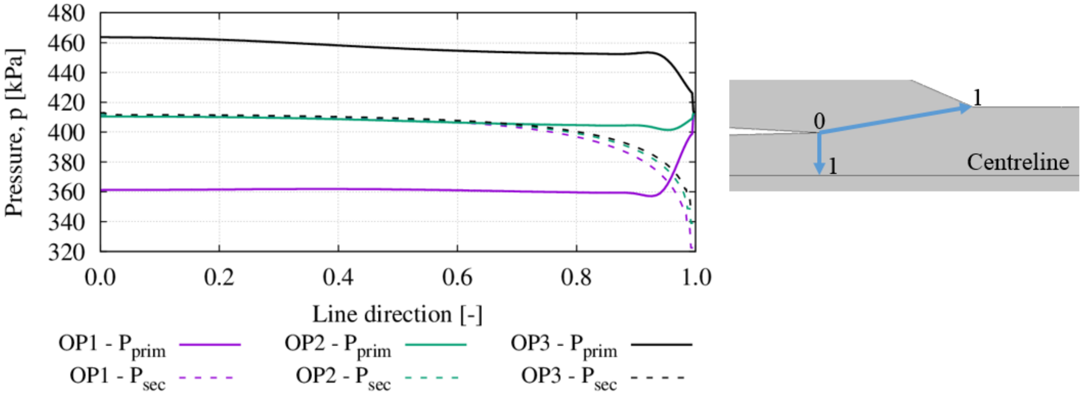

Figure 5.4 Pressure profiles for the primary and secondary flows as they enter the mixing section.

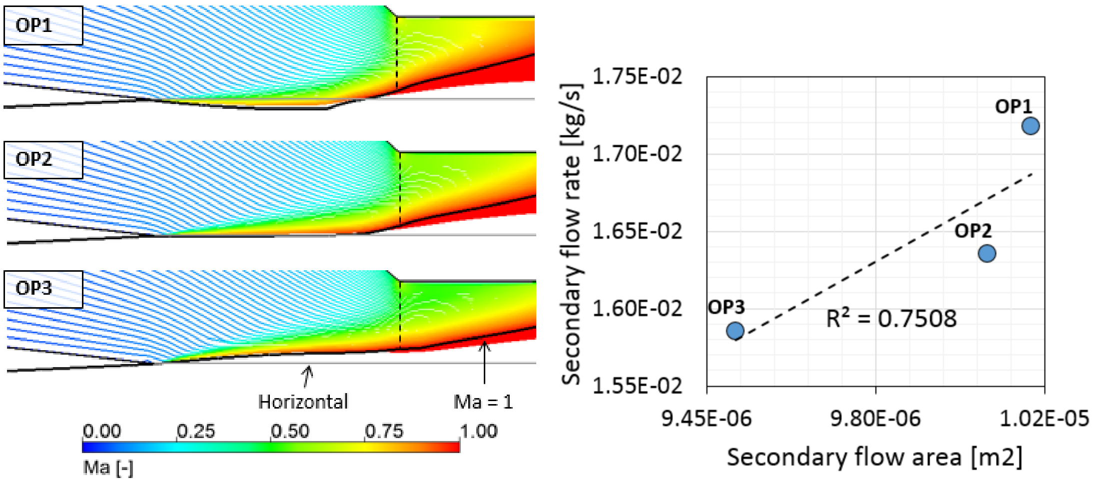

(a) (b)

Figure 5.5 Streamline patterns starting from the secondary inlet coloured by the Mach number. The iso-line denotes $Ma = 1$.

5.1.2 Differences between the single- and double-choke regimes

The influence of the outlet conditions on the flow features are shown in Figure 5.6 using contours of $Ma \geq 1$ at the CAS of the ejector with inlet conditions OP2. As expected, along double-choke operation (T_{out}^{sat} <33 °C) the flow structure up to the start of the shock train is not affected by the outlet pressure. As the outlet pressure increases, the motive jet potential zone contracts from $(x_{\text{shock onset}} - x_{NXP})/d = 16.2$ at T_{out}^{sat} <26 °C to 9.5 at T_{out}^{sat} <33 °C. The variation is shown in Figure 5.7, where the dashed line denotes a 2nd order relationship between $(x_{\text{shock onset}} - x_{NXP})/d$ and p_{out}/p_{prim} for the points in double-choke regime. If the off-design point is included, there is no conclusive trend. With a further outlet pressure augmentation the ejector enters the single-choke operation ($T_{out}^{sat} =$ 35 °C), revealed by the subsonic flow region persisting around the motive jet at the first half of the CAS. For this condition, the entrainment ratio is 0.206, meaning the secondary flow is still accelerated into the ejector although it is not supersonic.

Further insight into the changes from double- to single-choke operation can be appreciated in Figure 5.8, where radial p and Ma profiles have been plotted at position $x = 0$ m. At this position, the profiles for double-choke operation are superimposed. Considering first the pressure profiles (dashed lines), the average values are respectively 383 kPa and 420 kPa for the double- and single-choke cases, suggesting the secondary flow actually moves against a pressure gradient at the latter condition. This translates into much lower velocities, reflected in the Ma profiles (solid lines) which, although of similar shape, have very different minimum values (respectively $\sim$ 0 and 5.2 for single- and double-choke

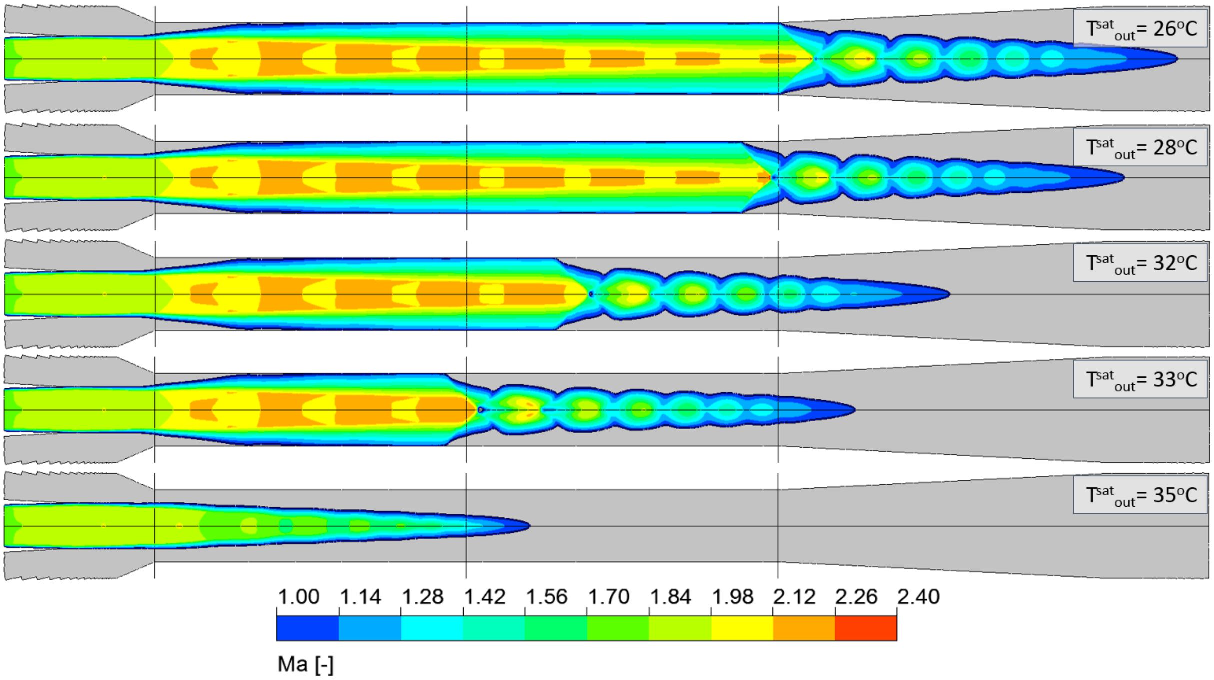

Figure 5.6 Ma number iso-contours for different outlet saturation temperatures. Results obtained for inlet conditions OP2.

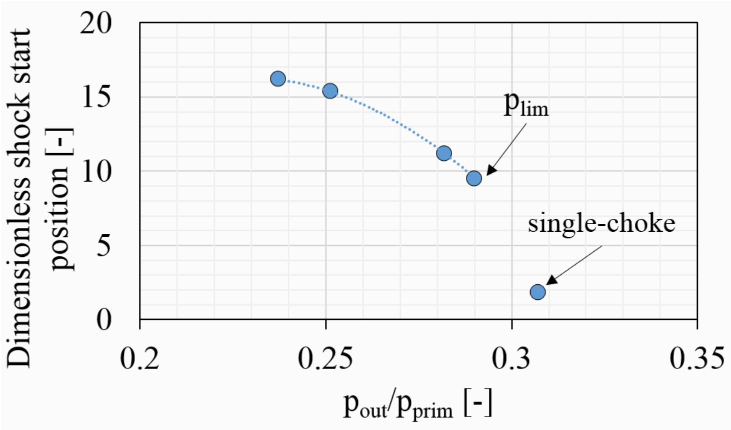

Figure 5.7 Variation in the dimensionless shock start position $(x_{\text{shock onset}} - x_{NXP})/d$ with the expansion ratio p_{out}/p_{prim}. Results obtained for inlet conditions OP2.

operation). By considering the $Ma = 1$ iso-lines as the limit of the motive jet, the secondary flow area is slightly smaller in the double-choke case. Although the difference along y is in the order of 0.1 mm, this translates into a cross-section reduction of 13%.

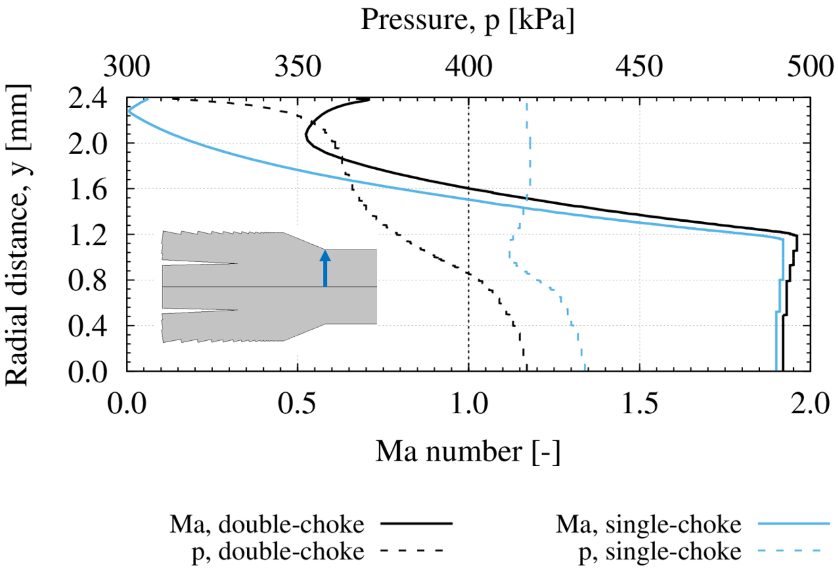

Figure 5.8 Radial pressure and Ma profiles at the start of the CAS. Results obtained for inlet conditions OP2.

5.1.3 Mixing

Figure 5.9 depicts distributions of the ratio of transversal velocity magnitude to the mean velocity vector magnitude ($|v| \,/\, |\bar{U}|$) and of turbulence kinetic energy (k) for the ejector at OP1 (Results for cases OP2 and OP3 showed essentially the same structure). These provide information on the transversal character of the flow and the localization of turbulence activity. It is seen that mixing between both inlet streams starts as interactions through the shear layer triggered at the NXP, and continues through the CAS and shock regions. Given the dominant axial character of the primary flow at the NXP, both inlet streams run in parallel along the first half of the CAS with mild diffusion through the shear layer. Complete mixing does not occur until the shock train region, where important transversal velocities appear due to the pressure fluctuations (representing about 25% of $|\bar{U}|$). This enhanced mixing is further verified by plotting the distribution of a passive scalar b_s injected with the secondary flow (Figure 5.10). The passive scalar follows a general transport equation with turbulent convection and diffusion terms as follows:

$$\frac{\partial}{\partial t} b_s + \frac{\partial}{\partial x_i}\left[(\bar{\rho}\tilde{u}_i b_s) - \left(\frac{\mu_t}{\bar{\rho} Sc}\right)\frac{\partial b_s}{\partial x_i}\right] = 0, \tag{5.1}$$

where $Sc = 0.7$ is the turbulent Schmidt number. Note that laminar diffusion has been neglected in Eq. (5.1). As shown in Figure 5.10 for OP1 (the results for OP2 and OP3 show little difference), there is a strong gradient of b_s in the direction normal to the sonic line.

Once the whole flow is supersonic, the secondary flow is confined to the outer diameter region, up until the shock train where interactions drive the scalar towards the centre of the ejector. Further down, the uniform colour reveals complete mixing of both inlet streams at the start of the diffuser.

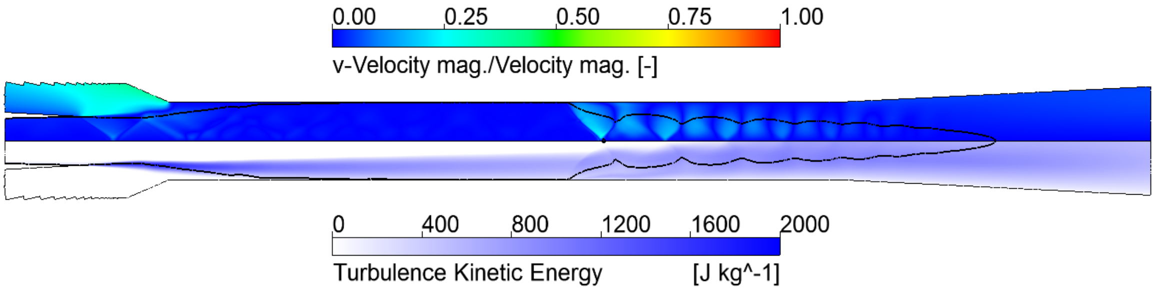

Figure 5.9 Ratio of the radial velocity component to the velocity magnitude in the mixing chamber. Results obtained for operating conditions OP1.

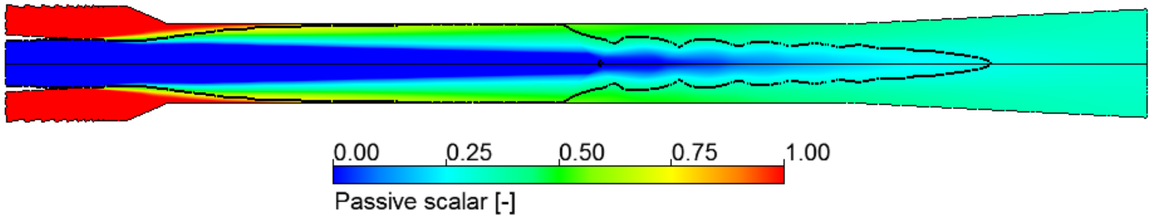

Figure 5.10 Mixing between the primary and secondary flows, represented by the distribution of a passive scalar injected in the the secondary inlet. Results obtained for operating conditions OP1.

Differences in mixing between single- and double-choke regimes are shown in Figure 5.11 for $T_{out}^{sat} = 32\,°C$ and $35\,°C$. The black iso-lines represent $Ma = 1$. In particular, an important reduction of the motive jet potential core occurs as the regime changes from double- to single-choke. Shortly after the end of the shock train, the inflows are completely mixed, as a result of increased interactions and turbulent activity in this region, a behaviour that has been captured in experimental studies of confined supersonic jets [Karthick *et al.*, 2016].

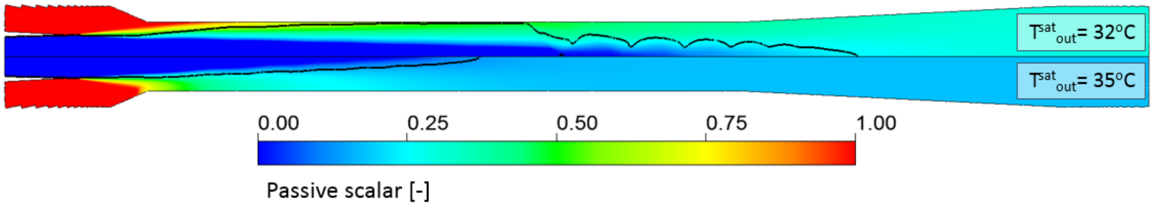

Figure 5.11 Maps of passive scalar distribution, comparison between double-choke ($T_{out}^{sat} = 32\,°C$) and single-choke ($T_{out}^{sat} = 35\,°C$) operations. The black iso-lines denote $Ma = 1$.

5.1.4 Ejector performance

Efficiency

Figure 5.12 shows the variation with varying operating conditions of three ejector performance indicators: the ASHRAE efficiency [ASHRAE, 1983] [Eq. (2.5)], the efficiency of Elbel and Hrnjak [2008] [Eq. (2.6)] and the exergy efficiency [Eq. (2.8)]. Taking into consideration all cases, the average values are $\eta_{ASHRAE} = 0.836$, $\eta_{Elbel} = 0.241$ and $\eta_{\chi} = 0.527$. Regarding Fig 5.12(a), only η_{ASHRAE} shows a clear tendency with the primary inlet conditions as it diminishes from OP3 (the highest p_{prim}) to OP1 (the lowest p_{prim}). This trend is opposite to the entrainment ratio (which reduces from OP1 to OP3), suggesting an increase in the ratio of specific compression to isentropic motive expansion works according to Eq. (2.5). It was observed while performing the energy accounting for this section that the compression ratio from OP1 to OP3 increases by about 18% whereas the expansion work available in the motive nozzle does so by barely 3%. However, it must be noted that the p_{out}/p_{prim} ratio range covered in Figure 5.12(a) is very limited. Figure 5.12(b) shows that for a wider range in double-choke regime η_{ASHRAE} remains invariant. Conversely, both η_{Elbel} and η_{χ} increase with the ratio p_{out}/p_{prim}. In Figure 5.12(b), ω_r and both inlet states are constant during double-choke conditions, which explains the trends in both parameters. On the one hand, for isentropic processes the increase in the outlet pressure reduces the isentropic expansion work $(h_{prim} - h_{out}^{is,prim})$ but increases $(h_{out}^{is,sec} - h_{sec})$, leading to a greater η_{Elbel}. On the other hand, the higher compression ratio leads to a higher exergy available at the outlet conditions, reflected in a better η_{χ}.

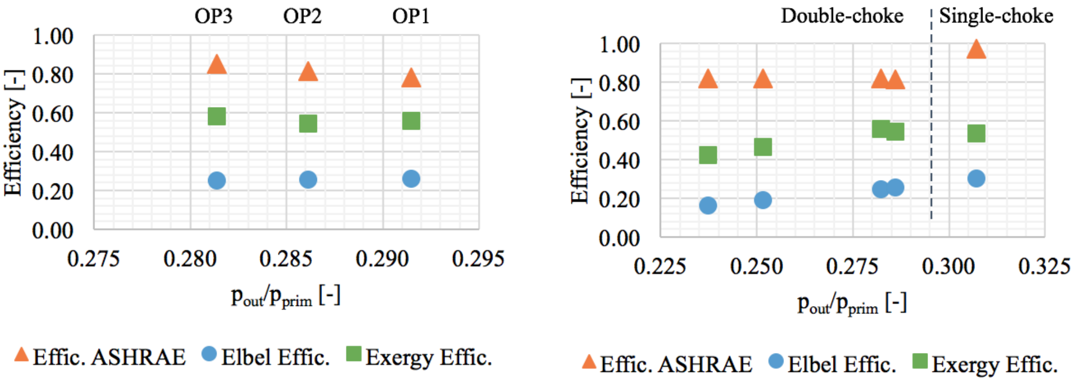

(a) (b)

Figure 5.12 Ejector performance indicators: ASHRAE Efficiency [Eq.(2.5)], Elbel Efficiency [Eq. (2.6)] and Exergy Efficiency [Eq. (2.8)] for the $R134a$ ejector at (a) operating conditions OP1, OP2 and OP3 and (b) inlet conditions OP2 with varying outlet pressure ($T_{out}^{sat} = 26\,°C$, $28\,°C$, $32\,°C$, $33\,°C$ and $35\,°C$).

Loss coefficients

Loss coefficients are often used to quantify the effects of irreversibilities generated by friction, mixing and shock waves on the performance of the ejector [Liu and Groll, 2013]. For single-phase $R134a$ ejectors, Untea *et al.* [2013] presented the following parameters:

$$\Phi_1 = \frac{u_{NXP}}{\sqrt{2(h_{prim} - h_{NXP})}}, \tag{5.2a}$$

$$\Phi_2 = \frac{u_{\text{end of CAS}}(1+\omega_r)}{u_{NXP}}, \tag{5.2b}$$

$$\Phi_3 = \frac{h_{out}^{is,\text{at end of CAS}} - h_{\text{end of CAS}}}{h_{out} - h_{\text{end of CAS}}}, \tag{5.2c}$$

which respectively quantify isentropic losses through the motive nozzle expansion, momentum losses in the mixing chamber and isentropic losses in the diffuser. Figures 5.13(a) and (b) depict the values of these coefficients respectively for operating conditions OP1-3 and for inlet conditions OP2 at varying outlet pressure. $\Phi_1 \sim 1$ for all cases, indicating that friction losses in the motive nozzle are almost negligible independently of the primary inlet conditions. Through the CAS, two important sources of losses take place: mixing and shock waves, which lead to the low Φ_2 values (in average 0.635). In terms of the variation with the operating conditions, Figures 5.13(a) and (b) show inverse tendencies in Φ_2 with p_{out}/p_{prim}, which are explained by the dependence on the entrainment ratio: from OP1 to OP3, the reduction in ω_r is the most important factor affecting Φ_2, whereas at fixed inlet conditions [Figure 5.13(b)] the entrainment ratio is constant but an important reduction in the axial velocity at the end of the CAS was observed (about 57% from $T_{out}^{sat} = 26\,°\text{C}$ to $T_{out}^{sat} = 33\,°\text{C}$). This also explains the abnormally high Φ_2 value at $T_{out}^{sat} = 26\,°\text{C}$, where the bulk of the flow is supersonic at the end of the CAS (Figure 5.6). Coefficient Φ_3 relates the ideal to actual specific enthalpy change through the diffuser. It reduces from OP1 to OP3 and from $T_{out}^{sat} = 26\,°\text{C}$ to $T_{out}^{sat} = 34\,°\text{C}$ in the same direction as the diffuser compression ratio.

5.1.5 Exergy analysis

Figure 5.14 shows the exergy evolution through the CAS and diffuser of the ejector for various operating conditions. These values have been determined by performing area-weighted averages at successive cross-sections along the domain. In general, all profiles present a very similar shape, with the greatest exergy destruction occurring along the CAS

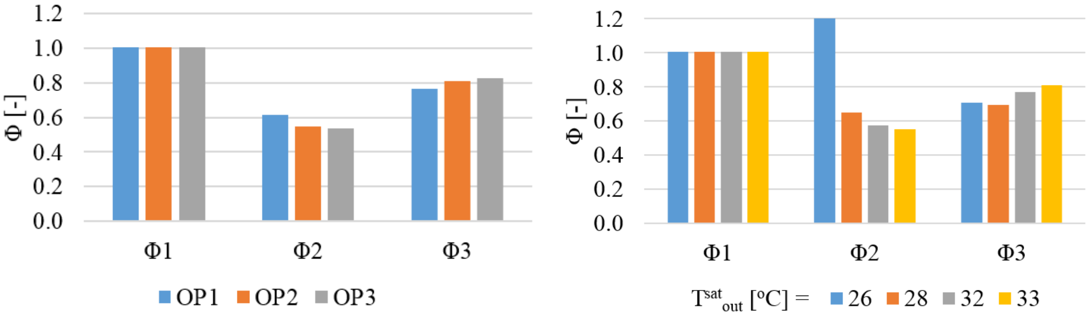

(a) (b)

Figure 5.13 Losses coefficients Φ_1, Φ_2 and Φ_3 [Untea *et al.*, 2013] for the $R134a$ ejector at (a) operating conditions OP1, OP2 and OP3 and (b) inlet conditions OP2 with varying outlet pressure ($T_{out}^{sat} = 26\,°\mathrm{C}$, $28\,°\mathrm{C}$, $32\,°\mathrm{C}$ and $33\,°\mathrm{C}$).

and first half of the diffuser. In terms of the dependence on inlet conditions, Figure 5.14(a) shows a vertical translation of the exergy profile with the primary inlet conditions, which explains the apparent invariance of the exergy efficiency for conditions OP1, OP2 and OP3 (56%, 55% and 58% respectively). Conversely, at fixed inlet conditions [Figure 5.14(b)], the input exergy is constant but the outlet exergy augments with the outlet pressure and temperature.

Exergy destruction (ξ) and Ma profiles through the ejector are shown in Figures 5.15 to 5.17 for operating conditions OP1 to OP3 (the values correspond to area-weighted averages at successive cross-sections). The exergy destruction index is defined in such a way that $\xi = 0$ at the start of the domain and $\xi = 1$ at the end, indicating the importance of each region on the total exergy destroyed [Eq. (2.10)]. For the three assessed operating conditions the profiles are very alike, with notable differences only on the maximum Ma number at the CAS and the location of the shock train. Most of the exergy losses are located in two regions: between the NXP and the start of the CAS (Section 1) where exergy is destroyed as the inflows start interacting and mixing, and through the second half of the CAS (Section 2) at the shock train location as revealed by the sudden reduction in Ma. At the start of the diffuser there is a mild although still noticeable increase in exergy destruction, probably due to the persistence of the sonic region around the centre of the ejector (Figure 5.3). At $x = 0.08\,\mathrm{m}$, ξ is equal to 0.997 meaning the greatest part of the exergy destruction through the domain has already occurred. Beyond this point, flow friction is the only noticeable source of losses. An accounting of the contribution of sections 1 and 2 to the total exergy destruction is shown in Figure 5.18 for all cases. In general, between 50% and 70% of the losses incurred through the device are generated in these two sections, with a slight prominence of section 2 for most cases. No clear tendency is seen with regards to varying inlet conditions [Figure 5.18(a)]. At fixed inlet conditions, the contributions of both sections augment with the outlet pressure.

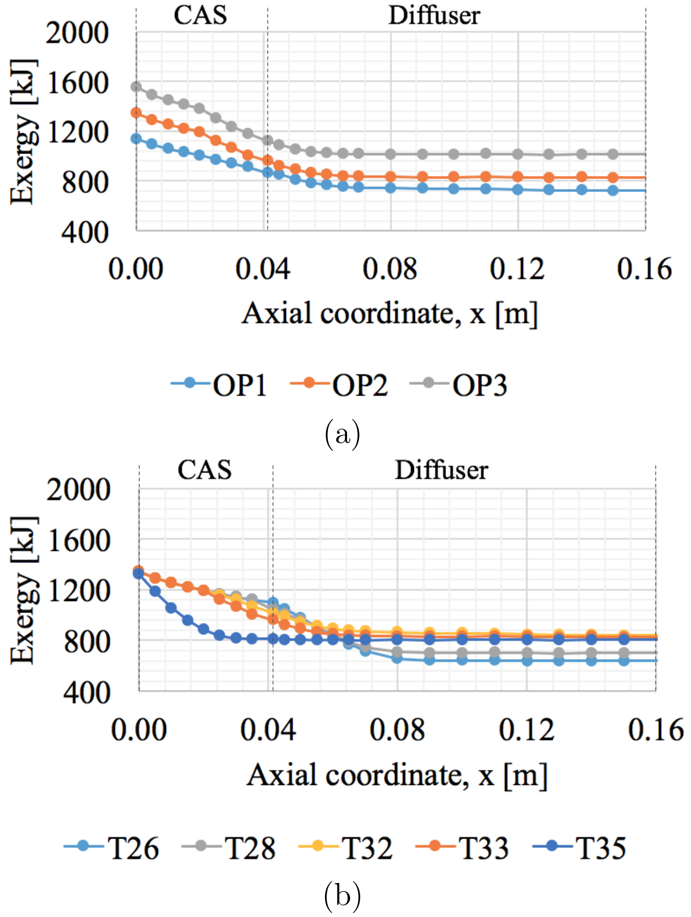

Figure 5.14 Exergy profiles through the CAS and diffuser of the ejector at (a) operating conditions OP1, OP2 and OP3 and (b) inlet conditions OP2 with varying outlet pressure ($T_{out}^{sat} = 26\,°C$, $28\,°C$, $32\,°C$ and $33\,°C$).

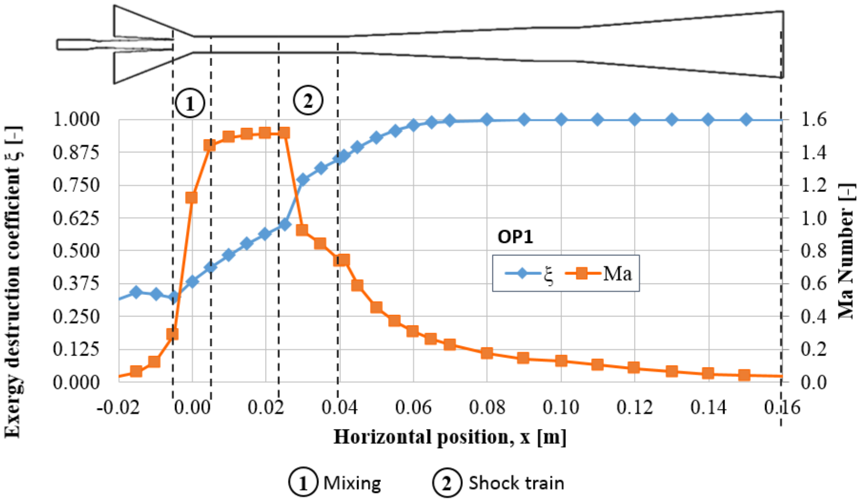

Figure 5.15 Exergy destruction and Ma profiles through the ejector at operating conditions OP1.

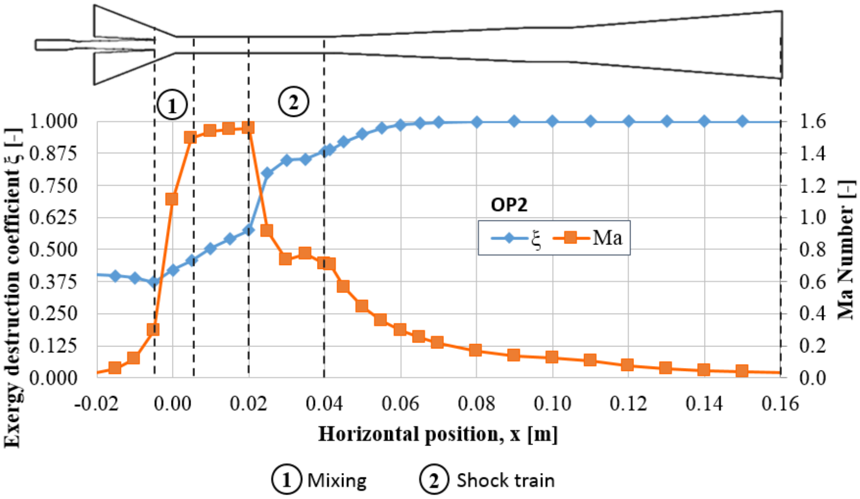

Figure 5.16 Exergy destruction and Ma profiles through the ejector at operating conditions OP2.

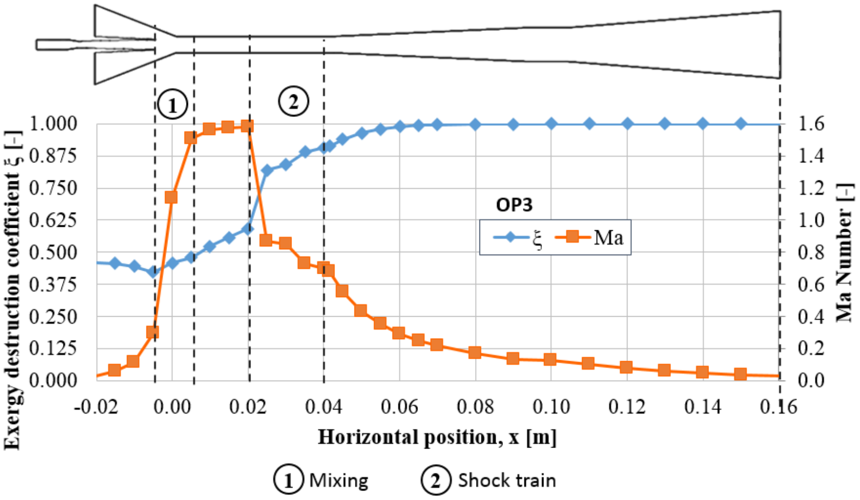

Figure 5.17 Exergy destruction and Ma profiles through the ejector at operating conditions OP3.

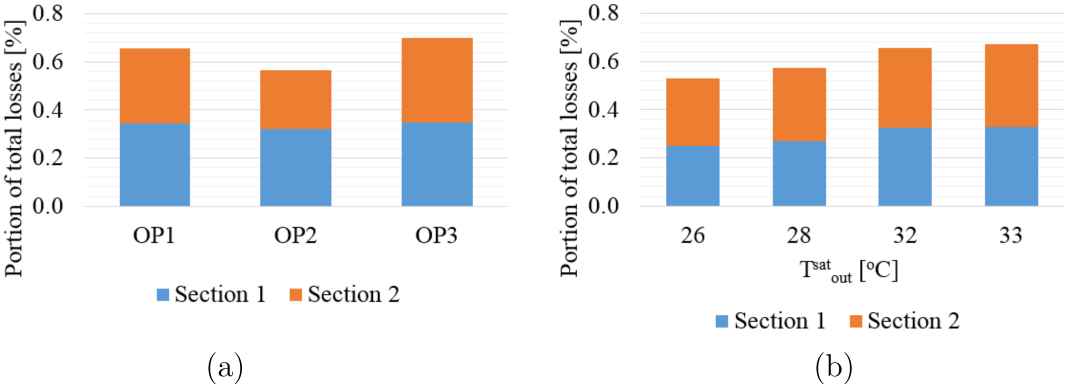

(a) (b)

Figure 5.18 Contribution of Mixing (Section 1) and Shocks (Section 2) losses to the total exergy destroyed through the ejector at (a) operating conditions OP1, OP2 and OP3 and (b) inlet conditions OP2 with varying outlet pressure (T_{out}^{sat} = 26 °C, 28 °C, 32 °C and 33 °C).

5.2 Drop-in replacement by HFO refrigerants

The effect of using the novel refrigerants $R1234yf$ and $R1234ze(E)$ instead of $R134a$ as working fluids for the ejector at similar operating conditions has been carried out, with particular emphasis on the differences in entrainment ratio, losses coefficients and net effect over the performance of a HDRC. Hydrofluorocarbons (HFCs), such as $R134a$ and $R245fa$, are a family of refrigerants commonly used in ejector based refrigeration systems as they are known for being stable, non-toxic, non-flammable and with zero Ozone Depletion Potential (ODP). Nonetheless, policies have been started to fade out their use, given their elevated Global Warming Potential (GWP) [Parliament and Council, 2014]. In recent years, a series of synthetic refrigerants known as hydrofluoroolefins (HFOs) have been specifically developed to mimic the thermodynamic and transport properties of common HFCs. Two particularly interesting members of this family are $R1234yf$ and $R1234ze(E)$, which have zero ODP, very low GDP and a much shorter lifetime in the atmosphere. Studies on vapour compression refrigeration cycles have shown that $R1234yf$ offers no significant detriment in energy efficiency and a lower exergy destruction rate [Ozgur *et al.*, 2012]. Similarly theoretical studies suggest $R1234ze(E)$ also presents a good low-GWP alternative to $R134a$ albeit with some basic system modifications [Ansari *et al.*, 2013]. The reader can refer to the recent works of Wang [2014] and Mota-Babiloni *et al.* [2016] for in-depth reviews of heat-pumps, refrigeration and air-conditioning systems working respectively with $R1234yf$ and $R1234ze(E)$.

As it is shown in Table 5.1, all three fluids have very similar properties. In particular the molecular weight and critical point are very close, which to some extent define their general behaviour. A notable difference exists in the saturation pressure of $R1234ze(E)$ at 20 °C and 80 °C, which is much lower than that for $R134a$ and $R1234yf$. This affects its applicability as pure gas in the single-phase ejector assessed in this section. Therefore, two options were considered in the definition of the operating conditions for drop-in fluid replacement: (i) to keep the operating conditions OP1, OP2 and OP3 unchanged (limiting the study to the use of $R134a$ and $R1234yf$), and (ii) to define the operating points OP1', OP2' and OP3' by adjusting p_{prim} to ensure a 10 °C superheat while maintaining the same T_{prim} and pressure ratios $p_{sec}/p_{critical}$ and $p_{out}/p_{critical}$ of the baseline cases with $R134a$. The resulting operating conditions OP1', OP2' and OP3' for $R1234yf$ and $R1234ze(E)$ are shown in Table 5.2. Operating conditions OP1, OP2 and OP3 are shown in Table 3.2.

working fluid	$R134a$	$R1234yf$	$R1234ze(E)$
Name	1,1,1,2 tetrafluoroethane	2,3,3,3 tetrafluoroprop-1-ene	1,3,3,3 tetrafluoroprop-1-ene
Chemical formula	CF_3CFH_2	$CH_2 = CFCF_3$	$CF_3CH = CHF$
Molecular weight [g/mol]	102.03	114.04	114.04
Toxicity class (Ashrae Std 34)	A (low)	A (low)	A (low)
Flammability (Ashrae Std 34)	A1 (non flammable)	A2L (low flammability)	A2L (low flammability)
GWP_{100}	1430	4	4
Ozone Depletion Potential (ODP)	0	0	0
Lifetime in the atmosphere (year)	13	0.03	0.05
Normal boiling point [°C]	26.1	29.4	18.95
Saturated vapor pressure at 20 °C [kPa]	774.3	794.3	419.2
Saturated vapor pressure at 80 °C [kPa]	2635	2519	2007
Critical temperature [°C]	101.1	94.7	109.4
Critical pressure [MPa]	4.059	3.38	3.635
Density [kg/m^3] at 30°C			
Liquid phase	1187	1075	1146
Vapor phase	37.54	44	30.6
Heat capacity C_p [kJ/kg/K] at 30°C			
Liquid phase	1.446	1.379	1.383
Vapor phase	1.065	1.11	0.9822
Thermal conductivity k [W/m/K] at 30°C			
Liquid phase	0.079	0.0631	0.0725
Vapor phase	0.01433	0.01143	0.014
Dynamic viscosity μ [µPa/s] at 30°C			
Liquid phase	185.8	152	188
Vapor phase	12.04	12.86	12.5
Latent heat of vaporization at 30 °C [kJ/kg/s]	173.1	140.1	162.9

Table 5.1 Thermodynamic properties of R134a, R1234yf and R1234ze(E). GWP_{100} is the Global Warming Potential over a 100 year integration horizon.

Table 5.2 Operating conditions for the ejector adjusted for the HFO refrigerants $R1234yf$ and $R1234ze(E)$, keeping the same primary inlet temperature, pressure ratios and superheat as in the experiments of García del Valle *et al.* [2014].

Operation Point	T_p [degreeCelsius]	**R1234yf** P_p[kPa]	P_s[kPa]	P_{out}[kPa]	**R1234ze(E)** P_p[kPa]	P_s[kPa]	P_{out}[kPa]
1’	89.35	2487.2	396.9	724.9	1980.5	316.1	577.2
2’	94.35	2753.9	395.3	788.0	2203.5	316.2	630.5
3’	99.15	3028.8	393.9	852.3	2432.5	316.3	684.5

5.2.1 Effect on ejector entrainment ratio

Table 5.3 shows the variation in primary and secondary mass flows and entrainment ratio when using $R134a$, $R1234yf$ and $R1234ze(E)$. Regarding operating conditions OP1-3, the change from $R134a$ to $R1234yf$ implies a slight decrease in terms of ω_r of 4.0% to 6.9%. This difference is a consequence of a noticeable increase in $\dot{m}_{prim}$ and a somewhat mild increase in $\dot{m}_{sec}$ when changing to $R1234yf$. Further analyses using the models developed in this section, published in Fang *et al.* [2017], have shown that the entrainment ratio and shock structure are practically independent to changes in the composition when working with $R134a$-$R1234yf$ and $R134a$-$R1234ze(E)$ mixtures at operating conditions OP1 to OP3. Concerning OP1’-3’, a reduction in ω_r is also observed with $R1234yf$ although at a lower degree. Conversely, at these conditions, using $R1234ze(E)$ leads to an average increase in entrainment ratio of about 3.5% relative to the case with $R134a$, although with important reductions in the mass flow rates through the ejector, *e.g.*: relative to conditions OP1’ with $R134a$, $\dot{m}_{prim}$ and $\dot{m}_{sec}$ decrease respectively by 22.1% and 20.9% when using

$R1234ze(E)$. The variations in the ejector performance curve are further appreciated in Figure 5.19, which depicts the ω_r versus compression ratio for the ejector at conditions OP2 (working with $R134a$ and $R1234yf$) and OP2' (working with $R1234yf$ and $R1234ze(E)$). While maintaining the same operating conditions, the change to $R1234yf$ reduces the entrainment ratio but increases the compression ratio in about 0.1 points. Conversely, at conditions OP2', an important reduction in the double-choke limiting compression ratio (p_{lim}/p_{sec})is observed, in particular for the case with $R1234ze(E)$, with the maximum expected compression ratio at double-choke regime is about 1.56, *i.e.*: 23% lower than the baseline case with $R134a$. The reduction in the maximum double-choke compressing capacity is not so drastic with $R1234yf$ in this case, as it reduces to 1.92, just 5% lower than when using $R134a$.

Table 5.3 Comparison of primary and secondary mass flows and entrainment ratio for $R134a$, $R1234yf$ and $R1234ze(E)$ at the operating conditions of Table 5.2

	OP1	OP2	OP3	OP1'	OP2'	OP3'
			$\dot{m}_{prim}$[kg/s]			
$R134a$	0.0335	0.0375	0.0417	0.0335	0.0375	0.0417
$R1234yf$	0.0357	0.0401	0.045	0.0338	0.0376	0.0417
$R1234ze(E)$	-	-	-	0.0261	0.0292	0.0323
			$\dot{m}_{sec}$[kg/s]			
$R134a$	0.0172	0.0164	0.0158	0.0172	0.0164	0.0158
$R1234yf$	0.0176	0.0167	0.016	0.017	0.0162	0.0157
$R1234ze(E)$	-	-	-	0.0136	0.013	0.0126
			ω_r [-]			
$R134a$	0.5126	0.4364	0.3804	0.5126	0.4364	0.3804
$R1234yf$	0.4919	0.4165	0.3543	0.5044	0.4297	0.3752
$R1234ze(E)$	-	-	-	0.5201	0.4442	0.3907

Given the similarity in structure and properties between $R134a$, $R1234yf$ and $R1234ze(E)$, it is expected that the general internal flow structure shows little dependence on the working fluid. This is verified in Figure 5.20 which depicts the magnitude of the density gradient ($\nabla\rho$) for the ejector at operating conditions OP2 using $R134a$-$R1234yf$ mixtures at the proportions $[20\% - 80\%]$ and $[80\% - 20\%]$. Density gradient contours enable to visualize more easily the shock structures along the domain. Other than slight variations in the motive jet core length, the contours are essentially the same for both mixtures. In particular, the oblique shocks generating at the primary nozzle tip, which reveal a slightly over-expanded shock, are mirrored between both cases, with negligible differences in the propagation angles and reflection locations through the centreline. Beyond this region, the

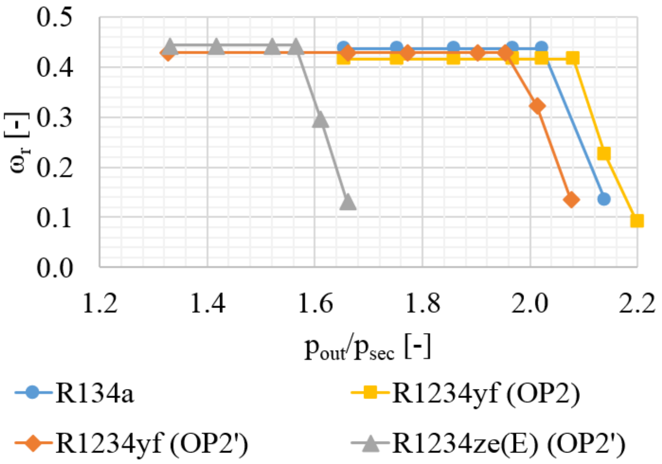

Figure 5.19 Curves of the entrainment versus compression ratios for the ejector at operating conditions OP2' with $R134a$, $R1234yf$ and $R1234ze(E)$.

shock starts a little earlier in the case with 20% $R134a$ and no differences are appreciated in the length of both shock trains.

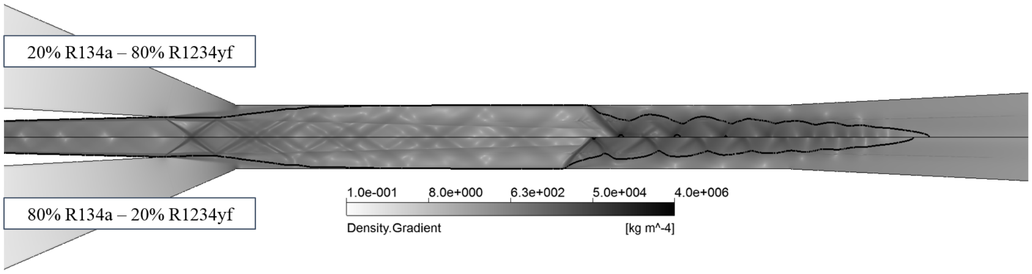

Figure 5.20 Comparison of the density gradient through the ejector at operating conditions OP2 with mixtures of 20% $R134a$ - 80% $R1234yf$ and 80% $R134a$ - 20% $R1234yf$.

5.2.2 Effect on losses coefficients

Figure 5.21 presents the three friction coefficients defined in Eqs. 5.2 [Untea *et al.*, 2013] for the ejector with the three working fluids at operating conditions OP2 and OP2'. Similar results were observed for the other assessed conditions and are not shown here. The friction losses are almost negligible in the primary nozzle such that $\Phi_1 \geq 0.96$ in all cases. Similarly, friction losses in the diffuser are within the typical range of these devices, with Φ_3 between 0.822 and 0.995. Although $R134a$ offers the best performance in the primary nozzle, it is outperformed by both HFOs at the mixing and diffuser sections, with $R1234yf$ resulting in the highest Φ_2 and Φ_3.

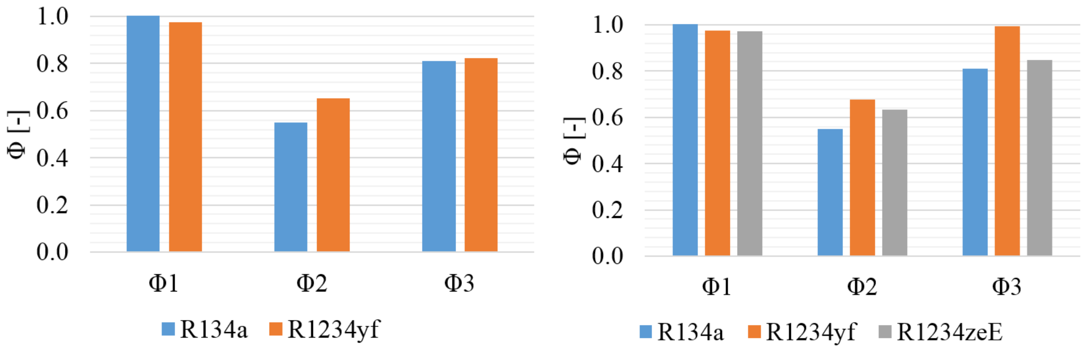

(a) (b)

Figure 5.21 Losses coefficients Φ_1, Φ_2 and Φ_3 [Untea *et al.*, 2013] for the ejector with (a) $R134a$ and $R1234yf$ at operating conditions OP1, OP2 and OP3, and (b) with $R134a$, $R1234yf$ and $R1234ze(E)$ at operating conditions OP1', OP2' and OP3'.

5.2.3 Effect on HDRC performance

With the ejector global behaviour fully characterized in the previous sections, it is possible to estimate the impact of drop-in fluid replacement on the performance of a Heat Driven Refrigeration Cycle (HDRC). Calculations are based on energy and mass balances along the different components of the HDRC as depicted in Figure 2.4. The cooling load ($\dot{Q}_{load}$), required heat input ($\dot{Q}_{req}$) and coefficient of performance (COP) are defined as follows:

$$\dot{Q}_{load} = \dot{Q}_{evaporator} = \dot{m}_{sec}\,(h_6 - h_5) \tag{5.3a}$$

$$\dot{Q}_{req} = \dot{Q}_{generator} = \dot{m}_{prim}\,(h_1 - h_4) \tag{5.3b}$$

$$COP = \frac{\dot{Q}_{evaporator}}{\dot{Q}_{generator} + \dot{W}_{pump}} = \omega_r \frac{h_6 - h_5}{h_1 - h_3} \tag{5.3c}$$

where $\dot{Q}_{evaporator}$ and $\dot{Q}_{generator}$ are the heat inputs to the evaporator and generator and $\dot{W}_{pump}$ is the pumping power. It was assumed that there are no pressure losses along the stream lines, the valve is isenthalpic and the pump has an isentropic efficiency of 90%. The calculation algorithm, which was implemented in Matlab, starts by fixing the saturation pressures or temperatures at the evaporator and generator and the respective superheat. This provided the entry conditions to the CFD model, from which the entrainment ratio, mass flow rates and condenser inlet temperature are obtained. The thermodynamic properties were calculated using the NIST REFPROP Database [NIST, 2010].

Table 5.2 shows the effect on HDRC performance of changing the working fluid from $R134a$ to $R1234yf$ and $R1234ze(E)$. Regarding operating conditions OP1 to OP3, despite the slight increase in entrainment ratio observed for $R1234yf$, the calculated COP and cooling load diminish in average by 9.6% and 17.5% respectively relative to the cases with $R134a$. This noticeable detriment in the cycle performance can be explained using the pressure-enthalpy diagram of Figure 5.22, which shows the resulting cycles with $R134a$ and $R1234yf$ at operating conditions OP1. The specific cooling capacity ($\dot{Q}_{load}/\dot{m}_{sec}$) is denoted by the process 4-1 for $R134a$ and 4^*-1^* for $R1234yf$. The former being longer than the latter, the system with $R1234yf$ has a much lower cooling capacity unless the secondary mass flow is increased, which is not the case as shown in Table 5.3. Furthermore, lines 5-6 and 5^*-6^* represent the specific required driving heat input ($\dot{Q}_{req}/\dot{m}_{prim}$) for $R134a$ and $R1234yf$ respectively. Although $\dot{Q}_{req}/\dot{m}_{prim}$ is much higher for the case with $R134a$, the excess in specific heat input required between the cycles $(1 - 1^*)$ is less than the difference in cooling gain $(6 - 6^*)$. On top of that, the primary mass flow rate is greater in the case with $R1234yf$, thus the required driving energy increases for this cycle relative to the case with $R134a$. The combination of the reduced cooling load and increase required heat input translate into a poorer COP.

Through conditions OP1' to OP3' the difference in COP is similar between $R134a$ and $R1234yf$ although the cooling capacity worsens. At these conditions, $R1234ze(E)$ drop-in replacement would imply an average decrease of only 4.2% in terms of COP, although the cooling capacity would diminish by 26.6%. The corresponding pressure-enthalpy diagram for the HDRC system at operating conditions OP2' is shown in Figure 5.23 for the alternatives using the three assessed fluids. Analogous to the diagram of Figure 5.22, the specific heat input requirement and cooling load for the cycle with $R1234ze(E)$ are represented respectively by lines $4'$-$1'$ and $5'$-$6'$. In this case, the term $\dot{Q}_{load}/\dot{m}_{prim}$ is lower for the case with $R1234ze(E)$, which added to a smaller $\dot{m}_{sec}$ leads to a reduced cooling capacity relative to the case with $R134a$.

Table 5.4 Variation in COP and Cooling Capacity of the refrigeration system working with $R134a$, $R1234yf$ and $R1234ze(E)$ at the operating conditions of Table 5.2.

	System COP [–]			Cooling Capacity [kW]		
	R134a	R1234yf	R1234ze(E)	R134a	R1234yf	R1234ze(E)
OP1	0.432	0.395 (-8.6 %)	-	2967.8	2480.8 (-16.4 %)	-
OP2	0.364	0.331 (-9.1 %)	-	2753.1	2282.8 (-17.1 %)	-
OP3	0.315	0.280 (-11.1 %)	-	2599.9	2108.5 (-18.9 %)	-
OP1'	0.432	0.392 (-9.3 %)	0.414 (-4.2 %)	2967.8	2399.5 (-19.1 %)	2175.3 (-26.7 %)
OP2'	0.364	0.329 (-9.6 %)	0.348 (-4.4 %)	2753.1	2206.6 (-19.9 %)	2017.2 (-26.7 %)
OP3'	0.315	0.284 (-9.8 %)	0.302 (-4.1 %)	2599.9	2069.2 (-20.4 %)	1913.6 (-26.4 %)

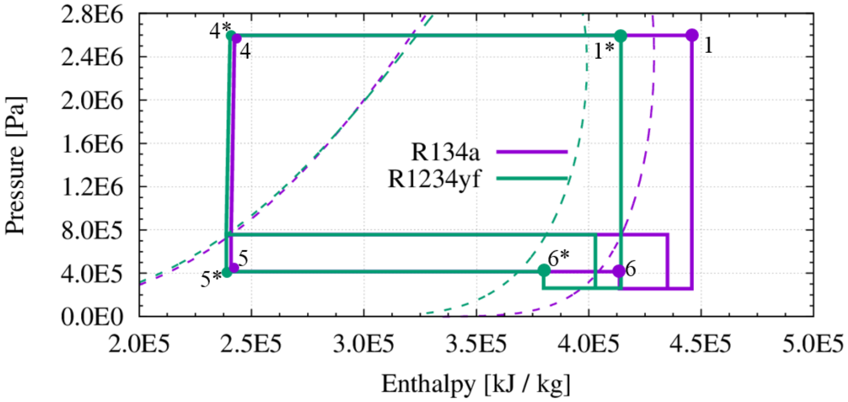

Figure 5.22 Pressure - enthalpy diagrams of the ejector heat driven refrigeration cycles with $R134a$ and $R1234yf$ for the conditions corresponding to Operating Point 1 of Table 3.2.

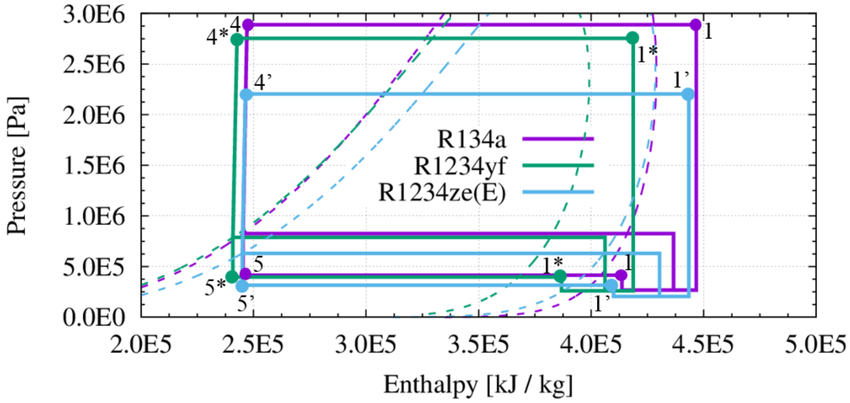

Figure 5.23 Pressure - enthalpy diagrams of the ejector heat driven refrigeration cycles with $R134a$, $R1234yf$ and $R1234ze(E)$ for the conditions corresponding to Operating Point 1 of Table 3.2.

5.3 Comparisons of CFD and thermodynamic models

This section presents a systematic comparison of the performance prediction of an air supersonic ejector using the CFD model described in Chapter 3 and the thermodynamic model of Galanis and Sorin [2016]. Comparisons are made in terms of global ejector performance, shock start location assumptions and flow similarity.

5.3.1 The thermodynamic model of Galanis and Sorin [2016]

The thermodynamic model of Galanis and Sorin [2016] solves integral conservation balances of mass, momentum and energy over the characteristic sections of the ejector as depicted in Figure 5.24 with the following main assumptions: one dimensional flow of a perfect gas; the primary flow is always choked; constant pressure mixing; adiabatic walls; full mixing is achieved at position 5 and a normal shock (delimited by a and b) occurs in the CAS between positions 5 and 6. Irreversibilities through both inlets and the diffuser are accounted for using polytropic efficiencies which, contrary to the commonly used isentropic coefficients, better adjust to changes in operating conditions. Through the CAS, a mixing efficiency is introduced to account for mixing and friction losses. Although the model has been developed principally for determining the optimal geometry delivering a desired entrainment ratio and inlet conditions, off-design operation can also be calculated for a given geometry by assuming that the limiting point p_{lim} corresponds to the conditions with minimum entropy generation. The model has been validated against the data of Huang *et al.* [1999]. As a consequence of the perfect gas assumption, analytical relationships for the ejector performance can be deducted in terms of dimensionless quantities. In this study, the primary throat diameter D_{p2} and secondary inlet conditions p_{s0} and T_{s0} have been chosen for adimensionalization such that, for a family of geometrically similar ejectors, performance curves are collapsed onto a single curve depending on the dimensionless quantities ω_r, p_{lim}, p_{p0}/p_{s0} and T_{p0}/T_{s0}.

5.3.2 CFD Model

A CFD model of the ejector has been built based on the numerical setup described in Chapter 3, using a density based solver and the $k-\omega$ SST model. Given the main interest of this study is a global outlook of the ejector behaviour over a wide range of operating conditions, the high-Reynolds version of the turbulence model has been preferred as it is less computationally expensive in comparison with the low-Reynolds approach. Computations have been performed with both the perfect gas model and REFPROP

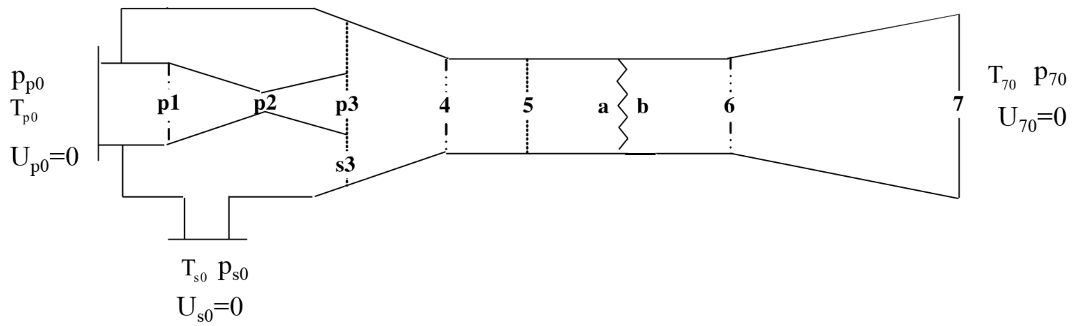

Figure 5.24 Schematic representation of the ejector geometry and the location of characteristic positions.

database for air. For cases using the former, transport properties are assumed constant: $\lambda = 0.0242\,\mathrm{W/mK}$ and $\mu = 1.7894 \times 10^{-5}\,\mathrm{Pa\,s}$. For the latter, all flow properties are determined using the formulation of Lemmon *et al.* [2000], valid in the range $60\,\mathrm{K} \leq T \leq 2000\,\mathrm{K}$ and $p \leq 2000\,\mathrm{MPa}$.

5.3.3 Ejector geometry and operating conditions

Calculations have been performed for the baseline case $p_{p0}/p_{s0} = 100$, $T_{p0}/T_{s0} = 1.6$, ω_r and polytropic and mixing efficiencies equal to 0.9. The selected efficiency values lead to calculated isentropic and mixing efficiencies in the range 0.7 to 1.0, which agrees with the ranges determined by Liu and Groll [2013] for a wide range of geometries and operating conditions. The ejector geometry and double-choke limit were determined using the thermodynamic model at the baseline conditions, resulting in $p_{lim}/p_{s0} = 5.85$ and the dimensions summarized in Table 5.5 relative to the primary throat diameter D_{p2}. In absolute terms, the geometrical similarity of two ejector sizes, based on $D_{p2} = 0.02\,\mathrm{m}$ and $0.06\,\mathrm{m}$, was verified by comparing performance and centreline p and Ma profiles. Similarly, the invariance with absolute inlet conditions values was assessed by comparing results at $p_{s0} = 50.663\,\mathrm{kPa}$, $101.325\,\mathrm{kPa}$ and $151.988\,\mathrm{kPa}$. In all cases $T_{s0} = 26.85\,°\mathrm{C}$.

Table 5.5 Ejector normalized dimensions for the baseline case. The subscripts reffer to the locations shown in Figure 5.24.

Diameters	**Value**	**Lengths**	**Value**
D_{p1}/D_{p2}	2.36	x_2/D_{p2}	3.85
D_{p3}/D_{p2}	3.69	x_3/D_{p2}	19.28
D_3/D_{p2}	5.43	x_4/D_{p2}	20.61
$D_4/D_{p2} = D_6/D_{p2}$	4.96	x_6/D_{p2}	96.14
D_7/D_{p2}	10.65	x_7/D_{p2}	111.10

5.3.4 Differences in global performance

Figure 5.25 shows a comparison of the predicted performance curves for the ejector with $p_{p0}/p_{s0} = 100$ ($p_{s0} = 101.325\,\mathrm{kPa}$) and $D_{p2} = 0.02\,\mathrm{m}$ using the thermodynamic and CFD models with perfect and real gas equations. The double-choke entrainment ratio calculated with the thermodynamic model is 0.20, in average this value is 25% above the entrainment ratio determined with the CFD model using the perfect gas ($\omega_r = 0.145$) and real gas ($\omega_r = 0.156$) approaches, which reflects the important simplifications and idealizations assumed in the construction of the thermodynamic model. In terms of the limiting pressure, the average difference between the thermodynamic and CFD models is about 5%, as $p_{lim}/p_{s0} = 5.85$, 6.2 and 6.1 according respectively to the thermodynamic, CFD - perfect gas and CFD - real gas models. It has been verified in previous studies that, for varying ratios p_{p0}/p_{s0}, the difference in ω_r between the thermodynamic and CFD - perfect gas approaches are practically invariant but the agreement in terms of p_{lim}/p_{s0} might be improved [Croquer *et al.*, 2016c]. Concerning both CFD models, the differences in ω_r and p_{lim}/p_{s0} are respectively of 7.9% and 1.6%, much lower than those observed in the benchmark study for $R134a$ (Section 3.5), which shows the air at these conditions behaves as an ideal gas, reinforcing the idea that the disagreement with the thermodynamic model stems from simplifications other than the perfect gas assumption.

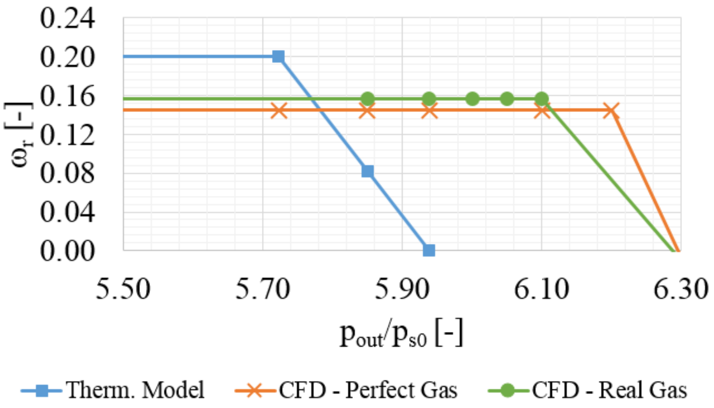

Figure 5.25 Ejector entrainment ratio versus compression ratio curves as predicted by the thermodynamic, CFD-perfect gas and CFD-real gas models, for $p_{p0}/p_{s0} = 100$, $p_{s0} = 101.325\,\mathrm{kPa}$ and $D_{p2} = 0.02\,\mathrm{m}$.

Flow properties at different internal locations

Figures 5.26 and 5.27 compare the values of p/p_{s0}, T/T_{s0} and Ma predicted by the three models at different locations within the ejector with $p_{p0}/p_{s0} = 100$, $p_{s0} = 101.325\,\mathrm{kPa}$ and $D_{p2} = 0.02\,\mathrm{m}$. The CFD values are area-weighted averages at each cross-section. Referring to Figure 5.26, which shows the results for double-choke regime ($p_{out}/p_{s0} =$

5.85), the agreement between the three models is rather good whatever the location, with indistinguishable differences between the CFD - perfect gas and CFD - real gas approaches. A variation of less than 10% between the models is observed at most of the positions. The biggest differences are in the prediction of the pressure and Mach number at cross-section $s3$, corresponding to the secondary flow just before meeting the primary jet, where the thermodynamic model predicts $p_{s3}/p_{s0} = 0.853$ and $Ma_{s3} = 0.930$ while the CFD - perfect gas model (resp. CFD - real gas model) predicts $p_{s3}/p_{s0} = 0.949$ and $Ma_{s3} = 0.596$ (resp. $p_{s3}/p_{s0} = 0.946$ and $Ma_{s3} = 0.609$). The conditions determined by the thermodynamic model at this location correspond to choked secondary flow, consistently with the on-design assumptions (the model of Galanis and Sorin [2016] establishes that the Mach number for irreversible compressible flow is less than unity at the throat). On the other hand, both CFD models indicate that choking of the secondary inflow occurs further downstream, in agreement with observations by Munday and Bagster [1977]. Similar results to those shown in Figure 5.26 have been obtained at other compression ratios up to the double-choke regime limit. For such cases, both streams are choked and therefore the outlet pressure does not influence the conditions at cross-sections $p1$, $p2$, $p3$, $s3$ and 4. Hence, the differences between the predictions of the two models at these cross-sections are independent of the compression ratio. Conversely, as p_{out}/p_{s0} increases, the predicted values of T/T_{s0} and p/p_{s0} at cross-sections 6 and 7 increase while the corresponding Ma values decrease. However, the agreement shows the same trend shown in Figure 5.26 here for the three models.

Figure 5.27 shows the results for single-choke operation with $\omega_r = 0.1$, $p_{out}/p_{s0} = 5.81$ and 6.15 for the thermodynamic and CFD models respectively. The agreement between the predictions of the three models remains generally good except at cross-section 4 where the thermodynamic model computes a subsonic flow while both CFD results indicated that it is in fact supersonic. The result in the case of the thermodynamic model is an usual assumption of this type of models, consistent with the one-dimensional modelling of the measured wall pressure [Huang *et al.*, 1985; Keenan, 1950], which shows a rapid pressure increase at the beginning of the converging duct. The corresponding results for the CFD models are a more realistic representation of these measurements and of the measured pressured along a supersonic air ejector axis [Bartosiewicz *et al.*, 2005].

Shock start location

Another important assumption introduced in the model of Galanis and Sorin [2016] is that the shock onset location varies linearly with the compression ratio. The shock train start location can be considered a limiting parameter for ejector operation since, at low

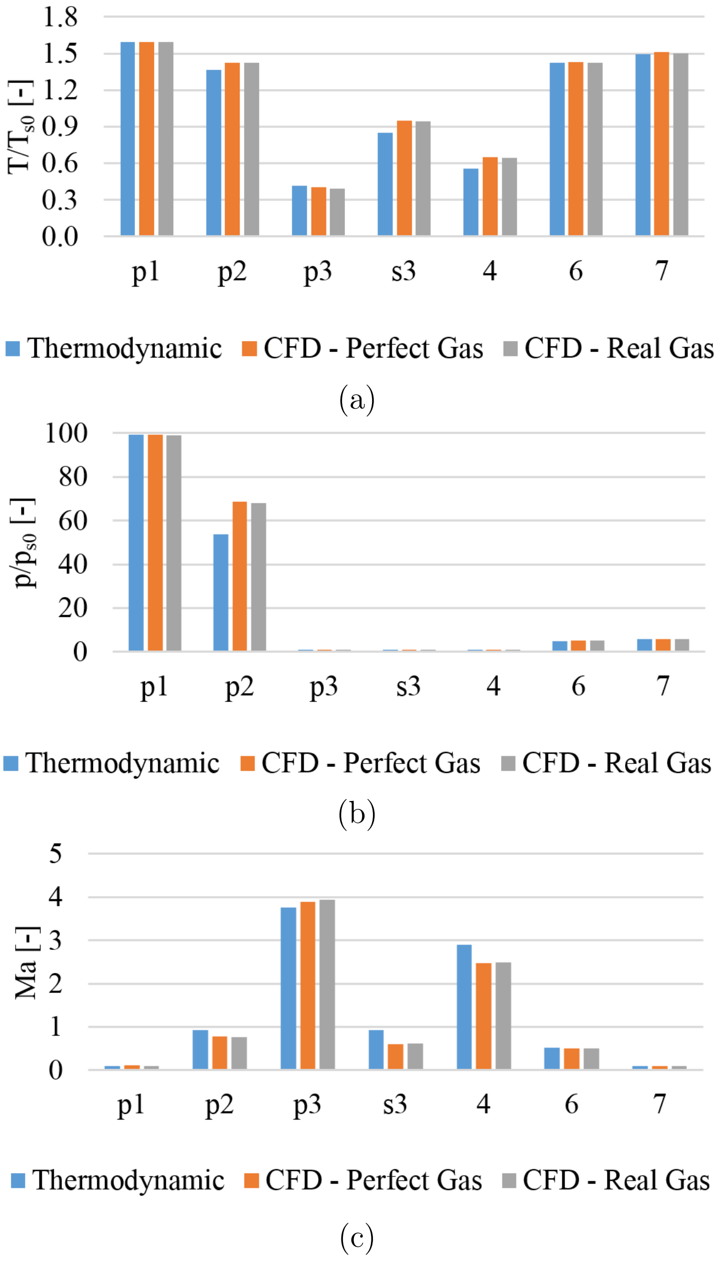

(a)

(b)

(c)

Figure 5.26 Comparisons of T/T_{s0}, p/p_{s0} and Ma at diferent axial locations for double-choke conditions ($p_{out}/p_{so} = 5.939$). Results obtained for $D_{p2} = 0.02\,\mathrm{m}$, $p_{p0}/p_{s0} = 100$ and $p_{s0} = 101.325\,\mathrm{kPa}$.

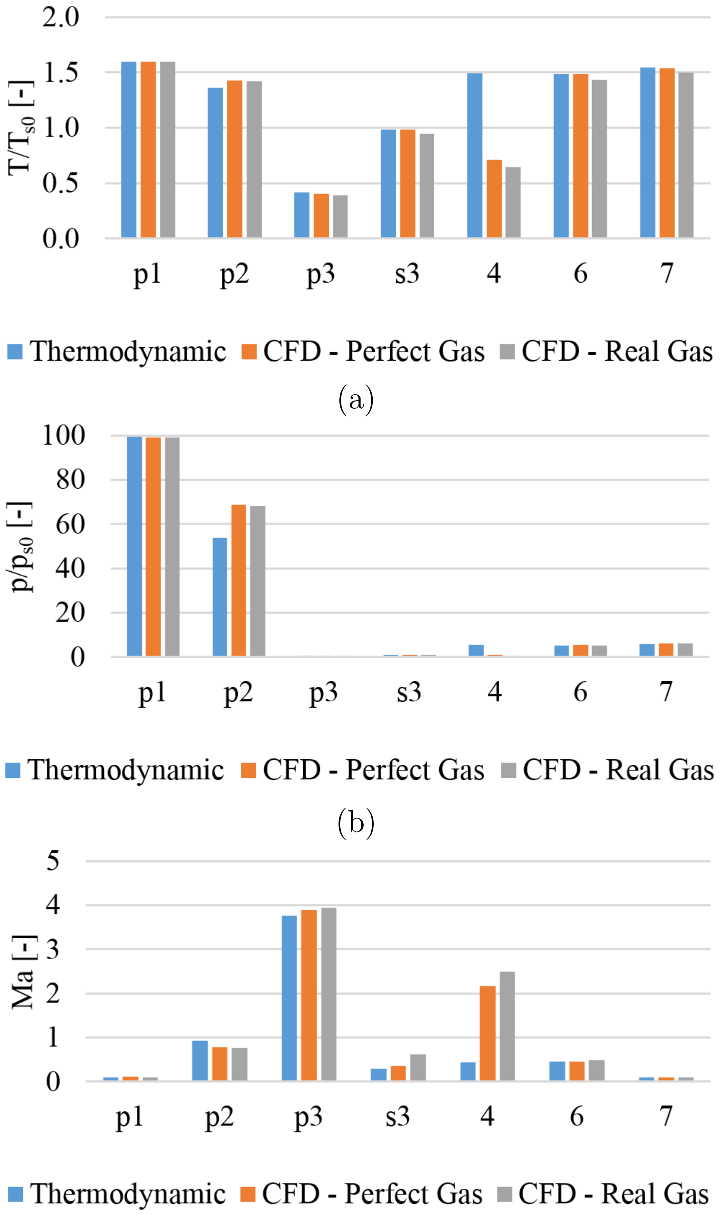

(a)

(b)

(c)

Figure 5.27 Comparisons of T/T_{s0}, p/p_{s0} and Ma at different axial locations for single-choke conditions ($p_{out}/p_{so} = 5.81$ for the thermodynamic model and 6.15 for both CFD models). Results obtained for $D_{p2} = 0.02\,\mathrm{m}$, $p_{p0}/p_{s0} = 100$ and $p_{s0} = 101.325\,\mathrm{kPa}$.

expansion ratios, the flow in the diffuser might be supersonic which hinders the diffuser performance. The validity of the linear variation assumption is assessed in Figure 5.28 where the start of the shock train in the CAS has been plotted against p_{out}/p_{s0} for the ejector with $D_{p2} = 0.02\,\mathrm{m}$ and $p_{s0} = 101.325\,\mathrm{kPa}$, using the results from the thermodynamic and CFD models. A linear variation is observed along the double-choke regime for all models, nonetheless while the thermodynamic model predicts that the shock train varies within the limits of the CAS ($96.1 \geq x/D_{p2} \geq 20.6$) for compression ratios in the range $4.14 \leq p_{out}/p_{s0} \leq 5.85$, the RANS models predict that the shock train reaches the end of the CAS at $p_{out}/p_{s0} = 2$, irrespective of the gas properties model. Similarly, both RANS models determine that the shock train starts as early as $x/D_{p2} \sim 50$ at the limiting condition. This difference with the thermodynamic model results from the actual motive jet structure, which even in single-choke conditions, extends into the start of the CAS.

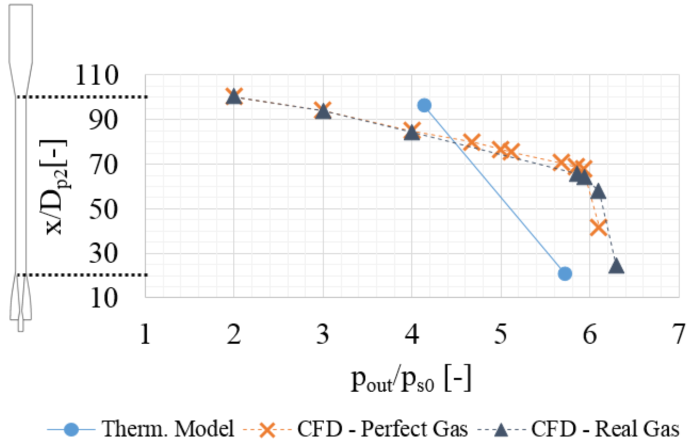

Figure 5.28 Variation in shock start position versus compression ratio as predicted by the thermodynamic, CFD-perfect gas and CFD-real gas models, for $p_{p0}/p_{s0} = 100$, $p_{s0} = 101.325\,\mathrm{kPa}$ and $D_{p2} = 0.02\,\mathrm{m}$.

5.3.5 Similarity of the flow domain

The previous results suggest that, at the assessed operating conditions, air behaves much like an ideal gas. This is verified in Figure 5.29 which depicts the compressibility factor determined using the CFD - real gas model for $p_{out}/p_{s0} = 5.85$, $p_{p0}/p_{s0} = 100$, $ps0 = 101.325kPa$ and $D_{p2} = 0.02\,\mathrm{m}$. Results for all other cases showed no differences, with $0.97 \leq Z \leq 1$. This implies that the flow adimensionalization introduced in the model of Galanis and Sorin [2016], which has been verified in CFD computations using the perfect gas model [Croquer *et al.*, 2016c], should extend to the real gas approach. This is assessed in Figure 5.30 for variations in the secondary inlet total pressure value

($p_{s0} = 50.663\,\text{kPa}$, $101.325\,\text{kPa}$ and $155.988\,\text{kPa}$), and in Figure 5.31 for two primary nozzle throat diameters $D_{p2} = 0.02\,\text{m}$ and $0.06\,\text{m}$. In terms of the actual secondary inlet pressure value, global performance is practically invariant except at $p_{s0} = 101.325\,\text{kPa}$ where the real gas model predicts a 7% higher double-choke entrainment ratio and the perfect-gas model predicts a higher limiting pressure [Figure 5.30(a)]. Computations in the region close to p_{lim} are marked by important secondary mass flow rate oscillations, which might accentuate differences in the results among the different models. Nonetheless, the pressure centreline profiles shown in Figure 5.30(b) verify that the flow structure can be adimensionalized using the secondary inlet pressure and primary throat diameter at these operating conditions.

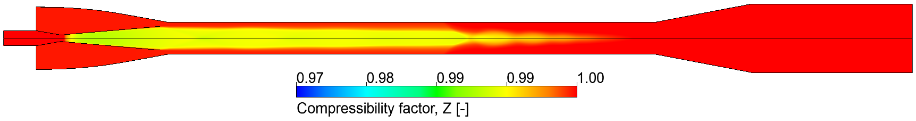

Figure 5.29 Compressibility factor through the ejector with real-gas. Results for $p_{out}/p_{s0} = 5.85$, $p_{p0}/p_{s0} = 100$, $ps0 = 101.325kPa$ and $D_{p2} = 0.02\,\text{m}$.

Concerning geometrical similitude, Figure 5.31 shows that differences persist in the baseline ($D_{p2} = 0.02\,\text{m}$) case between the perfect and real gas models. Nonetheless, differences in double-choke ω_r and p_{lim} are negligible between both models for an increase in D_{p2} to $0.06\,\text{m}$. Yet, the centreline profiles of Figure 5.31(b) show that, different from the observations with varying p_{s0}, inflow features do not completely scale with the ejector geometry, as the shock onset location moves towards the start of the CAS for the bigger ejector, independently of the chosen gas model.

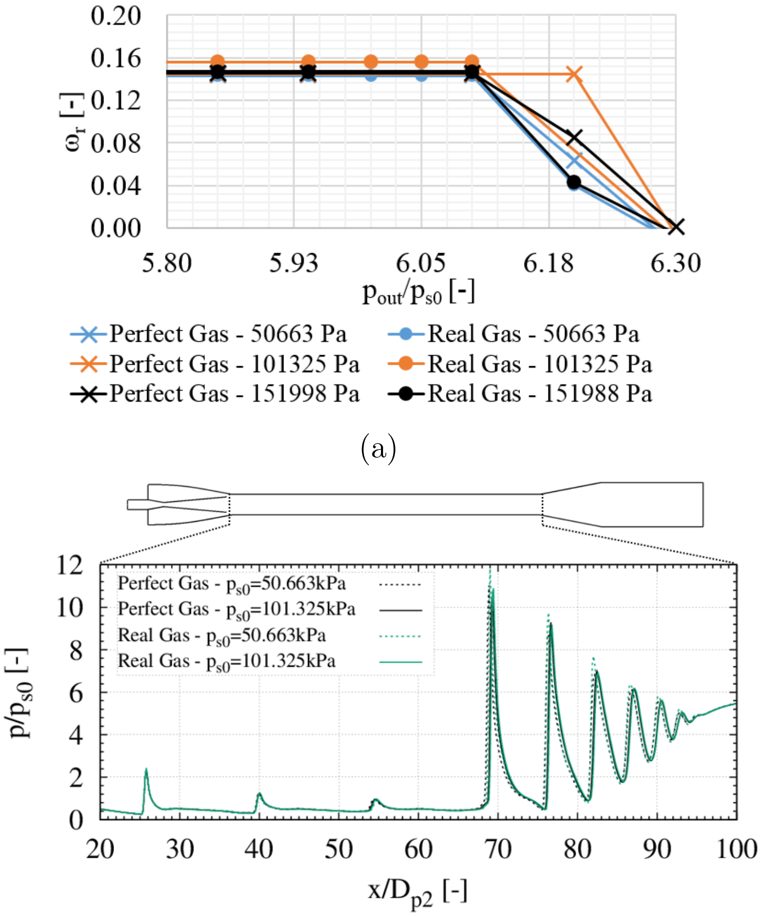

(a)

(b)

Figure 5.30 (a) Ejector entrainment ratio versus compression ratio curves for various p_{s0} values ($p_{s0} = 50.663\,\text{kPa}$, $101.325\,\text{kPa}$ and $151.988 kPa$) as predicted by the CFD-perfect gas and CFD-real gas models. (b) Comparison of centreline profiles of p/p_{s0} between both CFD models for $p_{s0} = 50.663\,\text{kPa}$ and $101.325\,\text{kPa}$. Results for for $p_{p0}/p_{s0} = 100$ and $D_{p2} = 0.02\,\text{m}$.

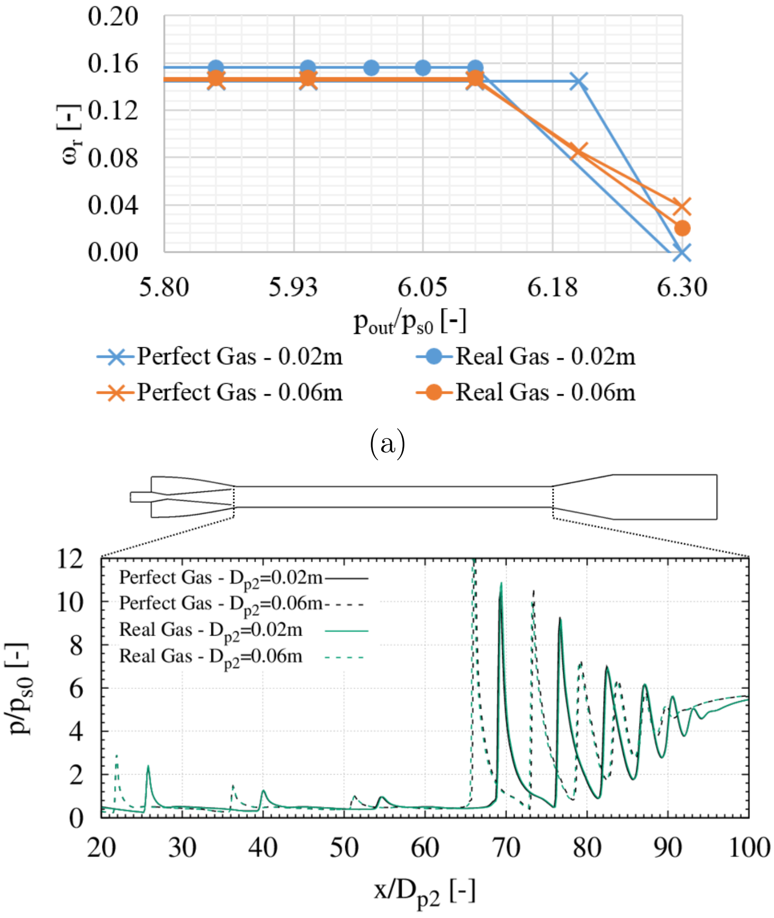

(a)

(b)

Figure 5.31 (a) Entrainment ratio versus compression ratio curves for geometrically similar ejectors with $D_{p2} = 0.02\,\text{m}$ and $0.06\,\text{m}$ as predicted by the CFD-perfect gas and CFD-real gas models. (b) Comparison of centreline profiles of p/p_{s0} between both CFD models for $D_{p2} = 0.02\,\text{m}$ and $0.06\,\text{m}$. Results for for $p_{p0}/p_{s0} = 100$ and $p_{s0} = 101.325\,\text{kPa}$.

5.4 Conclusions

A numerical study of the main internal flow features of different single-phase supersonic ejector configurations has been carried out, with particular emphasis on the flow characteristics along the constant area section, differences between double- and single-choke operation, device performance and internal losses coefficients. The following main conclusions can be drawn:

$R134a$ ejector internal characteristics

- At double-choke operation, interactions between the supersonic primary jet and secondary flow start at the nozzle exit position through the developing shear layer. Pressure profiles in this region show that the secondary flow is not pulled into the ejector but entrained through momentum transfer.
- Under fixed secondary inlet conditions, the area occupied by the secondary flow at the start of the CAS does not vary linearly with $\dot{m}_{sec}$, suggesting that the double-choke secondary mass flow rate is influenced by other factors apart from the effective area.
- At double choke operation, the shock train start location in the CAS extends between 9 and 16 times the primary nozzle exit diameter, reducing in length as the expansion ratio (p_{out}/p_{prim}) increases. At fixed inlet conditions, the relation between these two parameters approximates a parabolic trend.
- The prominent axial character of the flow at the start of the CAS limits mixing of both inlet flows in the CAS. Passive scalar maps show that the flow is not fully mixed until the shock train, where pressure fluctuations enhance the transversal velocity components.
- Other than ω_r and p_{lim}, the ejector global performance can be described by the ASHRAE efficiency (η_{ASHRAE}), the Elbel efficiency (η_{Elbel}) and the exergy efficiency (η_{chi}). Along double-choke operation, η_{ASHRAE} remains invariant with the expansion ratio whereas both η_{Elbel} and η_{χ} increase when p_{out}/p_{prim} increases.
- The exergy destruction profiles through the ejector CAS and diffuser are translated with the primary inlet exergy input, explaining the little variations in η_{xi} in these cases. For fixed inlet conditions, the exergy efficiency increases with the outlet pressure, as the flow moves farther away from the dead state.
- Internal exergy destruction profiles show that the mixing and shock waves sections represent between 50% and 70% of the losses incurred through the ejector.

Drop-in replacement of HFOs

- For the assessed $R134a$ ejector geometry and operating conditions, an average change of -5.1% (resp. $+3.5\%$) in ω_r is observed when changing the working fluid to $R1234yf$ (resp. $R1234ze(E)$). For the cases with $R1234ze(E)$, a marked reduction in the primary and secondary flows through the ejector is also observed.
- The ejector presents a better primary nozzle performance with $R134a$ in all cases. However, $R1234yf$ and $R1234ze(E)$ present respectively the best and second-best performance through the mixing and diffuser sections.
- In terms of effect on system performance, the best scenario is always obtained with $R134a$ than with the HFOs. Reductions of 10% (resp. 20%) in COP (resp. cooling capacity) were observed for $R1234yf$ at the same operating conditions as the baseline case. When the primary inlet temperature, superheat and pressure ratios are kept constant, the HDRC system with $R1234ze(E)$ has a reduction in COP (resp. cooling capacity) of 4.2% (resp. 26.6%), as well as lower generator and evaporator pressures.

Thermodynamic versus CFD models comparison

- In comparison with the CFD models, the thermodynamic model predicts a 25% higher entrainment ratio and a 5% lower limiting pressure at the assessed conditions. This difference is within the range observed in other thermodynamic models of similar complexity [García del Valle *et al.*, 2012; Huang *et al.*, 1999].
- Between the CFD-perfect gas and CFD-real gas models, a difference of about 8% (resp. 1.6%) in double-choke entrainment ratio (resp. p_{lim}) is observed, much lower than the deviations registered in the case of the $R134a$ ejector, which suggests that the air at these conditions is far from condensation and behaves like an ideal gas.
- The shock position varies linearly with the expansion ratio. Yet, whereas the CFD models predict that $65 \leq x/D_{p2} \leq 100$ for $2 \leq p_{out}/p_{s0} \leq 5.9$, the thermodynamic model assumes that $20.6 \leq x/D_{p2} \leq 96.1$ in the range $4.14 \leq p_{out}/p_{s0} \leq 5.85$.
- Given the air ideal gas behaviour at the assessed conditions, both the CFD-perfect gas and CFD-real gas models confirm that the ejector performance and flow structure can be adimensionalized in terms of D_{p2}, p_{s0}, T_{s0}, ω_r and p_{lim}. The internal flow structure is perfectly scalable in terms of the absolute secondary pressure value, although mild differences are observed in internal pressure profiles for geometrically similar ejectors, independently of the employed gas properties model.

CHAPTER 6

Performance of a Gas Supersonic Ejector with Droplets

The effect of droplet injection is assessed by considering the single-phase $R134a$ ejector described in Section 3.5.1 without droplet injection (*i.e.*: baseline case) and with injection fractions in the range $X_{inj} = \dot{m}_{inj}/\dot{m}_{prim} = 1\%$ to 10%. For all cases, droplets of diameter $\phi_{inj} = 500\,\mu\text{m}$ (average value measured by Chauvin *et al.* [Chauvin *et al.*, 2011] from a commercial atomizer) are injected at the first half of the CAS ($x = 0.015\,\text{m}$) at a temperature of $T_{inj} = -13\,°\text{C}$, which ensures liquid phase at the typical pressure ranges numerically observed in the CAS. For this analysis, both the thermodynamic and RANS model are used, as they allow to assess the influence of droplet injection from respectively a global and a local perspective. Thus, the chapter begins with a comparison of the results obtained with both approaches for the case with $X_{inj} = 10\%$, followed by an analysis of the changes in main flow properties when droplets are injected. The chapter ends with an accounting of the variations with droplet injection in terms of energy and exergy performance.

6.1 Comparison between the RANS and Thermodynamic models

In order to point out the main differences between the thermodynamic and RANS model regarding the ejector performance prediction with droplet injection, Figure 6.1 compares ejector centreline profiles of pressure, temperature and Mach number obtained with the RANS model against values predicted using the thermodynamic model at locations $L2$ through $L7$. Being the limiting situation with the highest injected fraction, the case at operating conditions OP2 with $X_{inj} = 10\%$ was chosen for this comparison. A good agreement is observed on the general evolution of the p, T and Ma profiles through the device, reflecting the good capacity of the thermodynamic model to capture the key flow features. The greatest difference is observed for the Mach number at position $L6$ (end of the CAS), where the thermodynamic model assumes an entirely subsonic flow but the RANS model predicts that the centreline Ma is still supersonic (Section 5.1, Figure 5.6).

Another noticeable difference exists in terms of the outlet temperature ($L7$), which takes the values 46.95 °C and 36.37 °C for the RANS and thermodynamic models respectively. The former predicts a higher temperature because the heat extracted from the main gas for droplet vaporization is not considered, an exchange which is indirectly comprised in the thermodynamic model through enthalpy changes. Nonetheless, it was verified that for increasing X_{inj} both models predict a decreasing outlet temperature trend.

6.2 Effects on Internal Flow Features

6.2.1 CAS and Shock Train

Figures 6.2 and 6.3 present respectively the fields of pressure and density gradient magnitude across the mixing and CAS of the ejector, obtained with the RANS model for operating conditions OP2 with droplet injection fractions in the range $X_{inj} = 0\%$ to 10%. The black iso-lines denote $Ma = 1$. In general, the global structure of the flow is similar across all cases, suggesting that the considered range of X_{inj} would be enough to affect the main flow through heat and momentum transfer without creating any large disturbances such as detachment or recirculation zones. With the highest injected fraction, cross-section averaged values of droplet volume fraction and diameter at a position 3 mm after the injection point were respectively $\leq 0.1\%$ and 8.6 µm, suggesting that droplets break and disperse shortly after reaching the main flow.

In terms of specific changes with the injected fraction, the influence on flow structure is negligible at $X_{inj} = 1\%$, in particular between the injection location and the start of the shock train. Although the latter is slightly delayed, the peak pressure and number of shock cells are very close to the baseline case (Figure 6.2). With $X_{inj} = 5\%$, a small disturbance in the flow structure is observed at the injection location. In this region, the flow is supersonic, hence, any change in the near wall region is recognized by the generation of oblique waves, as observed in Figure 6.3 at the injection location. Nonetheless, the main flow momentum at this condition is still enough to maintain its general structure. Yet, in comparison with the baseline and $X_{inj} = 1\%$ cases, a mild reduction in the peak pressure through the shock train can be observed, specially at the first cell close to the centreline. At the limit case $X_{inj} = 10\%$, the injection of droplets triggers the boundary layer detachment, revealed by the recess in the iso-Ma lines, which are no longer attached to the walls after the injection point. This results in an earlier onset of the shock train which, relative to the other cases, presents a lower peak pressure at the first cell as well as a greater length as it ends at roughly the same position within the diffuser. It is important

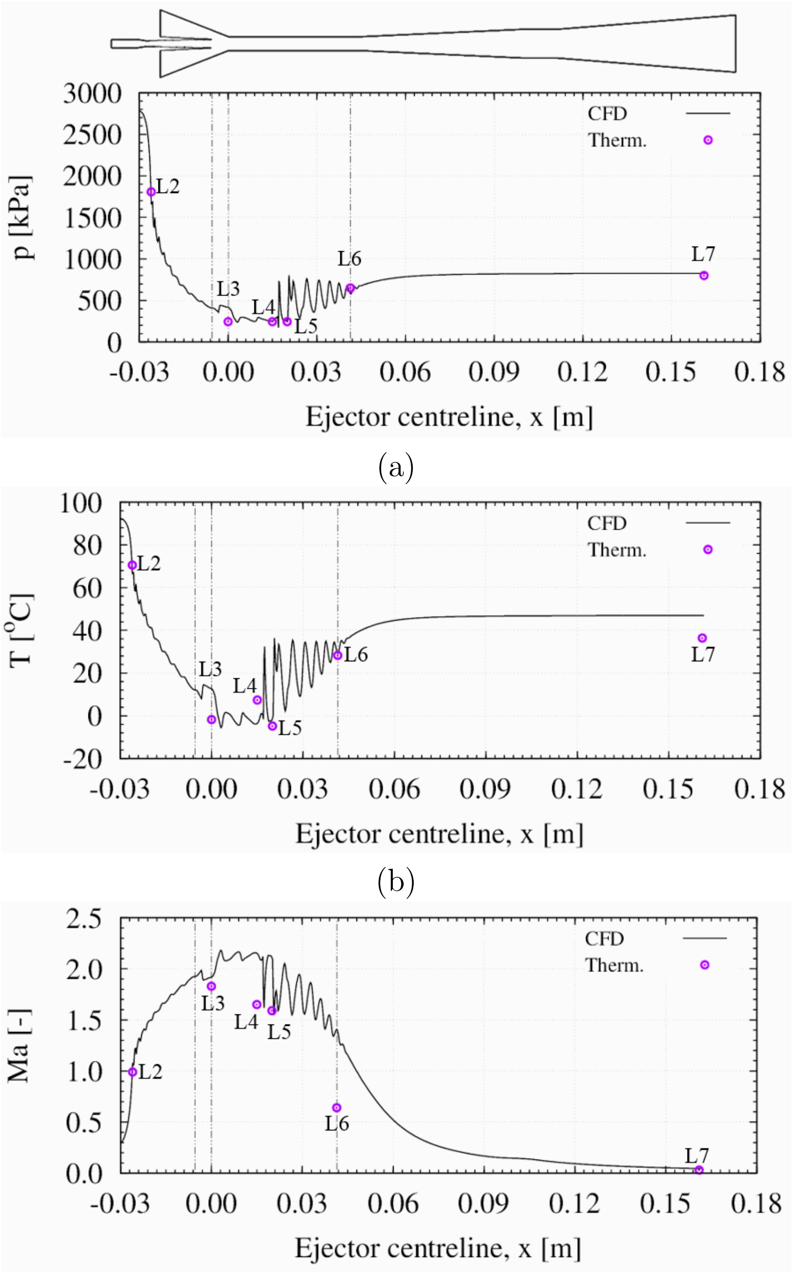

(a)

(b)

(c)

Figure 6.1 Comparison of (a) p, (b) T and (c)Ma centreline profiles obtained with the RANS model with values at locations $L2$ through $L7$ predicted with the thermodynamic model, for inlet conditions OP2 and $X_{inj} = 10\%$.

to remark that for the RANS cases, the outlet pressure value is prescribed as a boundary condition, which might restrain the position of the shock train end, as well as the pressure profile after this region.

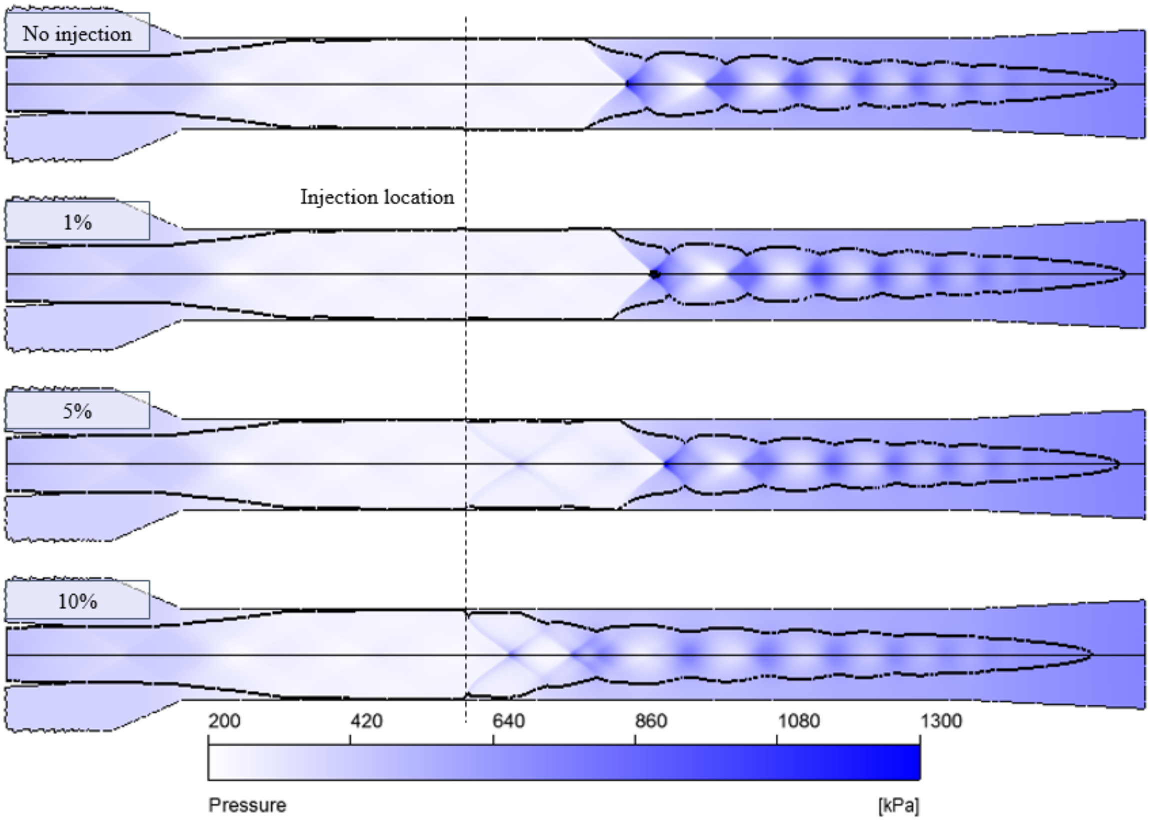

Figure 6.2 Pressure field and $Ma = 1$ iso-lines at CAS of the ejector. Results obtained with the RANS model for operating conditions OP2 and $X_{inj} = 10\%$.

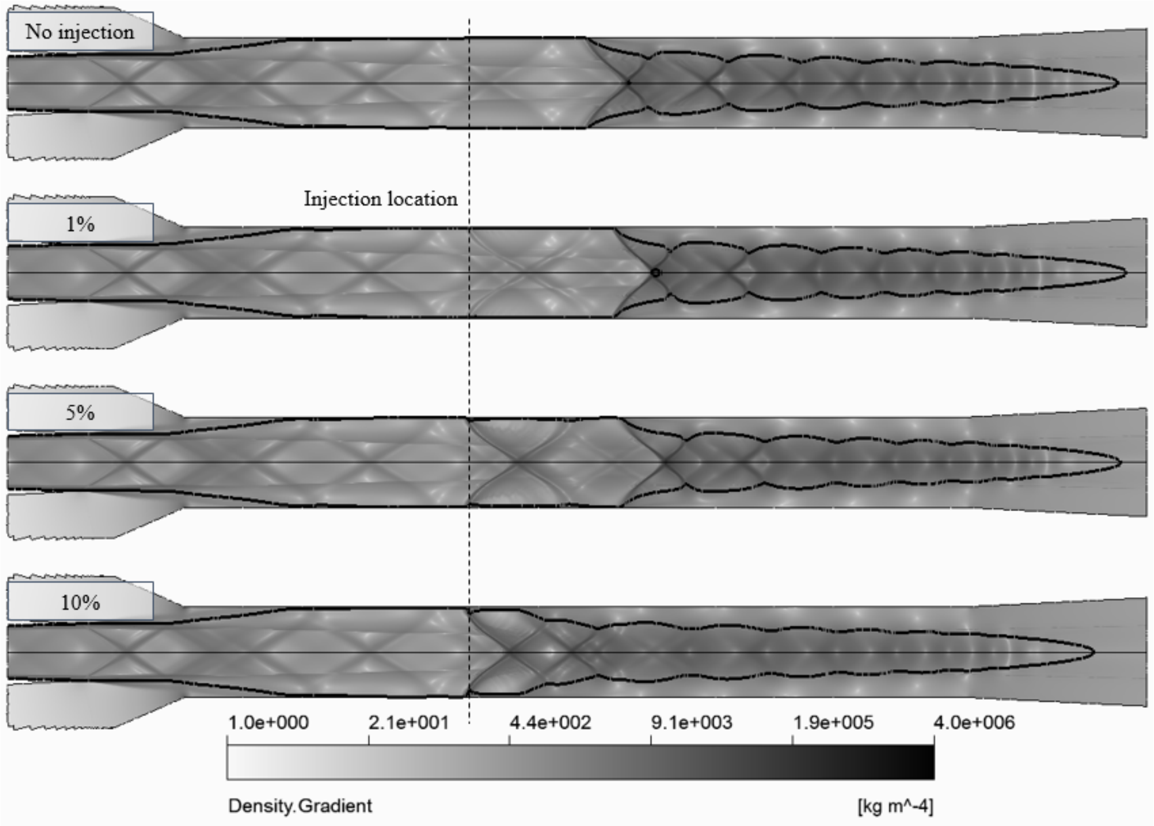

Figure 6.3 Magnitude of $\nabla\rho$ and $Ma = 1$ iso-lines at CAS of the ejector. Results obtained with the RANS model for operating conditions OP2 and $X_{inj} = 10\%$

6.2.2 Flow properties at key locations

The effects of droplet injection on pressure, Mach number and temperature at key ejector locations, as predicted by the thermodynamic model, are shown in Figure 6.4 for sections $L4$ (right before injection) to $L7$ (diffuser outlet) at working conditions OP2 and injected droplet fractions between 1% and 10%. In terms of pressure [Figure 6.4(a)], no changes are observed at sections $L4$ and $L5$ given the fact that the injection occurs in the CAS after full mixing of the primary and secondary flows. At position $L6$, a pressure reduction is observed with increasing injection fraction which suggests an effect on the shock intensity. Moreover, the lower pressure at the start of the diffuser is carried on to the outlet conditions affecting the exit pressure value (position $L7$). It must be noted that contrary to the RANS model, the outlet pressure is not fixed in the thermodynamic model such that the resulting p value at $L7$ corresponds to the limit of the double-choke region for fixed inlet conditions (OP2) and X_{inj}.

Concerning the Mach number [Figure 6.4(b)], an increase in X_{inj} leads to decreasing Ma values at position $L5$, suggesting flow deceleration. Conversely, at position $L6$ the Ma number slightly increases with X_{inj}. At the diffuser outlet, the Ma number is ~ 0.03 for all cases. These Ma profiles reflect that the flow in general decelerates with the injection of droplets, although the changes are barely noticeable. The most drastic impact of droplet injection is observed in the temperature profiles [Figure 6.4(c)]. For an injected fraction of 10%, the temperature after injection reduces by 12 °C, and the across-shock temperature jump reduces by 60% in comparison with the case $X_{inj} = 0$. A similar temperature reduction is observed at the outlet. The saturation temperature at $L7$ remains close to the baseline value of 33 °C for all the assessed conditions, meaning that increasing droplet injection reduces the superheat at the outlet from 20 °C to 5 °C. This behaviour was identical for working conditions OP1 and OP3.

6.2.3 Shock intensity

The intensity of the shock wave towards the end of the CAS is estimated in terms of the pressure ΔP and Mach number ΔMa jumps between sections $L5$ and $L6$. Figure 6.5 shows the effect of the droplet injection fraction on these quantities for conditions OP2 as predicted by the thermodynamic model. The pressure change has been normalized by the baseline value, ΔP_o. Both quantities, ΔP and ΔMa, decrease proportionally with the injected mass fraction. At $X_{inj} = 10\%$, a reduction of $\sim 8\%$ is observed for both $\Delta P/\Delta P_o$ and ΔMa. These results are in agreement with the changes in the $Ma = 1$

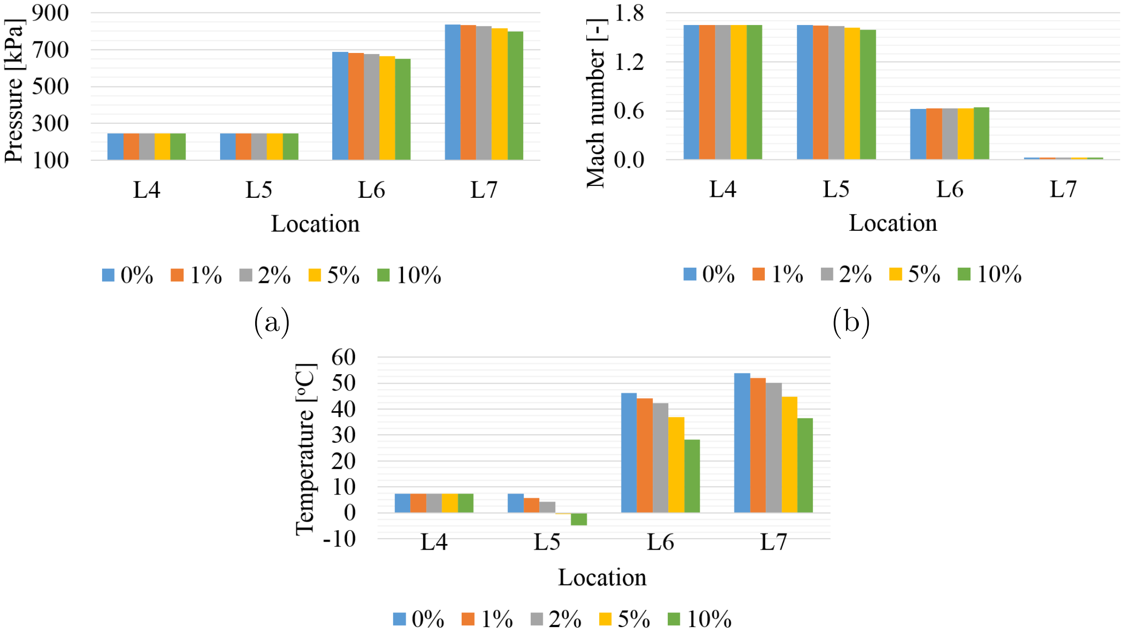

(a) (b)

(c)

Figure 6.4 Effect of droplet injection fraction X_{inj} on the (a) pressure, (b) Mach number Ma and (c) temperature at different sections of the ejector. Results for $R134a$ at the inlet conditions OP2 of Table 4.1.

iso-line and pressure peaks shown in Figure 6.2, showing that the injection of droplets effectively attenuates the shock wave intensity in the CAS, affecting one of the main sources of irreversibilities inside the ejector [Bilir Sag *et al.*, 2015; Croquer *et al.*, 2016b]. At the maximum injected fraction considered, the entropy generation between sections $L5$ and $L6$ is reduced by 10% relative to the case without injection.

6.3 Ejector Performance

6.3.1 Limiting Pressure

It was observed in Section 6.2.1 using the thermodynamic model that, for fixed inlet conditions, an increase in X_{inj} leads to a reduction in the limiting outlet pressure, *i.e.*: the maximum compression ratio achievable at double-choke operation. According to the thermodynamic model, this behaviour extends to other operating points as it is shown in Figure 6.6 for OP1, OP2 and OP3 with $X_{inj} = 1\%$ to 10%. The limiting compression ratio diminishes proportionally with the increasing injection fraction, from 1% at $X_{inj} = 1\%$ to 5% at $X_{inj} = 10\%$.

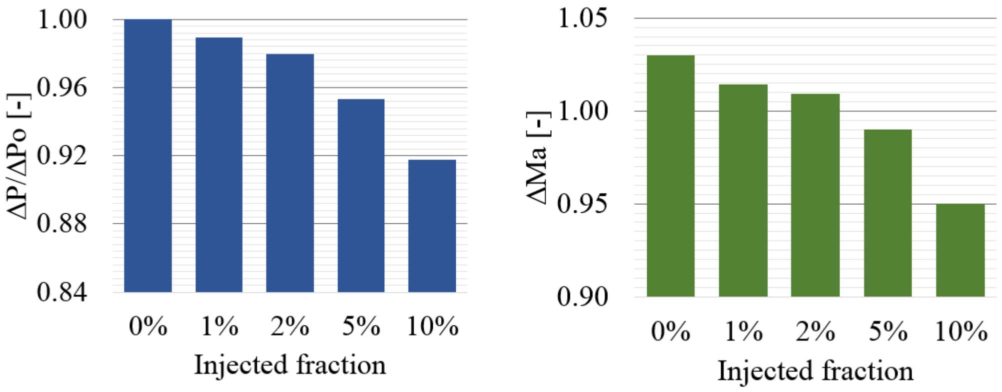

(a)
(b)

Figure 6.5 Effect of the droplet injection fraction X_{inj} on the (a) pressure and (b) Mach number Ma change across the shock wave, relative to the case without droplets. Results for $R134a$ obtained with the thermodynamic model at the inlet conditions OP2.

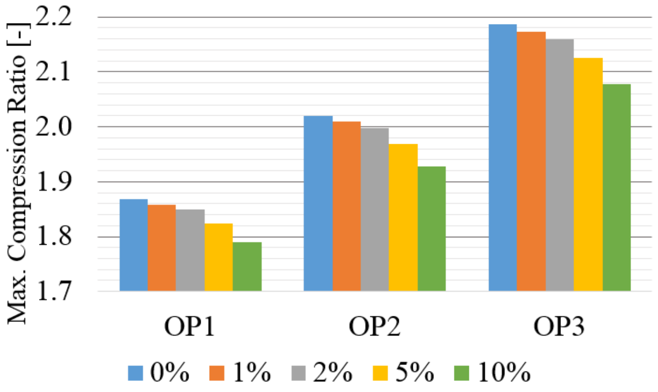

Figure 6.6 Effect of the droplet injection fraction X_{inj} on the maximum compression ratio achievable by the ejector. Results for $R134a$ at the inlet conditions OP1, OP2 and OP3 of Table 4.1.

This reduction in the limiting pressure can be explained from a 2^{nd} Law perspective using the enthalpy-entropy diagram shown in Figure 6.7. As proposed by Galanis and Sorin [2016], and following the entropy generation principle, the minimum entropy at the ejector outlet is the sum of the ejector inlet entropy, $S_{in} = (S_{prim} + \omega_r S_{sec})/(1 + \omega_r)$, plus that generated through the device. This imposes a limit on the pressure ratio, as the specific outlet entropy decreases with increasing P_{ratio}. In the cases with droplet injection, the additional entropy generated through injection augments the minimum possible outlet entropy while, at the same time, the specific outlet entropy reduces linked with the outlet temperature [Figure 6.4(c)]. These two effects close the gap between the outlet ejector conditions and the minimum possible entropy, thus reducing the compression ratio.

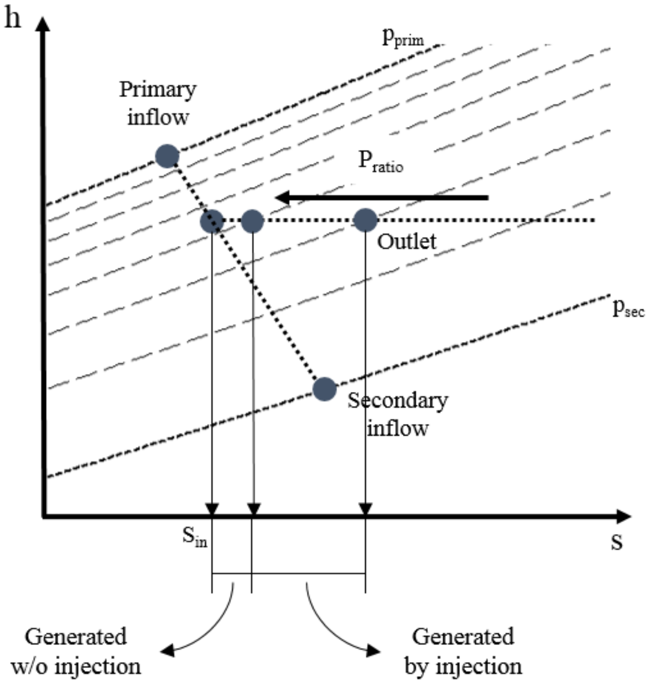

Figure 6.7 Enthalpy (h) - Entropy (s) schematic diagram, marking the primary inlet, secondary inlet, and outlet points of the ejector.

Using the RANS model, the ω_r versus P_{ratio} curve has been drawn in Figure 6.8 for the baseline case corresponding to OP2 and the case with $X_{inj} = 10\%$. As expected, there is no change in the double-choke entrainment ratio, as it is defined by phenomena occurring prior to the injection of droplets. The flow up to this point being supersonic, droplets have no effect whatsoever on upstream events. It was verified through the results with droplet injection, that not only ω_r but also both $\dot{m}_{prim}$ and $\dot{m}_{sec}$ are identical to the baseline case. Apart from the previously discussed reduction in p_{lim}, a slight reduction in the off-design entrainment ratio is also observed in the case with droplet injection. This disagrees with previous studies on air ejectors with droplets mixed with the primary flow, which report an increase in the off-design secondary mass flow rate, particularly at low primary inlet pressures [Al-Ansary and Jeter, 2004]. Further insight into the flow structure through the CAS at single-choke operation is shown in Figure 6.9, which compares the magnitude of the axial velocity u in the mixing and CAS of the ejector at inlet conditions OP2 and an outlet saturation temperature of 34 °C. At this outlet condition, the secondary mass flow rate for the baseline case (resp. with $X_{inj} = 10\%$) is 16.263 g /s (resp. 13.125 g/s), barely lower than the double-choke value of 16.354 g/s. The $Ma = 1$ iso-lines reveal for both cases that the flow is not entirely supersonic in the CAS, but the secondary remains subsonic between the motive jet and the outer walls. In addition, a closer look at the start of the CAS shows that the secondary flow passage area is similar for both cases but the velocity u is higher in the baseline case.

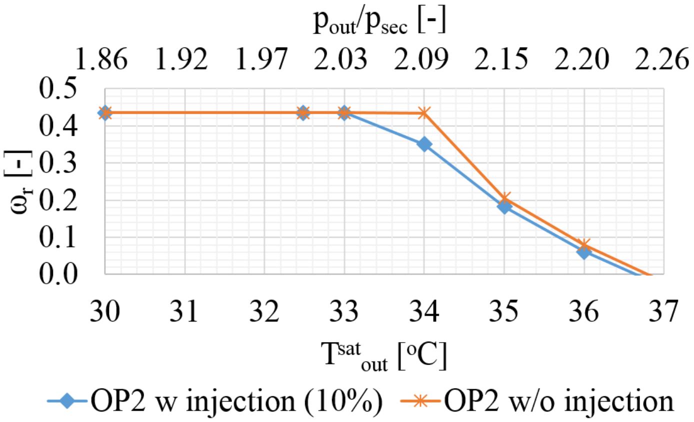

Figure 6.8 Entrainment versus compression ratio curves for the ejector with $X_{inj} = 10\%$ and without droplet injection. Results obtained using the RANS model at operating conditions OP2.

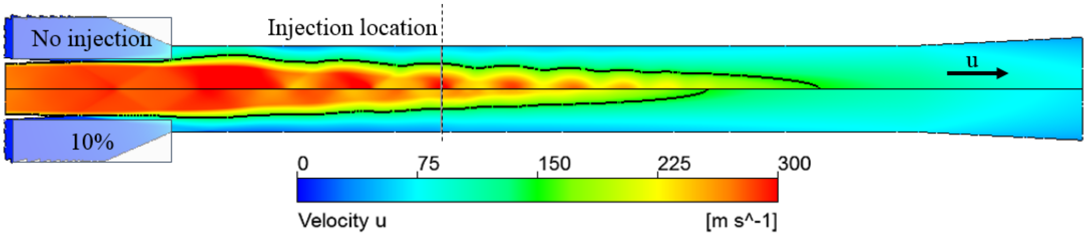

Figure 6.9 Map of the axial velocity u across the CAS of the ejector. Results obtained using the RANS model for operating conditions OP2 and $X_{inj} = 10\%$.

6.3.2 Energy and Exergy accounting

The ejector energy and exergy performances have been assessed using the thermodynamic model. Figure 6.10 shows the variations in the ejector efficiency and exergy efficiency with injection fractions of 1% to 10% at conditions OP1, OP2 and OP3. Both the exergy efficiency and the ejector efficiency reduce with increasing X_{inj}, independently of the operating conditions. Regarding η_{Elbel}, an average performance loss of 11% is observed for the greatest injection fraction, reflecting the decrease in the outlet pressure shown in Figure 6.4. For lower outlet pressures at fixed inlet conditions, the secondary flow compression ratio diminishes while the primary flow expands even more, resulting in less energy recovered by the ejector.

Concerning the exergy efficiency, a reduction of 15% in average is observed when the injection mass fraction is 10%, confirming that droplet injection results in less exergy

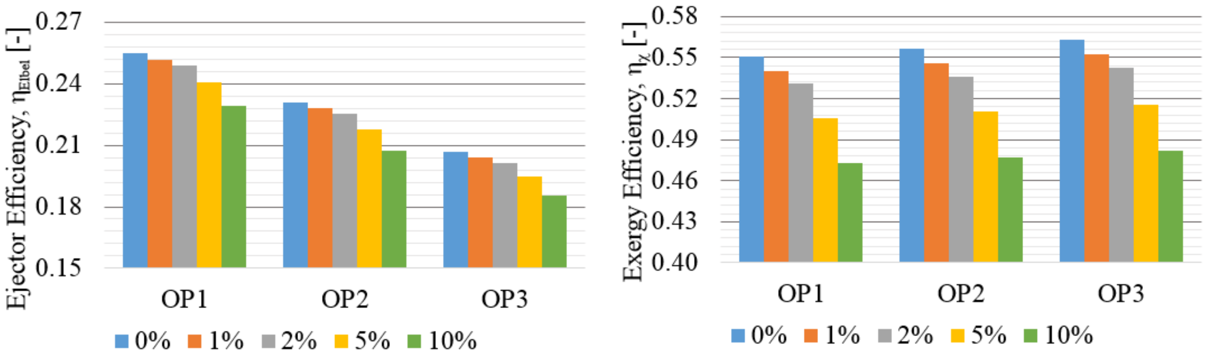

Figure 6.10 Effect of the droplet injection fraction X_{inj} on the ejector efficiency η_{Elbel} and exergy efficiency η_{χ}. Results obtained using the thermodynamic model.

recovered relative to the total entering at both inlets. The location where this exergy is destroyed can be pinpointed using Figure 6.11 which presents the exergy evolution through the ejector for the cases with $X_{inj} = 0\%$ to 10%, as determined using the RANS model. It is observed that at the point of injection, the main flow exergy reduces as X_{inj} increases, an effect which is carried on to through the rest of the device. Consequently, the available exergy at the ejector outlet also diminishes. An accounting of these effects using the thermodynamic model is shown in Figure 6.12, which decomposes the contribution to the total exergy destroyed through the ejector into four sections: mixing, droplet injection, shock waves and subsonic compression. Although droplets effectively attenuate the normal shocks in the CAS and reduce their contribution to exergy destruction by about 35% for $X_{inj} = 10\%$, other processes associated with the droplet injection (*e.g.*: mixing with the main flow) present an even greater contribution to the total exergy destroyed. For example, in the limiting case of $X_{inj} = 10\%$, 3.9 kJ/kg of exergy are destroyed at the point of injection which is 6 times the exergy destroyed across the shock wave in the case without injection. Thus, although the expected shock attenuation effect is carried out, other factor damaging the effectiveness of the ejector are introduced, resulting in a lower performance. From the perspective of a HDRC, a lower performance would be expected given that the injection of droplets render the ejector less effective for energy recovery and compression.

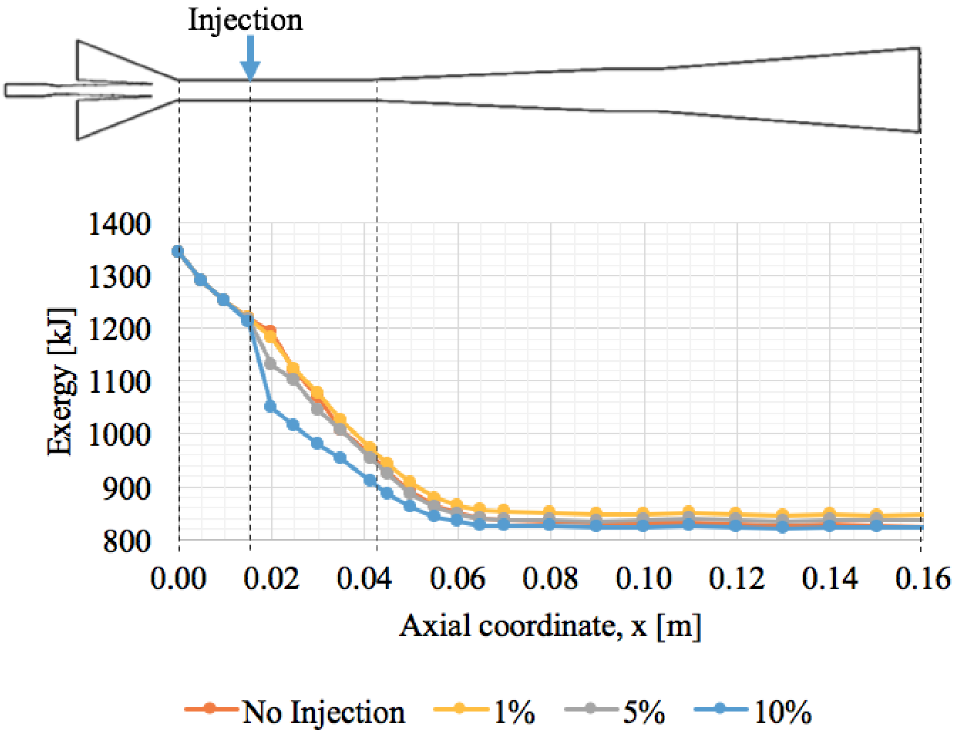

Figure 6.11 Exergy profiles through the ejector. Results obtained using the RANS model for inlet conditions OP2.

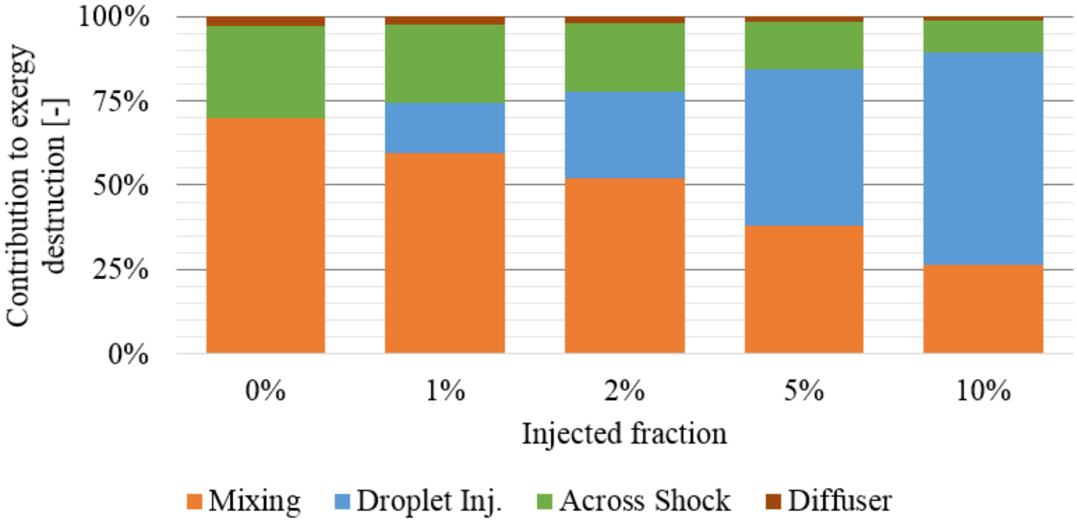

Figure 6.12 Effect of the droplet injection fraction X_{inj} on the contribution of each section to the exergy destruction across the ejector. Results obtained using the thermodynamic model at inlet conditions OP2.

6.4 Conclusions

This chapter presents the influence of injecting droplets into the constant area section of a single-phase supersonic ejector for refrigeration purposes, as predicted using a thermodynamic and a RANS model. While the former allows for an assessment of the impact over the global ejector performance, the latter provides valuable insight on the changes to the internal flow features, in particular the shock structure.

- A vis-à-vis comparison of the pressure, temperature and Mach number centrelines profiles of the ejector with an injected fraction of 10%, obtained with the RANS model, with the values predicted by the thermodynamic model at key ejector locations, shows that both approaches coincide in the general flow structure and the changes in flow properties with varying injection fractions.
- With an increasing injection fraction in the range 1% to 10%, pressure and magnitude of $\nabla\rho$ fields show that the general flow structure within the ejector remains unchanged, suggesting that the influence of droplets occurs instead through changes in the thermodynamic properties of the flow. The most remarkable changes were observed for an injection fraction of 10%, which induces boundary layer detachment and an earlier, less intense, shock train in the constant area section.
- In terms of flow properties, the thermodynamic model shows that the greatest impact of droplet injection occurs on the temperature. In particular, for an injected fraction of 10%, the temperature after injection reduces by 12 °C, and the across-shock temperature jump by 60%, relative to the baseline case without injection. Moreover, while the outlet saturation temperature varies by less than 1 °C, the superheat reduces from 20 °C at the baseline case, to 5 °C when $X_{inj} = 10\%$.
- In terms of compression ratio, as the droplet injection fraction increases, the limit double-choke pressure decreases. This results from a reduction in the outlet ejector temperature and the extra entropy generated trough droplet injection.
- In terms of global performance, although at an injection fraction of 10%, the shock intensity reduces by 8%, the ejector Elbel efficiency and exergy efficiency reduce respectively by 11% and 15%. Exergy profiles through the device show that as X_{inj} increases, the main flow exergy after the injection location further reduces. This effect is carried out to the domain exit, resulting in a lower available exergy.

CHAPTER 7

CONCLUSIONS AND FUTURES VIEWS

Conclusions de la thèse

Une analyse numérique de la structure d'écoulement dans des éjecteurs supersoniques gazeux et de ses changements lorsque des gouttelettes sont injectées avant l'apparition du train d'ondes de choc a été réalisée en utilisant les résultats combinés de: (i) un modèle RANS construit à la suite d'une étude comparative comprennant cinq modèles de turbulence et trois modèles pour les propriétés des fluides; et (ii) un modèle thermodynamique spécifiquement formulé pour déterminer la performance de l'éjecteur compte tenu de la géométrie et des conditions de fonctionnement souhaitées. De plus, une meilleure compréhension des interactions gouttelettes-flux principal a été obtenue en implémentant une phase discrète dans le modèle RANS, représentant les trajectoires de la phase dispersée et en prenant en compte la fragmentation des gouttes et les échanges de quantité de mouvement et d'énergie thermique entre les phases.

Dans la première étape de cette thèse, l'étude de référence (publiée dans un journal à comité de lecture Croquer *et al.* [2016a]) a montré que la combinaison du modèle de turbulence $k-\omega$ SST à bas nombre de Reynolds avec le modèle de gaz réel REFPROP offre le meilleur compromis en termes de précision et aux coûts de calcul. Le modèle est capable de capturer correctement la structure du train d'ondes de choc [Bouhanguel *et al.*, 2015; Rao and Jagadeesh, 2014] et de prédire le rapport d'entraînement avec un écart de seulement $\leq$ 6% par rapport aux valeurs expérimentales de García del Valle *et al.* [2014]. En utilisant cette stratégie de modélisation RANS, une analyse en profondeur de l'écoulement et des transferts dans des éjecteurs de gaz supersoniques monophasiques sous différentes configurations a été réalisée. Les contributions originales de ces études ont été publiées dans trois articles de revue ([Croquer *et al.*, 2016b,c; Fang *et al.*, 2017]) et sont résumées dans ce qui suit:

— Concernant les caractéristiques internes et la performance exergétique d'un éjecteur au $R134a$, les comparaisons des profils de pression au début de la section de mélange montrent que la pression de l'écoulement secondaire peut être supérieure ou inférieure à la pression du jet principal, suggérant que les interactions par cisaillement jouent un rôle important sur l'entraînement. De plus, la relation entre le débit massique secondaire et la surface de passage laissée par le jet principal n'est pas strictement linéaire, indiquant l'influence d'autres phénomènes (par exemple la transfert d'énergie du jet principal) dans la détermination du débit massique secondaire dans le régime dit *double-choke*. En ce qui concerne les performances de l'éjecteur, les efficacités maximales ASHRAE, Elbel et d'exergie pour les conditions d'entrée fixes ont été atteintes près de la limite d'exploitation (régime *double-choke*). Les profils d'exergie à travers l'éjecteur montrent qu'environ 70% de l'apport d'exergie est détruit par le mélange et les ondes de choc. Cela a été confirmé par les coefficients de perte calculés, qui pour les sections de buse, de mélange et de diffusion sont en moyenne de ~ 1, 0.58 et 0.74 respectivement.

— Il y a des différences négligeables en termes de structure de l'écoulement lorsque le $R134a$ est remplacé par des HFO comme le $1234yf$ et le $R1234ze(E)$, bien que les conditions de fonctionnement dans ce dernier cas doivent être adaptées pour éviter la condensation. Aux mêmes conditions de fonctionnement, l'utilisation du $R1234yf$ a un léger effet défavorable sur le rapport d'entraînement (environ 2 points) mais le rapport de compression maximal dans le régime *double-choke* augmente de 3%. Aux conditions adaptées (même température d'entrée primaire, rapports de surchauffe et de pression par rapport au point critique de chaque fluide), le rapport d'entraînement augmente de 3.5% en utilisant le $R1234ze(E)$, bien que le taux de compression maximum et le les débits massiques sont sévèrement diminués. Ces changements se traduisent globalement par une baisse moyenne du COP et de la capacité de refroidissement de 10% et 20% (respectivement 4.2% et 26.6%) en utilisant $R1234yf$ (resp. $R1234ze(E)$).

— Une comparaison avec les prédictions d'un modèle thermodynamique concernant la conception d'un éjecteur à air a montré que lorsque le gaz de travail se rapproche du comportement de gaz idéal, les différences qualitatives entre les modèles de gaz réels et parfaits diminuent. De plus, diverses hypothèses habituellement faites dans les modèles thermodynamiques sont validées, en particulier que la position de départ du choc dans le CAS varie linéairement avec le taux d'entraînement et que le débit de l'éjecteur ainsi que sa performance globale peuvent être réduites à quelques paramètres sans dimension: la température et pression à l'entrée secondaire, le diamètre de la gorge de la buse primaire, le rapport d'entraînement et le taux de compression, même dans des conditions de gaz réel.

Dans la seconde étape de cette thèse, un modèle thermodynamique a été développé en suivant les caractéristiques d'écoulement observées pour les éjecteurs monophasiques et en appliquant les principes de conservation de la masse, de la quantité de mouvement et de l'énergie dans les régions clés de l'éjecteur. Différent des modèles thermodynamiques communs, l'algorithme présenté dans cette thèse adopte une approche *opération* pour les éjecteurs de gaz réels, c'est à dire, la performance est déterminée pour un ensemble donné de paramètres géométriques et de fonctionnement. Ainsi, les données d'entrée comprennent les conditions de fonctionnement aux entrées et les diamètres de la gorge primaire, la section de surface constante et la sortie du diffuseur, tandis que les résultats de sortie incluent les propriétés thermodynamiques aux sections principales du dispositif et les rapports d'entraînement et de compression. Le développement du modèle et les principaux résultats concernant les changements de performance de l'éjecteur sont publiés dans une revue à comité de lecture Croquer *et al.* [2017]. En comparaison avec les données expérimentales monophasiques, on observe une déviation moyenne de 18% (resp. $4,5\%$) en termes de rapport d'entraînement en régime *double-choke* (resp. rapport de compression limite), qui se situe dans la même fourchette que pour des modèles similaires avec une formulation de conception [Ameur *et al.*, 2016; Huang *et al.*, 1999]. Sous des conditions biphasiques, le modèle est capable de capturer les changements du rapport d'entraînement avec la surchauffe d'entrée primaire dans des éjecteurs au $R134a$ et de prédire le débit massique critique du CO_2 dans des tuyères convergentes-divergentes avec une précision de 10%.

En général, les gouttelettes injectées normalement dans l'écoulement dans la première moitié du CAS ont un impact négatif sur la performance de l'éjecteur. Les résultats du modèle RANS ont montré que la structure de l'écoulement interne n'est pas modifiée sauf pour les fractions d'injection très élevées (10% du débit massique primaire). Dans ces conditions, un détachement de la couche limite est capturé, ce qui conduit à un démarrage anticipé du train de choc. De même, l'intensité du choc diminue de 8% (en termes de saut de pression). Ces observations vérifient l'hypothèse que l'injection de gouttelettes dans le CAS du dispositif permettrait de réduire l'intensité du choc et l'entropie associée à ces chocs. Néanmoins, l'efficacité d'Elbel et l'efficacité exergétique sont réduites respectivement de 11% et 15% et le taux de compression maximal dans le régime *double-choke* diminue de 10%. Ce désavantage dans les performances du dispositif est lié aux pertes supplémentaires générées par le mélange des gouttelettes avec le flux primaire, l'entropie supplémentaire injectée avec les gouttelettes et la réduction constante de la température de sortie avec une augmentation de la fraction d'injection de gouttelettes.

Au-delà des résultats négatifs obtenus sur l'injection de gouttelettes dans l'éjecteur, cette thèse montre la faisabilité de combiner les perspectives de modélisation RANS et thermodynamique dans l'analyse d'écoulements aussi complexes (supersonique, ondes de choc obliques, diphasiques ...). Elle montre aussi l'importance acquise par les méthodes numériques durant ces dernières années, qui sont devenues des outils très puissants pour l'étude des configurations d'écoulements très difficilement accessibles avec des méthodes expérimentales, dues à la petite taille des systèmes, leur isolation thermique et la nécessité de prévenir des fuites lorsque des réfrigérants de type HFC ou HFO sont utilisés.

Perspectives futures

Perspectives futures - Validation expérimentale de l'influence de l'injection de gouttes sur la performance de l'éjecteur

Compte tenu des simplifications importantes sur lesquelles reposent les études numériques, il est toujours nécessaire de valider la qualité des résultats par rapport aux données expérimentales. Ceci est particulièrement critique dans le contexte des éjecteurs supersoniques, car il a été montré dans la section 3.5.3 et dans des études antérieures [Bartosiewicz *et al.*, 2006] que les modèles de turbulence prédisent avec des écarts importants la structure interne de l'écoulement, même s'ils sont capables de bien prédire leur performance globale (taux d'entraînement et de compression).

Dans le but d'évaluer la précision des modèles numériques présentés dans cette thèse, un banc d'essai expérimental comprenant une boucle de réfrigération HDRC de 3 kW fonctionnant au $R134a$ est en construction à CanmetÉNERGIE (Varennes, Québec). La source de chaleur du cycle est une chaudière électrique de 10 kW qui génère de la vapeur saturée de $R134a$ dans un intervalle des températures de 70 °C à 80 °C. Des éléments électriques sont prévus pour surchauffer la vapeur de 5 °C environ. Le condenseur et l'évaporateur sont des échangeurs à plaques brasées avec des capacités nominales respectives de 15 kW et 5 kW. La chaleur du condenseur est transférée dans une boucle de propylène-glycol/eau à 30%. Le système peut atteindre des températures de saturation en entrée secondaire de 5 °C environ.

L'éjecteur a été conçu pour des applications monophasiques. Il est fabriqué en laiton et a des diamètres respectifs de section de col et de section constante de 3.27 mm et 7 mm. Deux trous ont été percés au début et au milieu de la section constante pour placer un injecteur de sorte que les gouttelettes entrent perpendiculairement dans le flux principal. Les gouttelettes au $R134a$ seront générées à l'aide d'un atomiseur à jet tournant, fabriqué par *Lee Company*, avec un diamètre d'orifice nominal de 0.2 mm, un angle de pulvérisation nominal de 70 °C et une pression différentielle recommandée entre 345 kPa et 1380 kPa.

La Figure 7.1 montre un plan préliminaire de l'éjecteur CAS avec l'emplacement des sites d'injection des gouttelettes.

La collecte de données attendue comprend: les valeurs de débit massique, pression et température aux entrées; les valeurs de pression aux parois prises au début et à la fin de la section constante; et la pression et la température au niveau du générateur, de l'évaporateur et du condenseur. Cela permettra d'effectuer une comparaison avec les résultats numériques concernant le comportement global de l'éjecteur (courbe ω_r en fonction de P_{ratio} pour diverses conditions de fonctionnement) et les effets d'attenuation des chocs. De plus, le banc d'essai permettra de déterminer l'effet de l'injection de gouttelettes sur la performance du cycle complet (en termes de COP et de capacité de refroidissement), un effet non pris en compte dans les études numériques. Le banc expérimental est actuellement en phase de test pour assurer sa bonne construction, les premiers essais expérimentaux étant prévus pour le premier trimestre de 2018.

Simulation aux Grandes Échelles d'un éjecteur supersonique à air

Avec une stratégie de modélisation RANS générale pour les éjecteurs supersoniques déjà esquissée, les efforts se divisent maintenant en deux voies distinctes: d'une part, exploiter les résultats RANS pour étudier le transfert d'énergie et d'exergie pour des configurations spécifiques, comme la comptabilité entropique effectuée par Sierra-Pallares *et al.* [2016] et le concept des *conduits d'éxergie* introduit par Lamberts *et al.* [2017b]; d'autre part, d'explorer d'autres approches de modélisation numérique qui, bien que d'un coût de calcul plus élevé, fournissent beaucoup plus de détails et une représentation plus réaliste de l'écoulement. La prochaine étape logique dans cette dernière direction est la Simulation des Grandes Échelles (LES) des éjecteurs supersoniques.

Dans l'approche de Simulation des Grandes Échelles (LES), la solution d'une version filtrée des équations de Navier-Stokes est recherchée. Le processus de filtrage, qui prend généralement la taille de la grille locale comme seuil, divise les structures de l'écoulement en deux groupes: celles qui sont plus grandes que le seuil (qui dépendent souvent des cas) sont résolues, tandis que les plus petites sont modélisées. Ainsi, une représentation plus réaliste des structures de l'écoulement transportant l'énergie est produite, sans les lourdes simplifications intrinsèques aux étapes de moyennage de l'approche RANS. L'inconvénient de cette approche est le coût de calcul associé plus élevé, tant en termes de puissance de calcul que de mémoire, car des maillages plus fins sont nécessaires (les tailles d'éléments typiques se situent dans la gamme des échelles inertielles) et il est nécessaire de collecter des résultats instantanés sur une longue période de temps simulée. Des descriptions théoriques complètes de la technique LES pour les écoulements incompressibles et compressibles peuvent être trouvées respectivement dans Sagaut [2006] et Garnier *et al.* [2009].

Actuellement, un modèle LES innovateur d'un éjecteur supersonique à air est en cours de développement, avec l'objectif principal d'effectuer une analyse détaillée des structures turbulentes et des échanges d'énergie se produisant lorsque les deux flux interagissent à travers les zones de mélange et de surface constante. Le cas de référence correspond à une installation expérimentale située à l'Université Catholique de Louvain (Belgique), équipée d'un éjecteur supersonique de section rectangulaire (largeur 0.05 m, longueur 1.52 m) et de hauteurs, respectivement au niveau de la gorge primaire et de la section constante, de 0.006 m et 0.027 m. L'écoulement est caractérisé par un nombre de Reynolds de $Re = 6.6 \times 10^5$ et de Mach de $Ma = 1.61$, avec des conditions de 5 bar et 300 K à l'entrée principale, et de 0.96 bar et 300 K à l'entrée secondaire. Le lecteur peut se référer à Lamberts *et al.* [2017a] pour une description détaillée de l'installation expérimentale.

Le modèle numérique a été construit en supposant un comportement de gaz parfait et que le caractère transversal du flux est négligeable par rapport aux composantes axiale et verticale. Ainsi, afin de réduire les coûts de calcul, le domaine simulé est une section 0.01 m de largeur avec symétrie des deux côtés. La discrétisation spatiale a été réalisée en utilisant un maillage non-structuré avec 240 millions d'éléments tétraédriques avec 21 couches prismatiques adjacentes aux parois. Compte tenu de la taille extrêmement petite des éléments nécessaires pour résoudre complètement les couches limites, l'hypothèse d'une fonction de parois logarithmique a été préférée, ce qui assouplit l'exigence de $y+$ à une moyenne de 25 partout dans le domaine. La pression totale et la température totale sont prescrites aux deux entrées, tandis que la pression statique est fixée à la sortie.

La solution numérique est obtenue en utilisant le code d'éléments finis *AVBP* [Schoenfeld and Rudgyard, 1999], qui résout les équations de Navier-Stokes filtrées en utilisant un schéma de Taylor-Galerking en deux étapes (TTG4A), de *4ème* ordre en temps et de *3ème* ordre en espace [Colin and Rudgyard, 2000]. De manière similaire à l'approche RANS, des termes supplémentaires ressemblant à un tenseur de contrainte apparaissent dans les équations de Navier-Stokes filtrées, qui font la liaison entre les échelles porteuses d'énergie résolues et les échelles modélisées (dissipation d'énergie). Ces termes sont supposés être proportionnels à une viscosité numérique, qui est calculée en utilisant le modèle *WALE* de Nicoud and Ducros [1999], connu pour sa meilleure performance pour des écoulements confinés. De plus, en attendant l'apparition d'ondes de choc, une viscosité artificielle supplémentaire est ajoutée pour lisser la solution dans des régions de gradients aigus détectés en utilisant un capteur basé sur la pression. Les calculs sont actuellement en cours à l'aide du superordinateur *Mammouth Parallèle 2* situé à *l'Université de Sherbrooke*. L'allocation pour ce projet consiste en 100 nœuds AMD Opteron, chacun avec 12 cœurs, 32 Go de RAM et une performance théorique de 201.6 Gflops par nœud. Avec cette configuration, simuler un temps caractéristique de l'éjecteur ($t_c = 0.003\,\mathrm{s}$, le temps nécessaire à une particule pour traverser le domaine de calcul) prend environ 36 jours.

Le calcul a été initialisé en utilisant une solution RANS. Une fois le calcul LES lancé, la simulation doit être exécutée pendant un certain temps pour permettre à la configuration d'atteindre un état stable. Dans ce cas, la stabilisation a été observée après environ 5 temps caractéristiques. Au-delà, la simulation est poursuivie pour quelques temps supplémentaires tout en recueillant les données d'intérêt. Dans ce cas, le domaine complet est stocké toutes les 1×10^{-4} s, des plans médians verticaux sont stockés avec une fréquence de $t_c/100$ et des propriétés de l'écoulement en différents points spécifiques du domaine sont stockées avec une fréquence de $t_c/60000$.

La validation expérimentale sera effectuée en termes de mesures de pression pariétale moyenne et de comparaison avec l'imagerie Schlieren. Un exemple de ce dernier est montré sur la Figure 7.2. Bien qu'étant à un stade préliminaire, la structure du jet principal prédite par la LES est en bon accord avec les visualisations expérimentales, en particulier le nombre et l'emplacement des cellules distinctes dans le jet principal sont bien saisis.

Quelques exemples d'informations attendues de ces calculs sont donnés sur les Figures 7.3 et 7.4. La première figure présente une prise instantanée des structures turbulentes générées au niveau de la couche de mélange colorée par leur sens de rotation, qui donne un aperçu des mécanismes d'échange à travers la couche de cisaillement et révèle la plus grande précision possible atteinte par la LES. La Figure 7.4 montre les fluctuations de pression en différents points à travers le domaine d'éjecteur. En se basant sur des variations temporelles des différentes quantités telles que la pression, les composantes de vitesse et les contraintes de Reynolds, on pourra mieux caractériser l'écoulement et enfin comprendre la relation entre ces caractéristiques complexes et la performance de l'éjecteur.

Thesis Conclusions

A numerical analysis of the flow structure of gas supersonic ejectors and its changes when droplets are injected before the onset of the shock train has been carried out using the combined results of: (i) a RANS model, built following a benchmark study comprising five two-equation turbulence models and three gas properties models; and (ii) a thermodynamic model specifically formulated to determine the ejector performance given the geometry and desired operating conditions. In addition, further insight on the droplet-main flow interactions was obtained by implementing a discrete phase in the RANS model, accounting for breakup and momentum and thermal energy exchanges.

In the first stage of this thesis, the benchmark study (published in a peer reviewed journal under Croquer *et al.* [2016a]) showed that the combination of the $k-\omega$ SST low-Reynolds number turbulence model with the REFPROP real gas equation database offers the best compromise in terms of accuracy versus computational costs, as it is able to properly capture the shock structures reported in ejector flow visualizations [Bouhanguel *et al.*, 2015; Rao and Jagadeesh, 2014] and has a deviation of $\leq 6\%$ relative to the experimental entrainment ratio data of García del Valle *et al.* [2014]. Using this RANS modelling strategy, an in-depth analysis of the flow in single-phase supersonic gas ejectors under different configurations was performed. The original contributions of these studies have been published in three peer reviewed articles ([Croquer *et al.*, 2016b,c; Fang *et al.*, 2017]) and are summarized in the following:

- Concerning the internal characteristics and exergy performance of an $R134a$ ejector, comparisons of the pressure profiles at the start of the mixing section show that the secondary flow pressure can be higher or lower than the motive jet pressure, suggesting that entrainment occurs in great part by shear interactions. Furthermore, the relation between the secondary mass flow rate and the flow passage area left by the motive jet is not strictly linear, indicating the influence of other phenomena (*e.g.*: energy transfer from the motive jet) in the determination of the secondary double-choke mass flow rate. Concerning ejector performance, the maximum ASHRAE, Elbel and exergy efficiencies for fixed inlet conditions were achieved near the double-choke operation limit. Exergy profiles through the device show that about 70% of the exergy input is destroyed by mixing and shock waves. It was confirmed by the computed loss coefficients, which for the motive nozzle, mixing and diffuser sections are respectively ~ 1, 0.58 and 0.74 in average.
- There are negligible differences in terms of internal flow structure when the working fluid is substituted from $R134a$ to $R1234yf$ or $R1234ze(E)$, although the operating conditions in the latter case must be adapted to avoid condensation. Under the same operating conditions, the use of $R1234yf$ has a slight detriment in entrainment ratio (about 2 points) but maximum double-choke compression ratio augments by 3%. At the adapted conditions (same primary inlet temperature, superheat and pressure ratios relative to the critical point of each fluid), the entrainment ratio augments by 3.5% when using $R1234ze(E)$, although the maximum compression

ratio and the actual mass flow rates are severely diminished. These changes result, overall, in average COP and cooling capacity decreases of 10% and 20% (resp. 4.2% and 26.6%) when using $R1234yf$ (resp. $R1234ze(E)$).

— A comparison with the predictions of a thermodynamic model regarding the design of an air ejector showed that, as the working gas approaches the ideal gas behaviour, qualitative differences between the real and perfect gas models diminish. Furthermore, various assumptions usually made in thermodynamic models are validated, in particular that the shock start position in the CAS varies linearly with the entrainment ratio and that the ejector flow structure and global performance can be reduced to a few dimensionless parameters: the secondary inlet temperature and pressure, the primary nozzle throat diameter, the entrainment ratio and the compression ratio, even under real gas conditions.

In the second stage of this thesis, a thermodynamic model was developed following the flow characteristics observed for single-phase ejectors and applying mass, momentum and energy conservation principles through key regions of the ejector. Different from common thermodynamic models, the algorithm presented in this thesis takes an *operation* approach for real gas ejectors, *i.e.*: the performance is determined for a given set of geometrical and operating parameters. Hence, input data comprise operating conditions at both inlets and primary throat, constant area section and diffuser exit diameters, while output results include the thermodynamic properties across the device, entrainment and limiting compression ratios, ejector efficiency and exergy performance. The model development and key results regarding ejector performance changes are published in a peer reviewed journal under Croquer *et al.* [2017]. In comparison with single-phase experimental data, an average deviation of 18% (resp. 4.5%) in terms of double choke entrainment ratio (resp. limiting compression ratio) is observed, which is in the same range as for similar models with a design formulation [Ameur *et al.*, 2016; Huang *et al.*, 1999]. Under two-phase conditions, the model is able to capture the entrainment ratio changes with primary inlet superheat in $R134a$ ejectors and predicts the choked mass flow rate of flashing CO_2 in convergent-divergent nozzles with an accuracy of 10%.

In general, droplets injected normally to the flow at the first half of the CAS have a negative impact on the ejector performance. RANS results showed that the internal flow structure has not noticeable changes except for very high injection fractions (10% of the primary flow mass flow rate). At these conditions, a detachment of the boundary layer is captured, which leads to an earlier shock train start. Similarly, shock intensity reduces by 8% (in terms of the across-shock pressure jump). These observations verify the hypothesis that the injection of droplets in the CAS of the device would reduce shock intensity and the entropy associated to these shocks. Nonetheless, the ejector Elbel and exergy efficiencies reduce respectively by 11% and 15%, and the maximum double-choke compression ratio reduces by 10%. This detriment in the device performance is related to the additional losses generated through droplet mixing with the primary flow, the additional entropy injected with the droplets and the consistent reduction in outlet temperature with increasing droplet injection fraction.

Beyond the negative results obtained regarding the injection of droplets into the ejector, this thesis shows the feasibility of combining RANS and thermodynamic modelling perspectives in the analysis of complex flows. As well as the importance gained by numerical methods in recent years, becoming a very powerful tool for studying flow configurations which are impossible to characterize with experimental methods.

Future perspectives

Experimental validation of the influence of droplet injection on the ejector performance

Given the important simplifications on which numerical studies are based, it is always necessary to validate the quality of the results against experimental data. This is particularly critical in the context of supersonic ejectors, since it has been shown in Section 3.5.3 and in previous studies [Bartosiewicz *et al.*, 2006] that different turbulence models predict important discrepancies concerning the internal structure prediction despite having nearly the same global accuracy (entrainment and compression ratio).

With the objective of assessing the accuracy of the numerical models presented in this thesis, an experimental test bench comprising an 3 kW $R134a$ HDRC refrigeration loop is under construction at the facilities of CanmetENERGY (Varennes, Québec). The cycle heat input is a 10 kW electric boiler generating $R134a$ saturated steam in the temperature range 70 °C to 80 °C. Electrical elements will also be included to add 5 °C superheat. The condenser and evaporator are brazed plate heat exchangers with respective nominal capacities of 15 kW and 5 kW. The heat extracted from the condenser is transferred to a propylene-glycol/water (30%) loop. The system can achieve secondary inlet saturation temperatures of about 5 °C.

The test ejector has been designed for single-phase applications, is made of brass and has motive throat and constant area section diameters of 3.27 mm and 7 mm respectively.

Two holes have been drilled at the start and middle of the constant area section for placing an injector such that droplets enter normally to the main flow. $R134a$ droplets will be generated using a spin jet atomizer, fabricated by *Lee Company*, with an nominal orifice diameter of 0.2 mm, a nominal spray angle of 70 °C and a recommended differential pressure between 345 kPa and 1380 kPa. Figure 7.1 shows a preliminary blueprint of the ejector CAS with the location of the droplet injection sites.

Expected data collection comprises: primary and secondary inlets mass flow rates, pressure and temperature; wall pressure values at the start and end of the constant area section; and pressure and temperature at the generator, evaporator and condenser. This will allow to perform comparison with numerical results regarding the ejector global behaviour (ω_r vs. P_{ratio} curve for various operating conditions) and punctual pressure values at the extremes of the CAS. In addition, the test bench will allow to determine the effect of droplet injection on the performance of the complete cycle (in terms of COP and cooling capacity), an effect not considered in the numerical studies. The experimental bench is currently in a test phase to ensure its proper construction, with the first experimental runs planned for the first quarter of 2018.

Large Eddy Simulation of an air supersonic ejector

With a general RANS modelling strategy for supersonic ejectors already outlined, efforts now divert into two distinct roads: on the one hand to exploit RANS results for studying the energy and exergy transfer at specific configurations, such as the entropy accounting performed by Sierra-Pallares *et al.* [2016] and the *exergy tubes* concept introduced by Lamberts *et al.* [2017b]. On the other hand, to explore other numerical modelling approaches which, although of a higher computational cost, provide much greater detail and a more realistic representation of the flow. The next logical step in the latter direction is the Large Eddy Simulation (LES) of supersonic ejectors.

In the Large Eddy Simulation (LES) approach, the solution of a filtered version of the Navier-Stokes equations is sought. The filtering process, which usually takes the local grid size as threshold, divides the flow structures into two groups: those larger than the threshold (which are often case-dependent) are fully resolved, while those smaller are modelled assuming they have an universal character. Thus, a more realistic representation of the energy-carrying flow structures is produced, without the heavy simplifications intrinsic to the RANS averaging steps. The downside of this approach is the higher computational costs associated, both in terms of computing power and memory storage, as much finer meshes are required (typical element sizes lie in the range of the inertial scales) and it is necessary to collect instantaneous results over a long simulated time period. Complete theoretical descriptions of the LES technique for incompressible and compressible flows can be found respectively in Sagaut [2006] and Garnier *et al.* [2009].

Currently, a pioneering LES model of a supersonic air ejector is being developed, with the main objective of performing a detailed analysis of the turbulent structures and energy exchanges occurring as both inflows interact through the mixing and constant area sections. The baseline case corresponds to an experimental facility located at the *Université Catholique de Louvain* (Belgium), equipped with a supersonic ejector of rectangular section (width 0.05 m, length 1.52 m) and heights, respectively at the primary throat and constant area section, of 0.006 m and 0.027 m. The device has a nominal $Re = 6.6 \times 10^5$ and a $Ma = 1.61$, with inlet conditions of 5 bar and 300 K at the primary inlet, and 0.96 bar and 300 K at the secondary inlet. The reader is referred to Lamberts *et al.* [2017a] for a detailed description of the experimental facility.

The numerical model has been built assuming perfect gas behaviour and that the transversal character of the flow is negligible in comparison with the axial and vertical components. Thus, in order to reduce computational costs, the simulated domain is a slab section of 0.01 m wide with symmetry at both sides. Spatial discretization was carried out using an unstructured mesh with 240 million tetrahedral elements and 21 wall-adjacent prismatic layers. Given the extremely small element size required to completely solve the boundary layers, the assumption of a log-law wall function was preferred, which relaxes the $y+$ requirement to an average of 25 through the domain. Total pressure and total temperature were prescribed at both inlets, while static pressure was fixed at the outlet.

The numerical solution is obtained using the finite-element code *AVBP* [Schoenfeld and Rudgyard, 1999], which solves the filtered Navier-Stokes equations using a Two-Step Taylor Galerking scheme (TTG4A), of *4th* order in time and *3rd* order in space [Colin and Rudgyard, 2000]. Similar to the RANS approach, additional terms resembling an stress tensor appear in the filtered Navier-Stokes equations, although in this case they make the liaison between the resolved energy-carrying scales and the modelled subgrid (energy-dissipating) scales. These terms are assumed to be proportional to a numerical viscosity, which is computed using the *WALE* model of Nicoud and Ducros [1999], known for its better suitability for wall-bounded flows. Moreover, preventing the appearance of shock waves, an additional artificial viscosity is added to smooth the solution in regions of sharp gradients detected using a pressure-based sensor. Computations are currently running using the *Mammouth Parallèle 2* supercomputer located at *Université de Sherbrooke*. The allocation for this project consists of 100 AMD Opteron nodes, each with 12 cores and 32

GB RAM and a theoretical performance of 201.6 Gflops per node. With this configuration, simulating one ejector characteristic time ($t_c = 0.003\,\mathrm{s}$, the time required for a particle to traverse the computational domain) takes about 36 days.

The calculation was initialized using a RANS solution. Once the LES computation starts, the simulation must be run for some time to allow for the configuration to reach steady state. In this case stabilization was observed after about 5 characteristic times. After this point, the simulation is ran for a few more characteristic times while collecting the data of interest. In this case, the full domain is stored every 1×10^{-4} s, vertical mid-planes are stored with a frequency of $t_c/100$ and punctual flow properties at different locations through the domain are recollected with a frequency of $t_c/60000$.

Experimental validation will be carried out in terms of average wall pressure measurements and comparisons with Schlieren imagery. An example of the latter is shown in Figure 7.2. Despite being at a preliminary stage, the LES predicted motive jet structure is in good agreement with the experimental visualizations, in particular the number and location of the distinct cells in the motive jet is well captured.

A few examples of the information expected to be obtained from these calculations is given in Figures 7.3 and 7.4. The former presents an instantaneous take of the turbulent structures generated at the mixing layer coloured by their rotation sense, which provides insight on the exchange mechanisms occurring through the shear layer and reveal the higher precision achievable by this technique for energy and exergy accounting. Meanwhile, Figure 7.4 shows the pressure fluctuations at different punctual locations through the ejector domain. Based on time variations of different quantities such as pressure, velocity components and Reynolds stresses will allow for a better characterization of the flow and to eventually understand the relation between these complex features and the ejector performance.

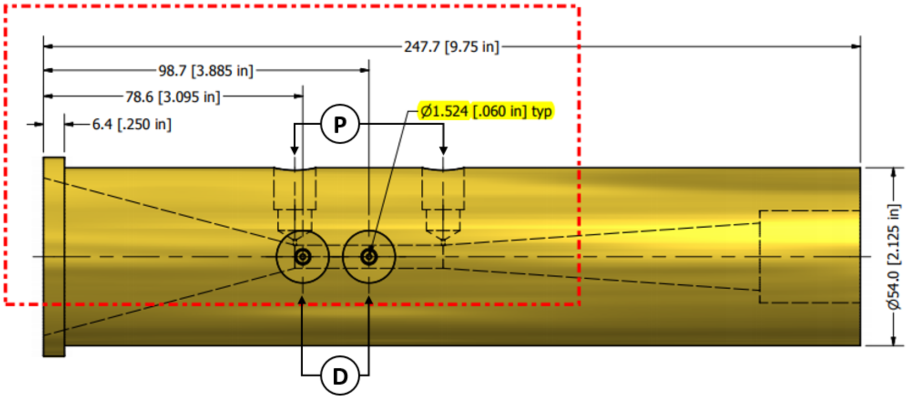

Figure 7.1 Preliminary blueprint of the ejector constant area section for the experimental tests, indicating the location of the droplet injection orifices (D) and the wall pressure transducers (P).

Plan préliminaire de la section constante de l'éjecteur pour les essais expérimentaux, indiquant l'emplacement des orifices d'injection des gouttelettes (D) et des transducteurs de pression aux parois (P).

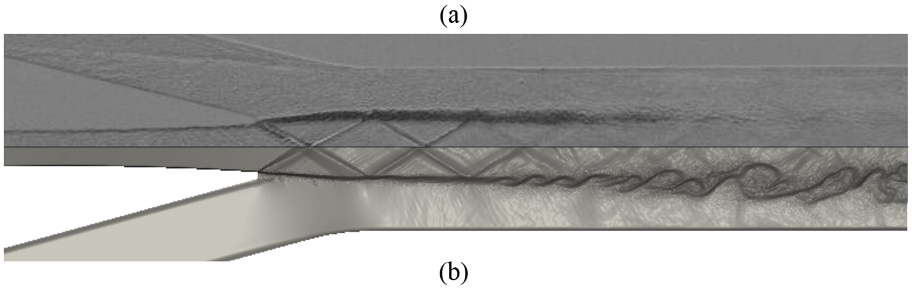

Figure 7.2 Comparison between (a) an ejector Schlieren image and (b) an instantaneous mean density gradient obtained using LES.

Comparaison entre (a) une image Schlieren de l'éjecteur et (b) un gradient de densité moyen instantané obtenu en utilisant la LES.

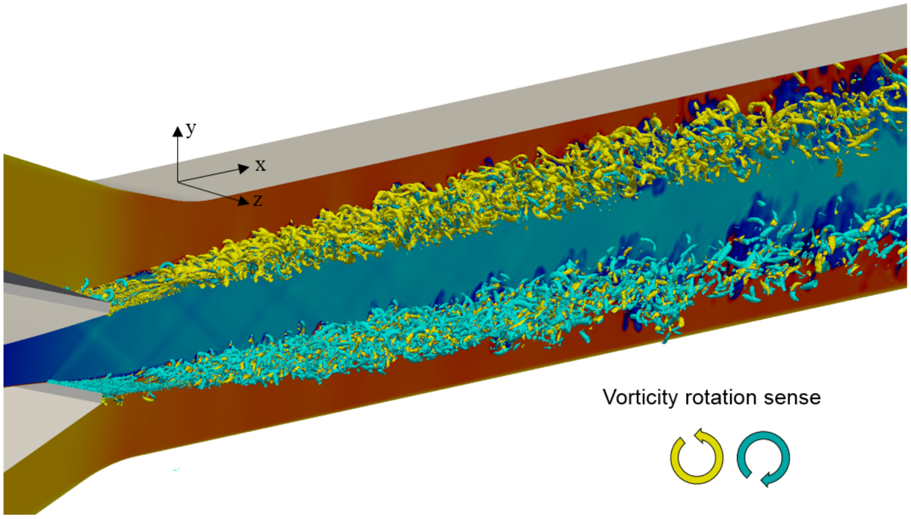

Figure 7.3 Iso-contours of the Q criterion coloured by the vorticity rotation sense.

Iso-contours du critère Q colorés par le sens de rotation des tourbillons.

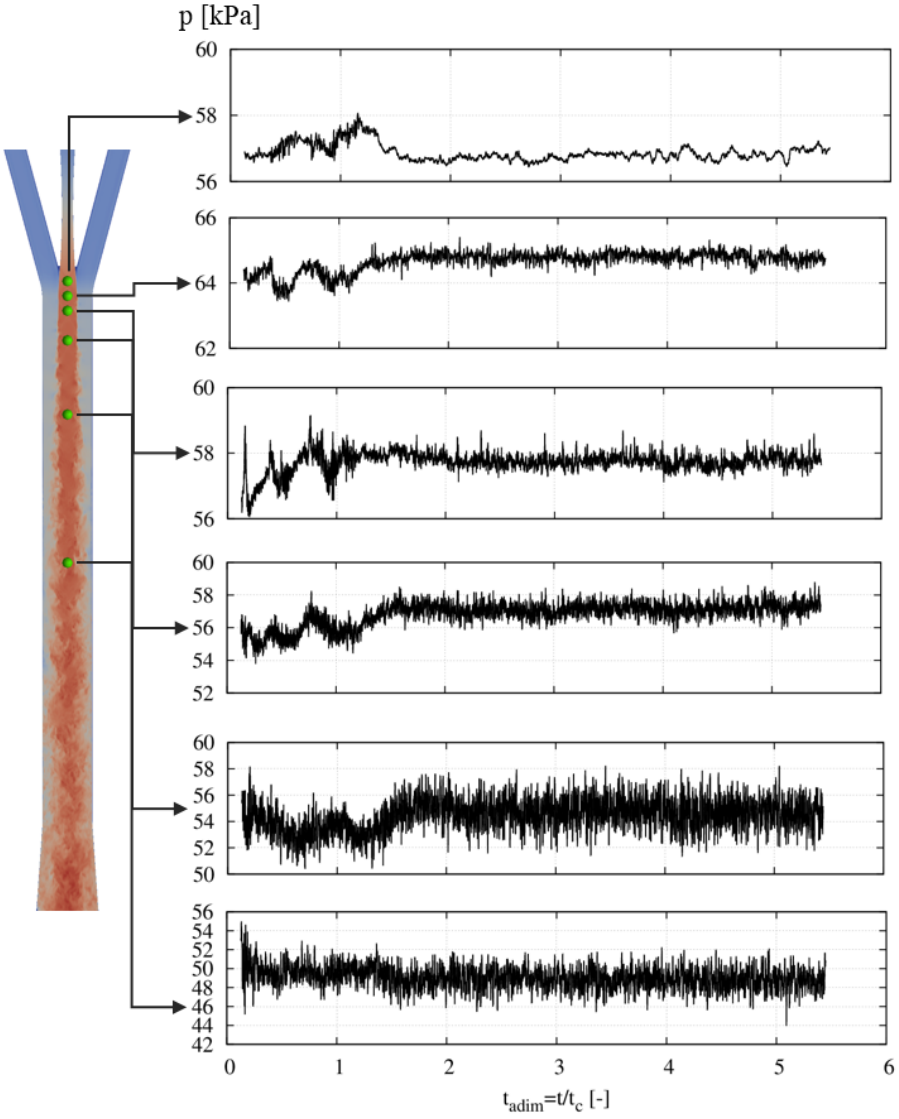

Figure 7.4 Pressure data collection at different punctual locations through the ejector domain.

Données de pression en fonction du temps prises à différents emplacements ponctuels à travers le domaine éjecteur.

The results shown in this thesis have been published in various international conferences and journals, namely:

Journals

- Croquer, S., Poncet, S. and Aidoun, Z. (2017). Thermodynamic Modelling of Supersonic Gas Ejector with Droplets. Entropy, 19(579), 1-21.

- Fang, Y., Croquer, S., Poncet, S., Aidoun, Z. and Bartosiewicz, Y. (2017). Drop-in replacement in a R134 ejector refrigeration cycle by HFO refrigerants. International Journal of Refrigeration, 77, 87-98.

- Croquer, S., Poncet, S. and Galanis, N. (2016). Comparison of ejector predicted performance by thermodynamic and CFD models. International Journal of Refrigeration, 68, 28-36.

- Croquer, S., Poncet, S. and Aidoun, Z. (2016). Turbulence modeling of a single-phase R134a supersonic ejector. Part 2: Local flow structure and exergy analysis. International Journal of Refrigeration, 61, 153-165.

- Croquer, S., Poncet, S. and Aidoun, Z. (2016). Turbulence modeling of a single-phase R134a supersonic ejector. Part 1: Numerical benchmark. International Journal of Refrigeration, 61, 140-152.

Conferences

- Croquer S., Fang Y., Poncet S., Aidoun Z., Bartosiewicz Y. Turbulence modeling of single-phase ejector working with HFO refrigerants. 26th Canadian Congress Of Applied Mechanics, May 29 - June 1, 2017, Victoria, Canada.

- *Paper & Oral Presentation*: Croquer S., Poncet S., Galanis N. Coupled thermodynamic and CFD approaches applied to a supersonic air ejector. 2016 Purdue Conferences: compressor engineering, refrigeration and air conditioning, high performance buildings, July 11-14, 2016, Purdue, USA.

- *Paper & Oral Presentation*: Croquer S., Poncet S., Aidoun Z. Operation and Exergetic Analysis of a Supersonic R134a Ejector by Low-Reynolds number Turbulence Model. 24th International Congress of Refrigeration, August 16-22, 2015, Yokohama, Japan.
- *Paper & Poster*: Croquer S., Poncet S., Aidoun Z., Etude numérique d'un éjecteur monophasique fonctionnant au R-134a, XII Colloque Franco-Québécois sur la Thermique des Systèmes, June 8-10, 2015, Sherbrooke, Canada.

LIST OF REFERENCES

Abe, Y. and Shibayama, S. (2014). Study on the characteristics of the supersonic steam injector. *Nuclear Engineering and Design*, volume 268, pp. 191–202.

Adiga, K., Willauer, H. D., Ananth, R. and Williams, F. W. (2009). Implications of droplet breakup and formation of ultra fine mist in blast mitigation. *Fire Safety Journal*, volume 44, number 3, pp. 363–369.

Al-Ansary, H. and Jeter, S. (2004). Numerical and Experimental Analysis of Single-Phase and Two-Phase Flow in Ejectors. *HVAC&R Research*, volume 10, number 4, pp. 521–538.

Ameur, K., Aidoun, Z. and Ouzzane, M. (2016). Modeling and numerical approach for the design and operation of two-phase ejectors. *Applied Thermal Engineering*, volume 109, pp. 809–818.

Ansari, N., Yadav, B. and Kumar, J. (2013). Theoretical exergy analysis of HFO-1234yf and HFO-1234ze as an Alternative Replacement of HFC-134a in Simple Vapour Compression Refrigeration System. *International Journal of Scientific & Engineering Research*, volume 4, number 8, pp. 137–144.

ANSYS (2013). *ANSYS FLUENT Theory Guide release 15.0, ANSYS Inc.*

ASHRAE (1983). *Handbook: Equipment, Chapter 13, Steam jet refrigeration equipment.*

Attou, A. and Seynhaeve, J. (1999). Steady-state critical two-phase flashing flow with possible multiple choking phenomenon. *Journal of Loss Prevention in the Process Industries*, volume 12, number 5, pp. 335–345.

Banasiak, K. and Hafner, A. (2011). 1D Computational model of a two-phase R744 ejector for expansion work recovery. *International Journal of Thermal Sciences*, volume 50, number 11, pp. 2235–2247.

Banasiak, K. and Hafner, A. (2013). Mathematical modelling of supersonic two-phase R744 flows through converging–diverging nozzles: The effects of phase transition models. *Applied Thermal Engineering*, volume 51, number 1-2, pp. 635–643.

Banasiak, K., Hafner, A. and Andresen, T. (2012). Experimental and numerical investigation of the influence of the two-phase ejector geometry on the performance of the R744 heat pump. *International Journal of Refrigeration*, volume 35, number 6, pp. 1617–1625.

Banasiak, K., Palacz, M., Hafner, A., Bulinski, Z., Smolka, J., Nowak, A. and Fic, A. (2014). A CFD-based investigation of the energy performance of two-phase R744 ejectors to recover the expansion work in refrigeration systems: An irreversibility analysis. *International Journal of Refrigeration*, volume 40, pp. 328–337.

Bartosiewicz, Y., Aidoun, Z., Desevaux, P. and Mercadier, Y. (2005). Numerical and experimental investigations on supersonic ejectors. *International Journal of Heat and Fluid Flow*, volume 26, number 1, pp. 56–70.

Bartosiewicz, Y., Aidoun, Z. and Mercadier, Y. (2006). Numerical assessment of ejector operation for refrigeration applications based on CFD. *Applied Thermal Engineering*, volume 26, number 5-6, pp. 604–612.

Bell, I. H., Wronski, J., Quoilin, S. and Lemort, V. (2014). Pure and pseudo-pure fluid thermophysical property evaluation and the open-source thermophysical property library coolprop. *Industrial & Engineering Chemistry Research*, volume 53, number 6, pp. 2498–2508.

Besagni, G., Mereu, R. and Inzoli, F. (2015). Cfd study of ejector flow behavior in a blast furnace gas galvanizing plant. *Journal of Thermal Science*, volume 24, number 1, pp. 58–66.

Besagni, G., Mereu, R. and Inzoli, F. (2016). Ejector refrigeration: a comprehensive review. *Renewable and Sustainable Energy Reviews*, volume 53, pp. 373–407.

Bilir Sag, N., Ersoy, H., Hepbasli, A. and Halkaci, H. (2015). Energetic and exergetic comparison of basic and ejector expander refrigeration systems operating under the same external conditions and cooling capacities. *Energy Conversion and Management*, volume 90, pp. 184–194.

Bouhanguel, A., Desevaux, P. and Gavignet, E. (2011). Flow visualization in supersonic ejectors using laser tomography techniques. *International Journal of Refrigeration*, volume 34, pp. 1633–1640.

Bouhanguel, A., Desevaux, P. and Gavignet, E. (2015). Visualization of flow instabilities in supersonic ejectors using large eddy simulation. *Journal of Visualization*, volume 18, number 1, pp. 17–19.

Cai, L. and He, M. (2013). A Numerical Study on the Supersonic Steam Ejector Used in Steam Turbine System. *Mathematical Problems in Engineering*, volume 2013, pp. 1–9.

Camporese, R., Bigolaro, G. and Rebellato, L. (1985). Calculation of thermodynamic properties of refrigerants by the Redlich-Kwong-Soave equation of state. *International Journal of Refrigeration*, volume 8, number 3, pp. 147–151.

Chauvin, A., Jourdan, G., Daniel, E., Houas, L. and Tosello, R. (2011). Experimental investigation of the propagation of a planar shock wave through a two-phase gas-liquid medium. *Physics of Fluids*, volume 23, number 11, pp. 1–14.

Chen, W., Liu, M., Chong, D. T., Yan, J., Little, A. and Bartosiewicz, Y. (2013). A 1D model to predict ejector performance at critical and sub-critical operational regimes. *International Journal of Refrigeration*, volume 36, number 6, pp. 1750–1761.

Chong, D., Hu, M., Chen, W., Wang, J., Liu, J. and Yan, J. (2014). Experimental and numerical analysis of supersonic air ejector. *Applied Energy*, volume 130, pp. 679–684.

Chong, D., Yan, J., Wu, G. and Liu, J. (2009). Structural optimization and experimental investigation of supersonic ejectors for boosting low pressure natural gas. *Applied Thermal Engineering*, volume 29, number 14-15, pp. 2799–2807.

Chunnanond, K. and Aphornratana, S. (2004). Ejectors: applications in refrigeration technology. *Renewable and Sustainable Energy Reviews*, volume 8, number 2, pp. 129–155.

Clift, R., Grace, J. R. and Weber, M. E. (2005). *Bubbles, drops, and particles.* Courier Corporation.

Colin, O. and Rudgyard, M. (2000). Development of high-order taylor–galerkin schemes for LES. *Journal of Computational Physics*, volume 162, number 2, pp. 338–371.

Cornman, J. K. and Bliss, D. B. (2012). *CFD Optimization of Small Gas Ejectors Used in Navy Diving Systems.* Ph.D. thesis, Duke University.

Croquer, S., Poncet, S. and Aidoun, Z. (2016a). Turbulence modeling of a single-phase R134a supersonic ejector. Part 1: Numerical benchmark. *International Journal of Refrigeration*, volume 61, pp. 140–152.

Croquer, S., Poncet, S. and Aidoun, Z. (2016b). Turbulence modeling of a single-phase R134a supersonic ejector. Part 2: Local flow structure and exergy analysis. *International Journal of Refrigeration*, volume 61, pp. 153–165.

Croquer, S., Poncet, S. and Aidoun, Z. (2017). Thermodynamic modelling of supersonic gas ejector with droplets. *Entropy*, volume 19, number 11, p. 579.

Croquer, S., Poncet, S. and Galanis, N. (2016c). Comparison of ejector predicted performance by thermodynamic and CFD models. *International Journal of Refrigeration*, volume 68, pp. 28–36.

de Castro, T. P., de Lima, R. C., Ribeiro, L. N., Zaparoli, E. L. and de Andrade, C. R. (2010). A CFD Analysis of a Gas Flow in a Supersonic Ejector. In *VI National Congress of Mechanical Engineering, Paraiba, Brasil, 18-21 August.*

Desevaux, P. and Lanzetta, F. (2004). Computational Fluid Dynamic Modeling of a Pseudoshock Inside a Zero-Secondary Flow Ejector. *AIAA Journal*, volume 42, number 7, pp. 7–10.

Disawas, S. and Wongwises, S. (2004). Experimental investigation on the performance of the refrigeration cycle using a two-phase ejector as an expansion device. *International Journal of Refrigeration*, volume 27, number 6, pp. 587–594.

Eames, I., Aphornratana, S. and Haider, H. (1995). A theoretical and experimental study of a small-scale steam jet refrigerator. *International Journal of Refrigeration*, volume 18, number 6, pp. 378–386.

Elbel, S. and Hrnjak, P. (2008). Experimental validation of a prototype ejector designed to reduce throttling losses encountered in transcritical R744 system operation. *International Journal of Refrigeration*, volume 31, pp. 411–422.

Ersoy, H. K. and Bilir Sag, N. (2014). Preliminary experimental results on the R134a refrigeration system using a two-phase ejector as an expander. *International Journal of Refrigeration*, volume 43, pp. 97–110.

ERTC (2016). *About Ejector Refrigeration Technologies.* Retrieved from: `http:\\www.ertc.od.ua\en\about_ert_en.html` on September 12th 2016.

Fabri, J. and Siestrunck, R. (1958). Supersonic air ejectors. *Advanced Applied Mechanics*, volume 6, pp. 1–34.

Fang, Y., Croquer, S., Poncet, S., Aidoun, Z. and Bartosiewicz, Y. (2017). Drop-in replacement in a R134 ejector refrigeration cycle by HFO refrigerants. *International Journal of Refrigeration*, volume 77, pp. 87–98.

Ferziger, J. and Peric, M. (2002). *Computational Methods for Fluid Dynamics*, 3rd edition. Springer-Verlag, Germany.

Galanis, N. and Sorin, M. (2016). Ejector design and performance prediction. *International Journal of Thermal Sciences*, volume 104, pp. 315–329.

Galanis, N., Sorin, M. and Samaké, O. (2014). Thermodynamic study of multi-effect thermal vapour-compression desalination systems. *Energy 2014*, pp. 1–11.

García del Valle, J., Sáiz Jabardo, J., Castro Ruiz, F. and San José Alonso, J. (2012). A one-dimensional model for the determination of an ejector entrainment ratio. *International Journal of Refrigeration*, volume 35, number 4, pp. 772–784.

García del Valle, J., Saíz Jabardo, J., Castro Ruiz, F. and San José Alonso, J. (2014). An experimental investigation of a R134a ejector refrigeration system. *International Journal of Refrigeration*, volume 46, pp. 105–113.

García del Valle, J., Saíz Jabardo, J., Castro Ruiz, F. and San José Alonso, J. (2015). An experimental and computational study of the flow pattern in a refrigerant ejector. Validation of turbulence models and real-gas effects. *International Journal of Refrigeration*, volume 89, pp. 795–811.

Garnier, E., Adams, N. and Sagaut, P. (2009). *Large eddy simulation for compressible flows*. Springer Science & Business Media.

Hakkaki-fard, A., Poirier, M., Aidoun, Z., Ouzzane, M. and Guiguere, D. (2015). An experimental study of an ejector supported by CFD. In *24th International Congress of Refrigeration, Yokohama*. pp. 1–8.

He, S., Li, Y. and Wang, R. (2009). Progress of mathematical modeling on ejectors. *Renewable and Sustainable Energy Reviews*, volume 13, number 8, pp. 1760–1780.

Hemidi, A., Henry, F., Leclaire, S., Seynhaeve, J.-M. and Bartosiewicz, Y. (2009a). CFD analysis of a supersonic air ejector. Part I: Experimental validation of single-phase and two-phase operation. *Applied Thermal Engineering*, volume 29, number 8-9, pp. 1523–1531.

Hemidi, A., Henry, F., Leclaire, S., Seynhaeve, J.-M. and Bartosiewicz, Y. (2009b). CFD analysis of a supersonic air ejector. Part II: Relation between global operation and local flow features. *Applied Thermal Engineering*, volume 29, number 8-9, pp. 2990–2998.

Henzler, H. (1983). Design of ejectors for single-phase material systems. *German Chemical Engineering*, volume 6, pp. 292–300.

Huang, B., Chang, J., Wang, C. and Petrenko, V. (1999). A 1-D analysis of ejector performance. *International Journal of Refrigeration*, volume 22, pp. 354–364.

Huang, B.-J., Jiang, C. and Hu, F. (1985). Ejector performance characteristics and design analysis of jet refrigeration system. *Journal of engineering for gas turbines and power*, volume 107, number 3, pp. 792–802.

Igra, O., Falcovitz, J., Houas, L. and Jourdan, G. (2013). Review of methods to attenuate shock/blast waves. *Progress in Aerospace Sciences*, volume 58, pp. 1–35.

Jarall, S. (2012). Study of refrigeration system with HFO-1234yf as a working fluid. *International Journal of Refrigeration*, volume 35, pp. 1668–1677.

Jourdan, G., Biamino, L., Mariani, C., Blanchot, C., Daniel, E., Massoni, J., Houas, L., Tosello, R. and Praguine, D. (2010). Attenuation of a shock wave passing through a cloud of water droplets. *Shock Waves*, volume 20, number 4, pp. 285–296.

Karthick, S., Gopalan, J. and Reddy, K. (2016). Visualization of supersonic free and confined jet using planar laser mie scattering technique. *Journal of the Indian Institute of Science*, volume 96, number 1, pp. 29–46.

Keenan, J. H. (1950). An investigation of ejector design by analysis and experiment. *Journal of Applied Mechanics*, volume 17, p. 299.

Khennich, M., Sorin, M. and Galanis, N. (2014). Equivalent Temperature-Enthalpy Diagram for the Study of Ejector Refrigeration Systems. *Entropy*, volume 16, number 5, pp. 2669–2685.

Lamberts, O., Chatelain, P. and Bartosiewicz, Y. (2017a). Experimental and numerical analysis of the flow within a supersonic ejector. In *Proceedings of the International Symposium on Advances in Computational Heat Transfer*.

Lamberts, O., Chatelain, P. and Bartosiewicz, Y. (2017b). New methods for analyzing transport phenomena in supersonic ejectors. *International Journal of Heat and Fluid Flow*, volume 64, pp. 23–40.

Lawrence, N. and Elbel, S. (2013). Theoretical and practical comparison of two-phase ejector refrigeration cycles including First and Second Law analysis. *International Journal of Refrigeration*, volume 36, number 4, pp. 1220–1232.

Lawrence, N. and Elbel, S. (2014). Experimental investigation of a two-phase ejector cycle suitable for use with low-pressure refrigerants R134a and R1234yf. *International Journal of Refrigeration*, volume 38, pp. 310–322.

Lawrence, N. and Elbel, S. (2015). Analysis of two-phase ejector performance metrics and comparison of R134a and CO_2 ejector performance. *Science and Technology for the Built Environment*, volume 21, number 5, pp. 515–525.

Lemmon, E. W., Jacobsen, R. T., Penoncello, S. G. and Friend, D. G. (2000). Thermodynamic properties of air and mixtures of nitrogen, argon, and oxygen from 60 to 2000 k at pressures to 2000 mpa. *Journal of physical and chemical reference data*, volume 29, number 3, pp. 331–385.

Li, C. and Li, Y. (2011). Investigation of entrainment behavior and characteristics of gas-liquid ejectors based on CFD simulation. *Chemical Engineering Science*, volume 66, pp. 405–416.

Little, A. and Garimella, S. (2016). Shadowgraph visualization of condensing R134a flow through ejectors. *International Journal of Refrigeration*, volume 68, pp. 118–129.

Liu, F. and Groll, E. A. (2013). Study of ejector efficiencies in refrigeration cycles. *Applied Thermal Engineering*, volume 52, number 2, pp. 360–370.

Lucas, C., Rusche, H., Schroeder, A. and Koehler, J. (2014). Numerical investigation of a two-phase CO2 ejector. *International Journal of Refrigeration*, volume 43, pp. 154–166.

Marinovski, T., Desevaux, P. and Mercadier, Y. (2009). Experimental and numerical visualizations of condensation process in a supersonic ejector. *Journal of Visualization*, volume 12, number 3, pp. 251–258.

Maytal, B.-Z. (2006). Real gas choked flow conditions at low reduced-temperatures. *Cryogenics*, volume 46, number 1, pp. 21–29.

Maytal, B.-Z. and Elias, E. (2009). Two-phase choking conditions of real gases flow at their critical stagnation temperatures and closely above. *Cryogenics*, volume 49, number 9, pp. 469–481.

Mazzelli, F. and Milazzo, A. (2015). Performance analysis of a supersonic ejector cycle working with R245fa. *International Journal of Refrigeration*, volume 49, pp. 79–92.

Menegay, P. and Kornhauser, A. (1996). Improvements to the ejector expansion refrigeration cycle. *IECEC 96. Proceedings of the 31st Intersociety Energy Conversion Engineering Conference, Washington, USA, 11-16, August*, volume 2, pp. 702–706.

Menter, F. R. (1994). Two-equation eddy-viscosity turbulence models for engineering applications. *AIAA Journal*, volume 32, number 8, pp. 1598–1605.

Morsi, S. and Alexander, A. (1972). An investigation of particle trajectories in two-phase flow systems. *Journal of Fluid Mechanics*, volume 55, number 2, pp. 193–208.

Mota-Babiloni, A., Navarro-Esbri, J., Molès, F., Barragán Cervera, A., Peris, B. and Verdú, G. (2016). A review of refrigerant R1234ze(E) recent investigations. *Applied Thermal Engineering*, volume 95, pp. 211–222.

Munday, J. and Bagster, D. (1977). A new ejector theory applied to steam jet refrigeration. *Industrial & Engineering Chemistry Process Dessign and Development*, volume 16, number 4, pp. 442–449.

Nicoud, F. and Ducros, F. (1999). Subgrid-scale stress modelling based on the square of the velocity gradient tensor. *Flow, Turbulence and Combustion*, volume 62, pp. 183–200.

NIST (2010). *NIST Reference Fluid Thermodynamic and Transport Properties - REFPROP, v9.0.*

Ozgur, A., Kabul, A. and Kizilkan, O. (2012). Exergy analysis of refrigeration systems using an alternative refrigerant (HFO-1234yf) to R-134a. *International Journal of Low-Carbon Technologies*, volume 0, pp. 1–7.

Parliament, E. and Council (2014). Regulation (EU) No 517/2014 of the European Parliament and the Council of 16 April 2014 on fluorinated greenhouse gases and repealing Regulation (EC) No 842/2006. *Official Journal of the European Union*, volume 150, pp. 195–230.

Pianthong, K., Seehanam, W., Behnia, M., Sriveerakul, T. and Aphornratana, S. (2007). Investigation and improvement of ejector refrigeration system using computational fluid dynamics technique. *Energy Conversion and Management*, volume 48, number 9, pp. 2556–2564.

Pilch, M. and Erdman, C. (1987). Use of breakup time data and velocity history data to predict the maximum size of stable fragments for acceleration-induced breakup of a liquid drop. *International Journal of Multiphase Flow*, volume 13, number 6, pp. 741–757.

Pope, S. (2009). *Turbulent Flows*, 1st edition. Cambridge University Press, India.

Ranz, W., Marshall, W. *et al.* (1952). Evaporation from drops. *Chem. Eng. Prog*, volume 48, number 3, pp. 141–146.

Rao, S. M. and Jagadeesh, G. (2014). Novel supersonic nozzles for mixing enhancement in supersonic ejectors. *Applied Thermal Engineering*, volume 71, number 1, pp. 62–71.

Reddick, C., Mercadier, Y. and Ouzzane, M. (2012). Experimental study of an ejector refrigeration system. In *International Refrigeration and Air Conditioning Conference, Purdue University, USA*. pp. 1–10.

Reddick, C., Sorin, M. and Rheault, F. (2014). Energy savings in CO2 (carbon dioxide) capture using ejectors for waste heat upgrading. *Energy*, volume 65, pp. 200–208.

Reitz, R. *et al.* (1987). Modeling atomization processes in high-pressure vaporizing sprays. *Atomisation and Spray Technology*, volume 3, number 4, pp. 309–337.

Ruangtrakoon, N., Thongtip, T., Aphornratana, S. and Sriveerakul, T. (2013). CFD simulation on the effect of primary nozzle geometries for a steam ejector in refrigeration cycle. *International Journal of Thermal Sciences*, volume 63, pp. 133–145.

Sagaut, P. (2006). *Large eddy simulation for incompressible flows: an introduction.* Springer Science & Business Media.

Samaké, O., Galanis, N. and Sorin, M. (2014). Thermodynamic study of multi-effect thermal vapour-compression desalination systems. *Energy*, volume 72, pp. 69–79.

Schoenfeld, T. and Rudgyard, M. (1999). Steady and unsteady flow simulations using the hybrid flow solver avbp. *AIAA journal*, volume 37, number 11, pp. 1378–1385.

Scott, D., Aidoun, Z., Bellache, O. and Ouzzane, M. (2008). CFD simulations of a supersonic ejector for use in refrigeration applications. In *International Refrigeration and Air Conditioning Conference, Purdue University, USA*. pp. 2159–1–2159–8.

Scott, D., Aidoun, Z. and Ouzzane, M. (2011). An experimental investigation of an ejector for validating numerical simulations. *International Journal of Refrigeration*, volume 34, pp. 1717–1723.

Selvaraju, A. and Mani, A. (2006). Experimental investigation on R134a vapour ejector refrigeration system. *International Journal of Refrigeration*, volume 29, number 7, pp. 1160–1166.

Sharifi, N., Boroomand, M. and Sharifi, M. (2013). Numerical assessment of steam nucleation on thermodynamic performance of steam ejectors. *Applied Thermal Engineering*, volume 52, number 2, pp. 449–459.

Shih, T.-H., Liou, W. W., Shabbir, A., Yang, Z. and Zhu, J. (1995). A new k-ϵ eddy viscosity model for high reynolds number turbulent flows. *Computers & Fluids*, volume 24, number 3, pp. 227–238.

Sierra-Pallares, J., del Valle, J. G., Carrascal, P. G. and Ruiz, F. C. (2016). A computational study about the types of entropy generation in three different r134a ejector mixing chambers. *International Journal of Refrigeration*, volume 63, pp. 199–213.

Smith, J., Van Ness, H. and Abbott, M. (1996). McGraw-Hill, New-York.

Smolka, J., Bulinski, Z., Fic, A., Nowak, A. J., Banasiak, K. and Hafner, A. (2013). A computational model of a transcritical R744 ejector based on a homogeneous real fluid approach. *Applied Mathematical Modelling*, volume 37, number 3, pp. 1208–1224.

Sriveerakul, T., Aphornratana, S. and Chunnanond, K. (2007). Performance prediction of steam ejector using computational fluid dynamics: Part 1. Validation of the CFD results. *International Journal of Thermal Sciences*, volume 46, number 8, pp. 812–822.

Stoecker, W. (1958). *Refrigeration and Air Conditioning.* Mac Graw Hill series in mechanical engineering, McGraw-Hill Companies.

Sumeru, K., Nasution, H. and Ani, F. (2012). A review on two-phase ejector as an expansion device in vapor compression refrigeration cycle. *Renewable and Sustainable Energy Reviews*, volume 16, number 7, pp. 4927–4937.

Sun, D.-W. (1996). Variable geometry ejectors and their applications in ejector refrigeration systems. *Energy*, volume 21, number 10, pp. 919–929.

Teymourtash, A. R., Esfahani, J. A. and Mousavi Shaegh, S. A. (2009). The effects of rate of expansion and injection of water droplets on the entropy generation of nucleating steam flow in a Laval nozzle. *Heat and Mass Transfer*, volume 45, pp. 1185–1198.

Thongtip, T., Ruangtrakoon, N. and Aphornratana, S. (2014). Development of a Steam Jet Refrigeration Cycle for the Actual Application Driven by Low Grade Thermal Energy. *Energy Procedia*, volume 52, pp. 110–119.

Tillner-Roth, R. and Baehr, H. (1994). An International Standard Formulation for the Thermodynamic Properties of 1,1,1,2-tetrafluoroethane (HFC-134a) for Temperatures From 170K to 455K and Pressures up to 70MPa. *Journal of Physical and Chemical Reference Data*, volume 23, number 5, pp. 657–729.

Untea, G., Dobrovicescu, A., Grosu, L. and Mladin, E. (2013). Energy and exergy analysis of an ejector refrigeration system. *University Politehnica of Bucarest, Scientific Bulletin, Series D*, volume 75, number 4, pp. 111–126.

Versteeg, H. K. and Malalasekera, W. (2007). *An introduction to computational fluid dynamics: the finite volume method*. Pearson Education.

Wang, C. (2014). System performance of R-1234yf refrigerant in air-conditioning and heat pump system - an overview of current status. *Applied Thermal Engineering*, volume 73, pp. 1412–1420.

Wang, X., Dong, J., Li, A., Lei, H. and Tu, J. (2014). Numerical study of primary steam superheating effects on steam ejector flow and its pumping performance. *Energy*, volume 78, pp. 205–211.

Wilcox, D. C. *et al.* (1998). *Turbulence modeling for CFD, volume 2*. DCW industries La Canada, CA.

Yakhot, V. and Orszag, S. A. (1986). Renormalization group analysis of turbulence. I. basic theory. *Journal of Scientific Computing*, volume 1, number 1, pp. 3–51.

Yang, Y., Shen, S., Kong, T. and Zhang, K. (2010). Numerical Investigation of Homogeneous Nucleation and Shock Effect in High-Speed Transonic Steam Flow. *Heat Transfer Engineering*, volume 31, number 12, pp. 1007–1014.

Yazdani, M., Alahyari, A. and Radcliff, T. (2012). Numerical modeling of two-phase supersonic ejectors for work-recovery applications. *International Journal of Heat and Mass Transfer*, volume 55, pp. 5744–5753.

Zhu, Y. and Jiang, P. (2014a). Experimental and analytical studies on the shock wave length in convergent and convergent–divergent nozzle ejectors. *Energy Conversion and Management*, volume 88, pp. 907–914.

Zhu, Y. and Jiang, P. (2014b). Experimental and numerical investigation of the effect of shock wave characteristics on the ejector performance. *International Journal of Refrigeration*, volume 40, pp. 31–42.

Zhu, Y., Wang, Z., Yang, Y. and Jiang, P. (2017). Flow visualization of supersonic two-phase transcritical flow of co_2 in an ejector of a refrigeration system. *International Journal of Refrigeration*, volume 74, pp. 352–359.